ISTANBUL TECHNICAL UNIVERSITY ★ GRADUATE SCHOOL OF SCIENCE
ENGINEERING AND TECHNOLOGY

INVESTIGATION OF DEEP BAR EFFECT ARISEN BY SPACE HARMONICS
AT THE START-UP STAGE OF SQUIRREL-CAGE INDUCTION MOTOR
FOR DIFFERENT BAR CROSS-SECTIONS

M.Sc. THESIS

Ahmet Yasin YEKSAN

Department of Electrical Engineering

Electrical Engineering Programme

MAY 2014

ISTANBUL TECHNICAL UNIVERSITY ★ GRADUATE SCHOOL OF SCIENCE
ENGINEERING AND TECHNOLOGY

INVESTIGATION OF DEEP BAR EFFECT ARISEN BY SPACE HARMONICS
AT THE START-UP STAGE OF SQUIRREL-CAGE INDUCTION MOTOR
FOR DIFFERENT BAR CROSS-SECTIONS

M.Sc. THESIS

Ahmet Yasin YEKSAN
(504111001)

Department of Electrical Engineering

Electrical Engineering Programme

Thesis Advisor: Prof. Dr. Ahmet Faik MERGEN

MAY 2014

SİNCAP KAFESLİ ASENKRON MOTORDA YOL VERME AŞAMASINDA UZAY HARMONİKLERİNİN OLUŞTURDUĞU DERİN OLUK ETKİSİNİN DEĞİŞİK OLUK PROFİLLERİNDE İNCELENMESİ

YÜKSEK LİSANS TEZİ

Ahmet Yasin YEKSAN
(504111001)

Elektrik Mühendisliği Anabilim Dalı

Elektrik Mühendisliği Programı

Tez Danışmanı: Prof. Dr. Ahmet Faik MERGEN

MAYIS 2014

Ahmet Yasin YEKSAN, a M.Sc. student of ITU Graduate School of Science Engineering and Technology 504111001 successfully defended the thesis entitled **"INVESTIGATION OF DEEP BAR EFFECT ARISEN BY SPACE HARMONICS AT THE START-UP STAGE OF SQUIRREL-CAGE INDUCTION MOTOR FOR DIFFERENT BAR CROSS-SECTIONS"**, which he prepared after fulfilling the requirements specified in the associated legislations, before the jury whose signatures are below.

Thesis Advisor :   **Prof. Dr. Ahmet Faik MERGEN**   ....
Istanbul Technical University

Jury Members :   **Prof. Dr. Ahmet Faik MERGEN**   ....
Istanbul Technical University

                    Assist. Prof. Dr. Derya Ahmet KOCABAŞ   ....
Istanbul Technical University

                    Prof. Dr. İbrahim ŞENOL   ....
Yıldız Technical University

Date of Submission :   **5 May 2014**
Date of Defense :   **27 May 2014**

To my family,

FOREWORD

I would like to express my gratitude to my thesis supervisor Prof. Dr. Ahmet Faik MERGEN for his invaluable guidance, support and encouragement throughout my thesis. I would like to also thank Assoc. Prof. Dr. Özgür ÜSTÜN and Asst. Prof. Dr. Derya Ahmet KOCABAŞ for sharing their knowledge and experience with me during my study. I would like to thank Dr. Murat İMERYÜZ for contacting Arçelik Motor Company and having required permission to use motor parameters for me.

I would like to mention Res. Asst. Mehmet Onur GÜLBAHÇE and thank him for his contributions. I would like to express my special thanks to my roommate Res. Asst. Furkan BAŞKURT and my dear friends Res. Asst. Ahmet Kubilay ATALAY, Res. Asst. Abdullah POLAT, Res. Asst. Aytuğ FONT, Res. Asst. Alparslan ZEHİR and all my colleagues in İTÜ Electrical Engineering Department for their support and strong friendship.

I would like to also thank my brothers Ömer Faruk GEMİCİ and Bilal ÖZASLAN for their contributions on this thesis and for their patience throughout my study.

My deepest gratitude goes to my family for their love and support throughout my life; this thesis was simply impossible without them.

May 2014   Ahmet Yasin YEKSAN
                                                                          Electrical Engineer

x

TABLE OF CONTENTS

ABBREVIATIONS

AC	:	Alternating Current
DC	:	Direct Current
FEA	:	Finite Element Analysis
FEM	:	Finite Element Method
IEEE	:	Institute of Electrical and Electronics Engineers
MMF	:	Magneto-motive Force

LIST OF TABLES

LIST OF FIGURES

INVESTIGATION OF DEEP BAR EFFECT ARISEN BY SPACE HARMONICS AT THE START-UP STAGE OF SQUIRREL-CAGE INDUCTION MOTOR FOR DIFFERENT BAR CROSS-SECTIONS

SUMMARY

Alternating current machines are widely used in many industrial and small power applications. Induction motors are the most preferred type in alternating current machines. This is because their construction is simple, manufacturing and maintenance costs are less and their control has become easier by power electronic converters. Hence, there have never been a decrement in their popularity in applications.

Deep bar effect is a phenomenon in squirrel-cage induction motors and many researches have been done about this subject. Deep bar effect can be simply defined as current displacement in rotor bars due to alternating magnetic field in the machine. The problem itself relies on skin effect actually. Because of the external magnetic field in the rotor bars, more eddy currents induced in the conductor and these currents pushes the bar current towards the top of the conductor. Since induced currents depends on the current frequency, this effect shows its maximum influence on the machine at the start-up. Deep bar effect can be seen as an disadvantage at first glance. However, this effect is used in some motor applications as an advantage. Because, induction motors that have deep rotor bars can start at high torque values. On the other hand, power losses in the motor can increase due to undesired effects of harmonics in the machine.If the efficiency is a severe problem in the machine, deep bar effect should be minimized.

As it is mentioned before, deep bar effect is caused by external alternating magnetic field. This field is arisen in the motor by leakage inductance of rotor bars. Leakage flux is induced by rotor currents and rotor bar current is induced by stator magnetic field. Even if the supply voltage and current is in sinusoidal form, due to construction of the machine winding distribution is not in sinusoidal waveform. As a result MMF function in the machine is not in sinusoidal waveform and MMF function in the motor affects all other induced magnitudes in the machine. Thus, space harmonics occur in the machine due to winding distribution in the stator. Space harmonics can not be avoided and their effect can not be ignored in the motor.

This study concentrates on the deep bar effect arisen by space harmonic components in a three-phase squirrel-cage induction motor. Another objective of the thesis is to investigate the effect of different bar geometries on deep bar effect and space harmonics. In the literature there are tremendous number of studies about deep bar effect and skin effect. However, studies that cover deep bar effect and space harmonics are very less. This study tries to compensate mentioned deficiency in the literature.

In this thesis, a three-phase squirrel-cage induction motor, which was manufactured by Arcelik Motor Company was used. A MATLAB code was generated to compute the winding function and MMF function of the motor by using motor parameters and

winding lay-out of the motor. Space harmonic components of the MMF function were obtained by using the same MATLAB code. As a next step, rotor model was drawn through AutoCAD 2014 software and a magnetic simulation model was created. Computed values were used in this model. Finite element method was the best and fastest method to solve the created model. Because of this reason, Ansoft Maxwell 14 was used to simulate the magnetic model. This simulation software uses the finite element method to solve the given problem and allows to assign mesh operation according to skin depth and takes skin effect in account. The effects of space harmonic and different cross-section rotor bars on deep bar effect were observed by using this software.

Four different rotor bar cross-sections that are round, square, deep bar and a novel two-way rotor bar were investigated. The effect of conductor material was also investigated by using copper and aluminum as rotor bar conductor.Procured results are very constructive and according to study results a novel squirrel-cage induction motor can be designed.

SİNCAP KAFESLİ ASENKRON MOTORDA YOL VERME AŞAMASINDA UZAY HARMONİKLERİNİN OLUŞTURDUĞU DERİN OLUK ETKİSİNİN DEĞİŞİK OLUK PROFİLLERİNDE İNCELENMESİ

ÖZET

Alternatif akım makinaları günümüzde elektrik enerjisi üretiminden sanayi uygulamalarına, elektrikli araçlardan ev aletlerine kadar birçok alanda yaygın olarak kullanılmaktadır. Bu makinalardan sincap kafesli asenkron motor, uygulamada en yaygın olarak kullanılan motor çeşitidir. Kullanımının bu kadar yaygın olmasının sebebleri yapısının basit ve ucuza mal olması, bakım masraflarının düşük ve uzun ömürlü olması ve güç elektroniği teknolojisinin gelişmesiyle hız ve moment kontrolünün de kolaylaşması olarak sayılabilir. Yeni nesil motorların üretilmiş olmasına rağmen asenkron motorlar uygulamadaki tercih edilirliğini hiç bir zaman kaybetmemiştir.

Asenkron motorların bu denli uzun zamandır ve yaygın bir şekilde kullanılması bir çok problemin ortaya çıkmasına ve araştırmacıların da yoğun bir şekilde asenkron motor uygulamaları üstüne çalışmasına sebep olmuştur. Sincap kafesli asenkron motorlarda en çok incelenen konulardan birisi de derin oluk etkisidir. 1950 yıllarının başında bu etki asenkron motorlarda incelenmeye başlanmış olup günümüze kadar sayısız çalışma ortaya konulmuştur.

Derin oluk etkisini en basit manada, alternatif bir manyetik alan etkisi altında kalan rotor çubuklarında akan alternatif akımın, endüklenen eddy akımlarının etkisi ile rotor çubuğu yüzeyine yığılması olarak tanımlayabiliriz. Tanımından da anlaşılacağı üzere aslında derin oluk etkisi, deri etkisinin bir türevidir. Aralarındaki fark ise derin oluk etkisinde, iletkene harici bir alternatif manyetik alanın nüfuz etmesidir.

Derin oluk etkisi ilk bakışta olumsuz olarak görünse de bu etkiden yararlanarak kalkış momenti yüksek motorlar tasarlanmıştır. Bashsedilen etki, yukarıda da belirtildiği üzere deri etkisi temelli bir olay olduğu için frekansa bağlıdır. Bilindiği üzere bir asenkron motorun kalkış anında kayma değeri 1'e eşit olacaktır ve bu anda rotor çubuklarında akan akımlar da stator besleme gerilimi frekansına eşit olacaktır. Bu durumda derin oluk etkisi en çok kalkış anında hissedilecek ve kalkış direncini artırarak kalkış momentinin de artmasını sağlayacaktır. Ancak şu da belirtilmelidir ki motorda oluşacak olan istenmeyen harmonik etkileri sebebiyle, derin oluk etkisi motor kayıplarının da artmasına sebep olabilir. Kalkış momentinden ziyade verimin önemli olduğu motor tasarımlarında bu etkinin mümkün olduğunca en az indirgenmesi istenecektir.

Bir asenkron motor saf sinüsoidal ve dengeli bir gerilim kaynağından beslense dahi, makinenin iç yapısından dolayı stator sargı dağılımı ve dolayısı ile stator amper-sarım dağılımı sinüsoidal formda olmaz. Bu yapısal özellik nedeni ile uzay harmonikleri açığa çıkacaktır. Bu durumda hava aralığı amper-sarım dağılımı ve rotora ulaşan magnetik alan yoğunluğu da statorda üretilen dalga formu ile aynı dalga formuna sahip olacaktır. Sonuç olarak ise rotor çubuklarında harmonik bileşenleri içeren akımlar

akacaktır. Rotor çubuklarının kaçak endüktansı ve akımları bir kaçak akı tanımlayacak ve bu kaçak akı derin oluk etkisinin tanımında bahsedilen harici manyetik alanı oluşturacaktır. Sonuç olarak statorda üretilen amper-sarım fonksiyonu makine içinde endüklenme sonucu ortaya çıkacak olan tüm değerleri etkileyecektir.

Bu noktada zaman harmoniklerinin etkisine değinmekte fayda vardır. Asenkron motorun saf sinüs formunda bir gerilimle beslenmemesi durumunda zaman harmonikleri ortaya çıkacaktır. Zaman harmoninklerinin makine üzerinde uzay harmoniklerine benzeyen etkileri olduğu söylenebilir. Kaynak geriliminin harmonik analizi yapıldığında ortaya çıkan her bir bileşenin stator ve rotor için etkileri olacaktır. Her bir zaman harmoniği bileşeni kendisi için bir eş değer devre tanımlayacaktır. Uzay harmonikleri ile zaman harmonikleri arasındaki temel farklılık aslında buradan gelmektedir. Uzay harmonikleri etkisi sadece rotorda gözlenirken, zaman harmonikleri hem statorda hem de rotorda etkisini gösterecektir. Bu durumda her bir zaman harmoniği bileşenin eşdeğer devresi, içinde her bir uzay harmoniği bileşeninin rotordaki etkisini gösterecek şekilde ifade edilir. Bu çalışma kapsamında ise asenkron motorun gerilim kaynağının bozucu harmonik bileşenleri içermediği kabul edilmiştir. Bu kabulün altında yatan temel neden ise, uzay harmoniklerinin makine iç yapısı kaynaklı olmaları ve hiçbir zaman tamamen yok edilememeleridir. Bu durum ise makine tasarım değişkenlerini etkileyen bir etken olacaktır. Uzay harmoniklerinin herhangi bir değişkene yada kayıba etkisinin tespit edilmesi durumunda, zaman harmoniklerinin etkisini tayin etmek daha kolay olacaktır ve basitçe tespit edilen etkileri katlayarak artıracağı söylenebilir.

Literatürde derin oluk etkisi ile ilgili bir çok çalışma varken, uzay harmonikleri ve derin oluk etkisini inceleyen çalışma sayısı oldukça azdır. Halbuki yukarıda bahsedilen durumun motor performansına etkileri kaçınılmazdır. Bu noktadan yola çıkarak bahsedilen etkinin incelenmesi ve sonuçlarının ortaya konması, bu konudaki eksikliğin giderilmesine katkı sağlayacağı düşünülmüş ve üç fazlı sincap kafesli asenkron motorda uzay harmoniklerinin oluşturduğu deri etkisinin değişik rotor çubuk kesitlerinde incelenmesi gerçekleştirilmiştir.

Tez kapsamında yapılan çalışmada Arçelik Motor İşletmesi tarafından üretilen üç fazlı sincap kafesli bir asenkron motorun verileri kullanılmıştır. Motor verileri ve sargı şeması kullanılarak motorun sargı fonksiyonu matematiksel olarak elde edilmiştir. Bu kısımda MATLAB'da yazılan bir kod kullanılmıştır. Bu kod yarıdımıyla tek ve üç faz amper-sarım fonksiyonları da üretilmiştir. Yine aynı kod yardımıyla toplam amper-sarım dağılımının harmonik bileşenleri elde edilmiştir.Ayrıca kullanılan motorun değişkenleri ve tasarlanan rotor çubuğu kesitleri kullanılarak manyetik analiz için gerekli olan bir takım değerler analitik olarak hesaplanmıştır. Ayrıca bazı ek hesaplamalar, çalışma sonuçlarının yorumlanabilmesi ve gerekli kontrollerin yapılabilmesi için çalışmaya eklenmiştir.

Sonraki aşamada gerçek rotor geometrisi AutoCAD 2014 programı yardımıyla çizilmiş ve manyetik model oluşturulmuştur. Oluşturulan manyetik modelin çözümünde en hızlı ve güvenilir sonucu, uygulamadaki örneklerden yola çıkarak sonlu elemanlar yönteminin vereceğine karar verilmiştir. Bu yönde bir benzetim programı seçilmesine ve Ansoft Maxwell 14 yazılımının tez kapsamında kullanılmasına karar kılınmıştır. Kullanılan yazılım sonlu eleman ağ ataması sırasında, deri etkisi kalınlığına göre ağ atanmasına izin vermekte ve deri etkisini tüm malzemelere uygulayabilmektedir.

Tez kapsamında dört farklı rotor çubuğu tasarlanmıştır. Bunlar sırayla yuvarlak, kare, derin oluk ve çift yollu rotor çubuğu olarak belirlenmiştir. Bu farklı kesit şekillerine sahip rotor çubuklarının iletken malzemeleri de değiştirilmiştir. Bu şekilde belirlenen özelliklerle manyetik benzetimler gerçekleştirilmiştir. Farklı harmonik bileşenlerin tamamı rotor çubuğuna uygulanmış yada bir kısmı elenerek rotor çubuğuna uygulanmıştır. Bu şekilde farklı harmonik bileşenleri farklı malzemeden yapılmış iletkenlerde ve kesitlerde incelenmesi yapılmıştır. Ayrıca rotor çubuk geometrisinin harmonik bileşenlerle olan etkileşiminin ortaya çıkarılması için farklı bir model daha kurulmuş ve bu modelin de benzetimleri çözdürülmüştür.

Elde edilen tüm çalışma sonuçları maddelendirilerek, nedenleri de açıklanarak verilmiştir. Yapılan çalışma sonunda elde edilen sonuçlar son derece olumlu ve yeni bir sincap kafesli asenkron motor tasarımının yapılmasına imkan verecek ölçüdedir. Sonuç olarak derin oluk etkisi ile uzay harmonikleri ve değişik rotor iletken kesitleri ve malzemeleri arasındaki ilişki ortaya koyulmuştur.

1. INTRODUCTION

Electrical energy has changed people's daily life a lot and it is used in all aspects of the applications such as industrial applications, telecommunication applications, consumer electronics and home applications. Since the area of usage and application of electrical power is too wide, many scientists are interested in electrical engineering applications.

As it is well known, there are two types of voltage that are AC voltage and DC voltage. Today, AC voltage is used in generation, transmission and distribution of electrical power. AC voltage can be directly used by the consumers also. DC voltage is usually generated after distribution of the AC voltage by the final consumer. This process is generally done by power electronic converters and DC voltage is used in consumer electronics, telecommunication and industrial applications.

Each voltage type has its own characteristic and results in currents that have the same characteristics. AC current has a frequency value and changes its direction periodically. Whereas, DC current's frequency is 0 and the current never changes its direction. These differences between this two type of currents arise different problems in real life applications. However, there is a common problem, which is the skin effect phenomenon. Because of the switching in power electronic circuits the DC current has a frequency value in those applications. Skin effect depends on the current frequency. Hence, skin effect occurs in both AC and DC current applications.

There is another well known phenomenon in AC machines, which is deep bar effect. Deep bar effect usually encountered in induction motors because of the construction of the machine. Deep bar effect is a kind of skin effect principally. It can be defined as the result of skin effect under an alternating magnetic field.

This thesis concentrates on deep bar effect in a squirrel-cage induction motor. Since skin effect and deep bar effect are related subjects principles of the both subjects were covered in this thesis.

1.1 Purpose of Thesis

This study aims to develop a relation between space harmonics and deep bar effect. It is also aimed that to develop the effect of rotor bar geometry on induced harmonic components. According to results a future work will be done about machine design.

1.2 Literature Review

Deep bar effect is related to skin effect. That is why skin effect studies in the literature should be examined to understand the deep bar effect effect better. The basics of the skin effect was built by James Clark Maxwell. After Maxwell, in 1883 Harace Lamb developed mathematical equations of the skin effect. In those years electricity and alternating current was a popular research subjects and many scientists investigated these subjects. After developing the mathematical basics of the skin effect, Oliver Heaviside made first investigations skin effect in different cross-section conductors in 1885.

It is seen that in early 20th century, advanced mathematical tools were used to examine skin effect. In 1929, H.B. Dwight investigated the skin effect in round and flat cross-section conductors and he adapted Bessel functions for skin effect problem by using his studies [1]- [2]. Because skin effect was expressed in complex plane, it was remarkable to use Bessel functions to solve the skin effect problem. His study leaded to many researchers to use the Bessel functions to examine the skin effect.

In 1942, Harold A. Wheeler compiled all of the skin effect formulas published in the literature till that date [3]. His study provided a common notation in skin effect problem and general expressions were accepted by the researchers. Wheeler used many scientists' valuable studies in his publication. These scientists can be listed as Oliver Heaviside, Steinmetz, S.A. Schelkunoff, Stratton and Harnwell [3].

Industrial revolution showed its impact in 19th century extremely and this revolution leaded to a necessity for more powerful and power efficient machines. As a result, high power alternating current machines started to use in 20th century. The demand on use of alternating current machines increased in those years and a lot of new problems occurred in applications. These problems in the industry directed researchers to solve and research alternating current machine problems deeper. In 1951, F.H. Douglas

examined the skin effect for deep rotor bar induction motor and developed the basics of deep bar effect [4]. A similar study was done for squirrel-cage induction motor in 1954 [5].

The analytical solution of the skin effect and deep bar effect is very difficult since both problem depend on the time and geometry. The analytical solution is many times obtained by second or higher order differential equations. That is why analytical solution does not exist for some problems and even if it exists, solution takes very long time. Numerical solution methods are used for these problems usually. The common numerical method is finite element method for skin effect and deep bar effect. FEM is actually used in solving any kind of electrical machine problems. This method was first used by P.Silvester in the late 1960s [6]- [7]. His studies were a milestone in electrical machine problems. FEM has been widely used to investigate electrical machine problems after his studies. He is also the author of the first FEM book for electrical engineers [8] FEM requires a computer and those days computers were started to use in scientific problems. Hence, a lot of study completed about skin effect and deep bar effect after late 1960s.

Today power electronic circuits are frequently used in applications. In these applications switching frequency starts from the utility frequency and it gets values at kHz levels usually. For some applications this level can reach to MHz levels. Hence, the skin effect has become a significant problem in power electronic circuits also. There are many studies about this research area but Marian K. Kazimierczuk is a leading researcher in this subject. One of his study is about comparison of different methods to analyze skin effect which gives very helpful approaches to analyze the skin effect problem [9].

In recent years, energy efficiency has become a very substantial subject in electrical engineering. Since fossil energy sources will be consumed in near future, use of renewable energy has become the main topic of scientists. In this regards, the importance of electric vehicles has increased. Electrical vehicles use electrical machines and power electronic converters and efficiency in these systems is very important. Skin effect and deep bar effect are also considerable in efficiency. Hence, there are some new studies about these subjects in the literature [10], [11], [12].

Skin effect and deep bar effect have a very old history in the literature. However these subjects maintain their popularity among the researchers. Efficiency requirements in applications and development of new techniques in electrical machine design and power electronic converters pushes the researchers to make new studies about these phenomenons. This literature review and new trends in electrical machines sufficient to make a new research about these subjects.

1.3 Assumptions

In this thesis, some important assumptions were made to perform some calculations easier and to make proper comparisons.

In the thesis a real induction motor's parameters are used. The original rotor bar cross-section shape was changed in the study but the cross-section area was always kept constant.

The rotor bar current was calculated for original motor and this value was used as a reference value for other bar profiles and materials. Otherwise, a proper comparison could not be made. Rotor bar current value changes the deep bar effect in the motor and rotor bar current value also depends on material and bar geometry. To make comparisons between rotor bar types the rotor bar current should be kept constant because the point in this study is space harmonic effect in the rotor.

Another important assumption was that the squirrel-cage induction motor was supplied from a pure and balanced three-phase voltage source. That means there would not be any time harmonic component in the machine.

2. SKIN EFFECT AND DEEP BAR EFFECT

2.1 Skin Effect

A current carrying conductor's current distribution depends on the the current characteristic. If the current were time-invariant then the current distribution in the conductor would be uniform. However, if the current is time-variant then this time current distribution is not uniform . A time varying current induces its own magnetic field and according to Lenz's law to attenuate the primary magnetic field there will be induced currents, which are called as eddy currents. Because of those induced eddy currents in the conductor, current distribution will be different this time. Eddy currents starts to circulate in the conductor and as a result, current density in the conductor's center decreases and the conductor current tends to flow near the surface of the conductor [13]. This effect is called as skin effect and skin effect depends on frequency of conductor current. If the current frequency is high, conductor current starts to flow in a very narrow band in the conductor and that narrow band is called as penetration depth.

Pure DC current's current distribution in a conductor is uniform and to calculate the conductor's resistance whole cross sectional area can be used. However, conductors that carrying time-variant current resistance depends on the frequency of the current. As the frequency increases, penetration depth decreases and effective cross-sectional area of the conductor decreases. The conductor resistance increases, as a result. The increment in the conductor resistance escalates power loss in the conductor [13].To analyze skin effect basics, a semi-infinite square conductor can be used. Assume thickness of the conductor is infinite and magnetic field intensity vector is in z direction. One-dimensional model can be used in this case. If the magnetic field intensity is sinusoidal, the magnetic field intensity can be expressed as follows [13].

$$\mathbf{H}(t) = a_m H_z cos(\omega t). \tag{2.1}$$

where $\mathbf{H}$, a_m, H_z, ω and t are magnetic field intensity vector, unity vector, magnitude of the magnetic field intensity, angular frequency and time respectively.

The magnetic field intensity is defined by a second order differential equation. This equation is also linear and homogeneous and can be expressed in phasor form [13].

$$\frac{d^2 H_z(x)}{dx^2} = j\omega\mu\sigma H_z(x) = \gamma^2 H_z(x). \tag{2.2}$$

where μ and σ permeability and conductivity of the conductor and the complex propagation constant is noted by

$$\gamma^2 = j\omega\mu\sigma. \tag{2.3}$$

To write the penetration depth, the term j can be substituted as follows

$$\sqrt{j} = \sqrt{e^{j\frac{\pi}{2}}} = e^{j\frac{\pi}{4}} = \cos(\frac{\pi}{4}) + j\sin(\frac{\pi}{4}) = \frac{1+j}{\sqrt{2}} \tag{2.4}$$

$$\gamma = \sqrt{j\omega\mu\sigma} = (1+j)\sqrt{\frac{\omega\mu\sigma}{2}} = (1+j)\sqrt{\pi\mu\sigma f} = \frac{1+j}{\delta_w} \tag{2.5}$$

Here f represents the frequency of the conductor current.

$$\delta_w = \sqrt{\frac{2}{\omega\mu\sigma}} = \sqrt{\frac{\rho_w}{\pi\mu_r\mu_0 f}} \tag{2.6}$$

where ρ denotes resistivity of the conductor, μ_r, is relative permeability, μ_0 is permeability of free space and δ_w is penetration depth.

Penetration depth equation depicts that skin depth is proportional to the conductor resistivity and inversely proportional to conductor permeability and current frequency. In other words, skin depth depends on the conductor material and conductor current frequency. Another important point is resistivity of a conductor related to ambition temperature as a result skin depth is related to ambition temperature.

Skin depth of a copper conductor is given in Table 2.1 [13] and frequency effect is demonstrated in Figure 2.1. In Figure 2.1 as the frequency increase, the current concentrates near the conductor surface and especially current density is very high
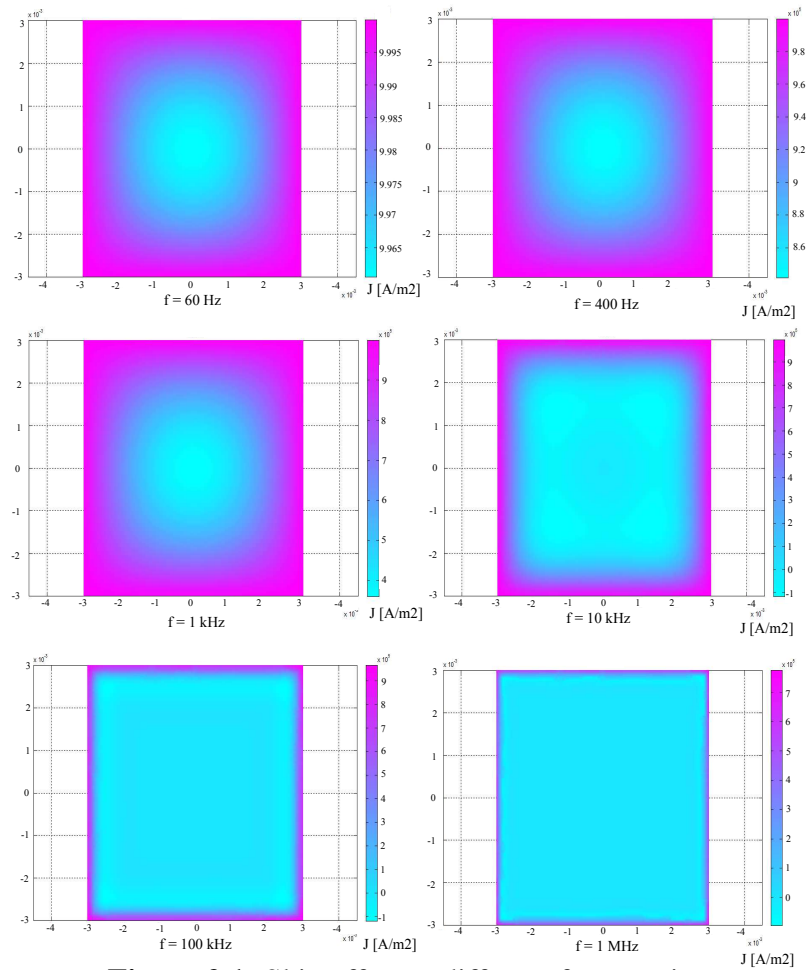
Figure 2.1: Skin effect at different frequencies.

at sharp corners. Since examined conductor cross-section area is square, the current tends to flow at the corners. However, if the cross-section area shape was different, for example round cross-section, the current would again flow near the surface but this time current density at near the surface would be homogeneous.

In Figure 2.1, current density looks nonuniform for 60 Hz frequency level because of the color-map default settings but if the current density scale J is examined, the current distribution is almost same for that frequency. That is because of the conductor thickness. According to Table 2.1 for 60 Hz frequency, the skin depth is 8.53 mm where examined conductor thickness is 6mm. Since the skin depth is greater than conductor thickness, skin effect at 60 Hz for this conductor can be ignored. However, for 400 Hz the skin depth 3.3mm which is very close to conductor thickness. Skin effect and losses due to skin effect should be taken into account at this time.

It should be stated that for the analyzes above, there is no magnetic field applied to conductor. Eddy currents that induced in the conductor is just because of conductor's

Table 2.1: Skin depth for copper at $20°C$ [13].

Frequency	Skin Depth δ_{cu}
60 Hz	8.53mm
400 Hz	3.3mm
1 kHz	2.53mm
10 kHz	0.66mm
20 kHz	0.467mm
100 kHz	0.209mm
1 MHz	0.066mm

own magnetic field and circulation currents flow in the center of the conductor in both directions. Since their magnitudes are same, the total current in the center of conductor is zero. However, if there is an external magnetic field that is applied to conductor, then current distribution would be very different. This situation will be discussed in advance chapters.

2.2 Deep Bar Effect

Skin effect depends on frequency and conductor material as it is given in previous section. However, skin effect is not just affected by those parameters, but also affected by the magnetic field applied to the related conductor. According to Faraday's law, a conductor in a time-variant magnetic field induces voltage across the conductor and if conductor terminals are connected, induced currents start to flow. In the light of this law, if a time-variant magnetic field is applied to a current carrying conductor, it increases induced eddy currents in that conductor. As a result, current accumulates to a certain area that is defined by the applied magnetic field direction and conductor current direction.

The effect mentioned above is a well-known phenomenon in squirrel-cage induction machines and it is called as deep bar effect or current displacement in the literature. Current displacement in squirrel-cage induction machine's rotor bars changes dynamic response of the machine. In this study, rotor bars in squirrel-cage induction machine are used as conductor model. Required explanations and related mathematical equations are given considering that model.

In a squirrel-cage induction machine, the flux that generated in the stator, passes through air gap, reaches rotor, and completes its loop by using a symmetric path.

Stator magnetic field induces a voltage across the rotor bars. Since the rotor bars are short-circuited, rotor bar currents start to flow. Rotor bar currents create their own magnetic field. Some amount of rotor magnetic flux completes its path through rotor bars, which is called as leakage flux. This leakage flux, as it is explained above, induces eddy currents in rotor bars. The rotor bar current accumulates in some certain areas due to increasing eddy currents.

In Figure 2.2, the current distribution in a rotor bar is shown for 0 Hz current case.
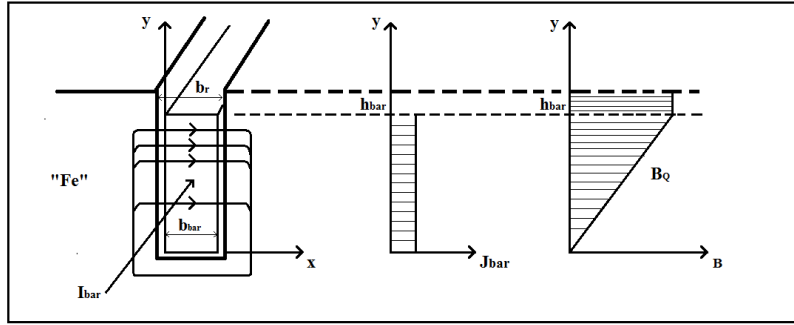
Figure 2.2: Current distribution in a rotor bar for DC bar current.

Demonstrated current and magnetic field distributions in a rotor bar can be derived simply by using Ampere's law.

$$\oint \mathbf{H} \, \mathbf{ds} = H_Q(x)b_r = \mathbf{J} \, b_{bar} \tag{2.7}$$

$$B_Q(x) = \mu_0 \, J \, \frac{x b_{bar}}{b_r} = \mu_0 \frac{I_{bar}}{b_r} \frac{x}{h_{bar}} \quad , \quad 0 \le x \le h_{bar} \tag{2.8}$$

where B_Q, J, b_{bar}, b_r, h_{bar} and I_{bar} denotes magnetic field intensity vector of the rotor slot, current density vector rotor bar, width of rotor bar, width of rotor slot, height of the rotor slot and current of the rotor bar respectively.

$$B_Q = \mu_0 \frac{I_{bar}}{b_r} \quad , \quad h_{bar} \le x \le h_Q \tag{2.9}$$

Since frequency for this case is 0 Hz, then the current distribution is uniform and current distribution function is as follows.

$$J = \frac{I_{bar}}{A_{bar}} \tag{2.10}$$

Here, A_{bar} is cross-sectional area of the rotor bar.

In Figure 2.2, slot flux density increases linearly with the slot height and it can be said that the leakage inductance of the slot increase as the height of the slot increases [14].

The example above explains the current and magnetic field response for 0 Hz in other word DC current case. However, induced rotor currents and rotor magnetic field have alternating characteristics in AC machines and the effect of eddy currents cannot be ignored.

Assume there is a rotor bar current flow into the paper plane and there is leakage magnetic field from left to right. Eddy currents are induced as it is mentioned before to decrease the slot magnetic field. As a result, eddy current magnetic field direction will be in reverse direction, which is from left to right. In this case, eddy currents start to circulate in the conductor and their direction is the same with the bar current at the upper region and in reverse direction at the lower region [14]. It is represented in the Figure 2.3.
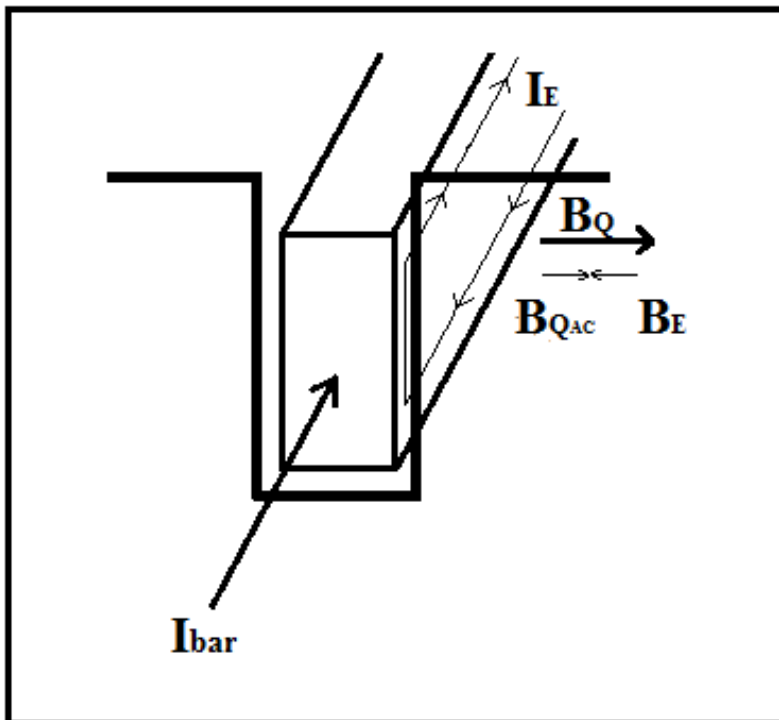

Figure 2.3: Induced Eddy currents in a rotor bar.

The current density distribution for this case can be calculated by using Maxwell's equations [15].

$$\nabla \times \mathbf{E} + \frac{d\mathbf{B}}{dt} = 0 \tag{2.11}$$

$$\nabla \times \mathbf{H} = \mathbf{J} + \frac{d\mathbf{D}}{dt} = 0 \tag{2.12}$$

where *E*,*H*,*J* and *D* are electric field vector, magnetic field intensity vector, current density vector and displacement vector respectively.

Since electric field change is relatively small in this application, the displacement current term **D** in Equation **2.12** can be neglected [15].

$$\nabla \times \mathbf{H} = \mathbf{J} \tag{2.13}$$

$$\nabla \times \frac{J}{\sigma} = -\mu \frac{d\mathbf{H}}{dt} \tag{2.14}$$

$$\nabla \times J = -\mu\sigma \frac{d\mathbf{H}}{dt} \tag{2.15}$$

$$\nabla \times \mathbf{J} \times \mathbf{H} = -\nabla^2\mathbf{H} = \nabla \times \mathbf{J} \tag{2.16}$$

$$\nabla^2\mathbf{H} = \mu\sigma \frac{d\mathbf{H}}{dt} \tag{2.17}$$

where $\mathbf{B} = \mu\mathbf{H}$ *and* $\mathbf{J} = \sigma\mathbf{E}$.

$$\frac{\partial^2\mathbf{J}}{\partial z^2} - jm'^2\mathbf{J} = 0 \tag{2.18}$$

$$J = A'\cosh(\sqrt{j}\,m')z + B'\sinh(\sqrt{j}\,m')z \tag{2.19}$$

where $m' = \sqrt{\mu\sigma_0\omega}$ and if $z = 0$, $\mathbf{H} = 0$ and σ_0 is conductivity of the free space. A' and B' are constants.

$$\nabla \times J = 0 \ , \ \frac{\partial J}{\partial z} = 0 \tag{2.20}$$

11

$$\frac{\partial J}{\partial z} = A'' \cosh(\sqrt{j}\, m')z + B'' \sinh(\sqrt{j}\, m')z = 0 \qquad (2.21)$$

$$J = A' \cosh(\frac{1+j}{2})m'z \qquad (2.22)$$

$$J = A'[\cosh(\frac{m'z}{\sqrt{2}})\cos(\frac{m'\,z}{\sqrt{2}}) + \sinh(\frac{m'\,z}{\sqrt{2}})\sin(\frac{m'\,z}{\sqrt{2}})] \qquad (2.23)$$

Equation **2.23** is analytical expression of current density distribution of a rotor bar under a alternating magnetic field. As it is seen from the Equation **2.23**, current distribution function is much more complex then the first case. In Figure 2.4 current density distribution of a rotor bar is given.
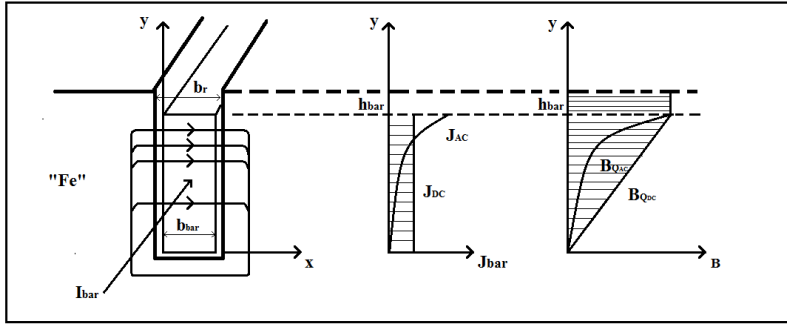
Figure 2.4: Current distribution in a rotor bar under an AC magnetic field.

Figure 2.4 points out that current density increases near the conductor surface and magnetic field curve has a similar form with current density. One can say that the effective resistance of the conductor rises since the effective cross-section area decreased. Similarly, since the slot magnetic field decreased, the leakage inductance also diminished [16]. As a result the AC resistance and inductance of the rotor bar should be corrected. Fixed resistance and inductance values can be calculated by deriving Equation **2.23**.

$$\xi = h_{bar}\sqrt{\pi f_r \mu \kappa \frac{b_{bar}}{b_r}} \qquad (2.24)$$

$$k_R = \xi \frac{\sinh(2\xi) + \sin(2\xi)}{\cosh(2\xi) - \cos(2\xi)} \qquad (2.25)$$

$$k_L = \frac{3}{2\xi}\frac{\sinh(2\xi) - \sin(2\xi)}{\cosh(2\xi) - \cos(2\xi)} \qquad (2.26)$$

Here k_R represents reduction coefficient for rotor bar resistance and k_L represents reduction coefficient for rotor bar inductance.Equations (**2.25**) and (**2.26**) clearly explains the effect of alternating magnetic field in a conductor. This effect depends on and increases with rotor frequency, electric conductivity of the bar, height of the bar and permeability of the bar conductor [16].

2.2.1 Impact of deep bar effect in squirrel-cage machines

Current displacement in rotor bars in a squirrel-cage machine changes the dynamic response of the machine. This effect can be an advantage or a disadvantage in different applications. The current displacement increases rotor resistance and this increment leads to also an increment in motor's breakdown torque and start-up torque. As a result, for an application that requires high breakdown or start-up torque rotor bars can be designed as deep rotor bar or double-squirrel cage rotor. However, if an induction motor is supplied from an inverter, there will be a significant multiplication in rotor harmonics, Since current displacement increases the resistance of the rotor, in this case rotor copper losses gets a higher value that decreases motor efficiency and results in cooling problems. Moreover, even if induction motor is supplied from a pure sinusoidal source there will be again harmonic components in the rotor currents. That is because MMF distribution is not sinusoidal in alternating current machines. Mentioned harmonics are called as space harmonics that results from the construction of the machine and can not be avoided.

There are lots of design considerations for an induction machine and rotor bar design is a substantial part of this process. Since, rotor bar material and shape have a significant effect in motor dynamics. It also affects the production and test procedure of an induction machine. According to IEEE standards, high power induction motor's short circuit tests should not be done at its rated frequency [17]. During the short circuit test, rotor does not rotate and short circuit current flows in rotor bars. Due to skin effect, this short circuit current concentrates at near the rotor bar surface. The motor that under this test is not designed to carry those short circuit currents as steady a state condition. That is why performing short circuit test at rated frequency can lead an insulation failure. To avoid this failure related standard offers to perform this test at reduced frequency level such as half of the rated frequency [17].

2.3 Harmonics and Electrical Machines

Two types of harmonic concerned with electrical machines. The first one is time-domain harmonics, which comes from the voltage source. The other one is winding-domain harmonics, which arises from the construction of the machine. Time-domain harmonics are related to utility system and voltage source and elimination techniques are different from space harmonics whereas space harmonics are related to winding distribution in the machine. Hence, to eliminate a space harmonic component machine construction design should be revised. Even though origin of these harmonic types are different, their mathematical analyzes can be done by the same mathematical tool that is Fourier transform. This study's aim is to investigate the effect of rotor bar shape and material to the rotor bar current distribution and this topic is related to MMF distribution in the air-gap. Since air-gap flux contains harmonic components, induced rotor currents also contains harmonic components. That is why; space harmonics were examined rather than time-domain harmonics in this study.

2.3.1 MMF distribution in airgap

Two-pole, three-phase, 6 slots induction machine's stator windings can be taken as a reference to examine production of MMF distribution in an AC machine. Figure 2.5 depicts a cross-sectional view of an induction machine.

Each phase coil in Figure 2.5 has N turns and each phase current is balanced and symmetric. A single phase MMF distribution will be investigated for this case. Since this machine has six slots and coils span $180°$ electrical degrees, it is a full-pitch coil [16]. This type of winding is called as concentrated windings. Figure 2.6 shows the generated winding function for one phase.

By assuming the phase current as 1 A, MMF distribution of one phase would be rectangular function. This function's harmonic components can be calculated by using Fourier transform. Required equations for Fourier transform are given in Equations **2.27**-**2.30** [15].
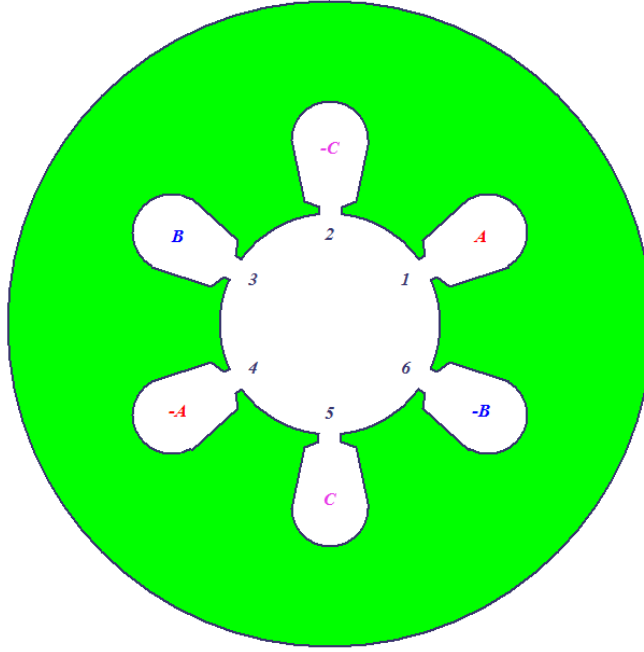
14

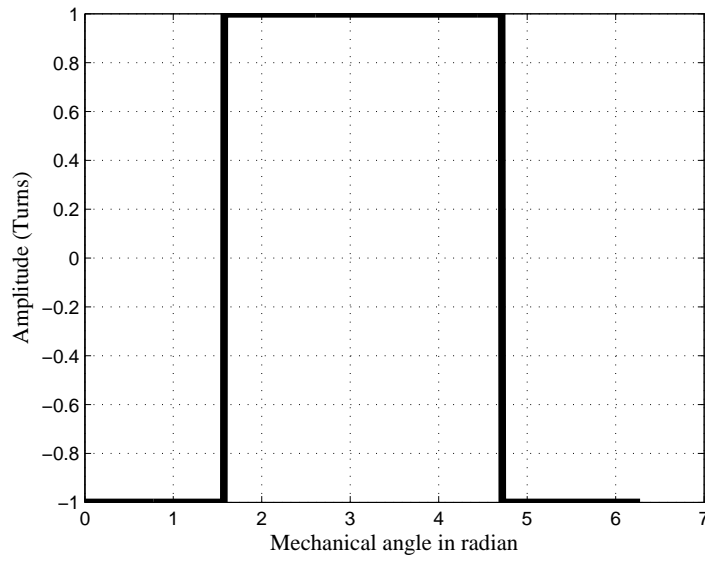**Figure 2.5**: An example winding lay-out of induction machine for 6 slots.

Figure 2.6: Single phase winding function of concentrated winding.

$$F(t) = A_0 + \sum_{n=1,2,3...}^{\infty} [A_n \cos(\frac{2\pi}{T}nt) + B_n \sin(\frac{2\pi}{T}nt)] \tag{2.27}$$

where A_n and B_n are Fourier coefficients, A_0 is the d.c. component of the waveform.

$$A_n = \frac{2}{T} \int_0^T f(t) \cos(\frac{2\pi}{T}nt dt) \tag{2.28}$$

$$B_n = \frac{2}{T} \int_0^T f(t) \sin(\frac{2\pi}{T}nt dt) \tag{2.29}$$

15

$$A_0 = \frac{1}{T} \int_0^T f(t)dt \tag{2.30}$$

where T,n,t are period of the waveform, order of harmonic and time.

There are some symmetry conditions that eliminates some certain harmonic components. These conditions are given below.

- $A_0 = 0$. If the waveforms positive and negative areas are equal. Which means average of the waveform is zero.

- $f(\theta + \pi) = -f(\theta)$. Waveform is symmetric respect to x axis. Even harmonics do not appear in the final equation.

- If there is symmetry respect to origin, then final equation contains only cosine terms. $B_n = 0$.

- $f(-\theta) = -f(\theta)$, In this case final equation contains only sine terms. $A_n = 0$.

Since the ampere-turn function has quarter-wave symmetry, even terms are canceled and only sinusoidal terms appear in the final expression. Fundamental component of this function is given in Equation **2.31** [18].

$$\mathscr{F}_{ag1} = \frac{4}{\pi} \frac{Ni_a}{2} \sin(\theta_a) \tag{2.31}$$

Figure 2.6 and Fourier analysis of the related function indicates that MMF distribution of this function has serious harmonic components and very far away from sinusoidal waveform. Because of this reason, concentrated winding usually is not preferred in applications. Distributed winding is a common option to reduce space harmonic components of the MMF distribution function [18]. Figure 2.7 represents an example for a distributed winding lay-out.

Since each coil does not span over 180 degrees in this case, sum of harmonic components of a single phase winding is greater than fundamental harmonic component [16]. This explanation defines winding factor actually. Distributed winding has a reduction constant that is winding factor. This constant is significant because it shows its effects on MMF distribution, induced voltages, induced currents and induced
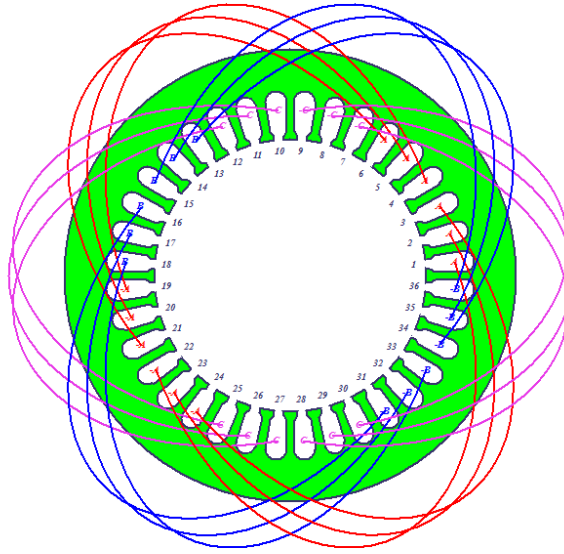
Figure 2.7: An example winding lay-out for distributed winding.

torque values in the machine. Figure 2.8 demonstrates winding function for one phase for a distributed winding.
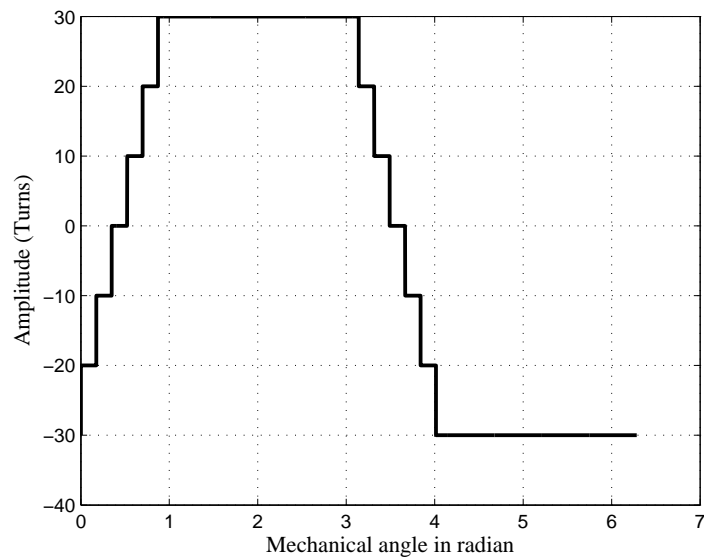

Figure 2.8: Winding distribution function of distributed winding for single phase.

As it is seen from Figure 2.8, winding function is stairs shaped function that is closer to sinusoidal waveform. Fourier transform can be applied to this function to investigate harmonic components. The result shows that this type of winding distribution can reduce higher harmonic orders. Equation **2.32** figures out the fundamental component of the MMF distribution function [18].

$$\mathscr{F}_{ag1} = \frac{4}{\pi} \frac{k_w N i_a}{p} \sin(\frac{p}{2}\theta_a) \tag{2.32}$$

$\mathscr{F}_{ag1}$ is fundamental component of phase a MMF distribution, N_a is number of turns for phase a, k_w is winding factor, i_a is current of phase a, p is number of poles and θ_a is geometric angle for phase a.

Winding factor is seen in equation **2.32** that is the main difference between the concentrated winding and distributed winding. Winding factor is between 0.85 and 0.95 many times for three-phase windings [18]. Winding factor contains two different coefficient actually that are winding distribution factor and chording factor. They are described by the Equations **2.34** and **2.35** [16].

$$K_{w_e} = K_{qe}K_{ye} \tag{2.33}$$

$$K_{qe} = \frac{\sin(\frac{e\pi}{6})}{q\sin(\frac{e\pi}{6q})} \tag{2.34}$$

$$K_{ye} = \sin(\frac{e\pi y}{2\tau}) \tag{2.35}$$

where K_{qe}, K_{ye}, e, q, y and τ are winding distribution factor, chording factor, space harmonic order, number of slot per pole per phase, chording ratio and pole pitch respectively.

Equations **2.33** and **2.34** indicates that winding factor depends on harmonic order also. Hence, effect of harmonic order on winding factor should be taken into account while calculating the MMF distribution.

Reducing higher order harmonic components is another topic itself. Some certain harmonic orders can be reduced or canceled by changing the geometry of the stator slots and by changing slot locations in stator. There are studies in the literature about this topic [19], [20]. In this study, instead of eliminated harmonic levels, conventional distributed winding type was preferred to investigate harmonic effects better.

Except from the fundamental component of the space harmonic, other components can be also calculated by modifying the equation **2.32**.

$$\mathscr{F}_{ag1} = \frac{4}{e\pi} \frac{k_{w_e} N i_a}{p} \sin(\frac{p}{2} e\theta_a) \tag{2.36}$$

Here e represents the order of the space harmonic and it is an odd number. Fundamental and higher order harmonics MMF distribution can be calculated by using the Equation **2.36**.

A three-phase induction machine has three symmetric windings in stator and each winding produces its MMF distribution. Since these windings are located symmetric and balanced, they produce the same MMF distribution that shifted by 120° in machine space. These windings are supplied by a three-phase balanced and symmetric voltage source thus; there will be symmetric three-phase currents flowing in the stator windings.

$$i_a = I_m \cos(\omega t) \tag{2.37}$$

$$i_b = I_m \cos(\omega t - 120°) \tag{2.38}$$

$$i_c = I_m \cos(\omega t + 120°) \tag{2.39}$$

where I_m denotes maximum phase current, ω_e denotes the angular frequency of the phase current and t denotes time.

Each phase winding defines an ampere-turn function.

$$\mathscr{F}_a = \frac{4}{e\pi} \frac{k_{w_e} N i_a}{p} \sin(\frac{p}{2} e\theta_a) \tag{2.40}$$

$$\mathscr{F}_b = \frac{4}{e\pi} \frac{k_{w_e} N i_b}{p} \sin(\frac{p}{2} e\theta_a - 120) \tag{2.41}$$

$$\mathscr{F}_c = \frac{4}{e\pi} \frac{k_{w_e} N i_c}{p} \sin(\frac{p}{2} e\theta_a + 120) \tag{2.42}$$

These ampere-turn functions operate together in the machine and they produce a final ampere-turn function in the machine. The final equation can be calculated by using trigonometrical substitutions and summing the Equations **2.40**, **2.41** and **2.42** [18].

$$\mathscr{F}(\theta_{ae}, t) = \frac{3}{2} F_{max} \sin(\theta_{ae} - \omega_e t) \tag{2.43}$$

Here, θ_{ae} represents the electrical angle. Equation **2.43** depicts that there is an ampere-turn function whose magnitude is constant but it changes its position in the machine by the time. This definition is rotating magnetic field's definition itself. There is a rotating MMF distribution in the machine which defines rotating magnetic field in the machine. During derivation process of Equation **2.43**, it is deduced that summation of every third component of the MMF distribution of each phase is zero . The third harmonic component in the machine can be eliminated simply by using three-phase winding. Thus, calculation of the third harmonic components in three-phase machine is not required and they can be directly removed from the equations. In this thesis, third harmonic components was not investigated also.

Time harmonics are not included in related equations but calculating time harmonic components are not difficult. Time harmonic components are determined by the phase currents. Since phase currents are symmetric and balanced, the third component of the time harmonics are zero also. This can be proven by applying similar processes on the related equations. In the end, each time harmonic component defines its own space harmonic components. Equation **2.43** should be re-written for every time harmonic component by multiplying the angular electrical frequency by related time harmonic order.

2.3.2 Generated stator space harmonics

In previous section, airgap MMF distribution and its harmonic contents were explained. The effect of using three-phase winding and the results of Fourier transform of MMF functions were also given. To conclude these results a general expression can be written for generated stator space harmonic orders [21].

$$e = 6k_1 \pm 1 \tag{2.44}$$

where e represents harmonic order, k_1 represents a positive integer including zero. Generated harmonic components can be calculated by using the Equation **2.44**. Table 2.2 gives the results for a three-phase machine [21].

Table 2.2: Stator space harmonic orders.

k_1	0	1		2		3		4	
e	1	5	7	11	13	17	19	23	25

The equivalent circuit of an electrical machine should be revised to calculate the losses that caused by space harmonics and skin effect. Figure 2.9 demonstrates the revised equivalent circuit of an induction motor [22].
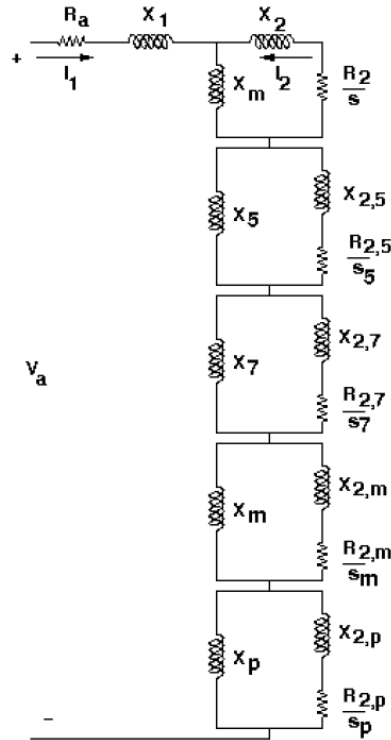

Figure 2.9: Equivalent circuit of induction motor including space harmonics [22].

Number of stator slots are significant for space harmonics. Increasing number of stator slots can reduce space harmonic orders because it pushes the MMF waveform closer to the sinusoidal waveform. Also, number of slots give an idea to where to stop calculating space harmonic components. If there are 24 slots in a machine's stator, then calculating 23rd harmonic order as a last term is enough for this machine. Because harmonic components that higher than 23rd order effects are very less in the machine and they can be ignored [15].

2.3.3 Induced rotor space harmonics

The generated magnetic field from the stator, induces voltage and current in the rotor and rotor magnetic field is induced as a result. Since generated magnetic field contains harmonic components, induced rotor magnetic field also contains harmonic

components. Moreover, harmonic effects in the rotor of an induction machine are much more heavy. The reason for that is each harmonic order that comes from the stator induces more than one harmonic order in the rotor side [21].

Stator and rotor phase numbers and pole numbers of an induction machine can be different or the same. If the number of phases and number of poles are equal in stator and rotor, then induced harmonics in the rotor are the same with the stator harmonics. However, if these numbers are not equal, then induced rotor harmonics would be different this time. Squirrel-cage induction motor's rotor has N_r number of rotor bar, which means rotor has N_r number of phases. Hence, induced harmonics in the rotor is determined by each harmonic order that generated by the stator. Equation **2.45** figures which harmonic orders are induced for a certain stator harmonic order [21].

$$e_2 = e + \frac{k_2 N_r}{P} \tag{2.45}$$

Here k_2 is an integer and P is number of pole pairs.

A 2 poles squirrel-cage induction machine that has 36 rotor bars can be given as an example. Induced rotor harmonic orders for the 7th stator space harmonic can be calculated by using Equation **2.45**. Table 2.3 shows the result for this example.

Table 2.3: Rotor space harmonic orders for given example.

k_1	0	1	-1	2	-2	3	-3
e	7	43	-29	79	-65	115	-101

The sign ($-$) indicates that related harmonic component rotates in the opposite direction of 7th harmonic. As it is seen from the Table 2.3 and Equation **2.45** rotor harmonics are multiplied by stator harmonics. The important point is higher order harmonics that are higher than number of slots in the stator can be neglected as it is mentioned before.

In this study, it was assumed that the same harmonic orders were induced in the rotor and remains were ignored to procure simplicity in the model.

Stator magnetic field harmonic components and rotor magnetic field harmonic components produces a resultant magnetic field and this magnetic field induces a torque in the machine. These harmonic components affects also current distribution

in the machine conductors. Especially current distribution in rotor bars are substantial because many parameters such as losses, efficiency, start-up and breakdown torque are affected by rotor bar current distribution. In this chapter required mathematical equations, important points about these subjects, explanations and assumptions were given. All of the results were calculated and computed by given background information in this chapter.

3. FINITE ELEMENT METHOD

This chapter covers a brief information about finite element method and application of FEM to solve skin effect problem. In this study, FEM was used to analyze current density distribution in a conductor.

3.1 Finite Element Method Basics

Finite element method is a common numerical way to generate solutions for boundary value problems in mathematics. It was used first in 1940s in civil engineering. Since the basics of method is convenient for any kind of engineering problem, the use of method spread any aspect of engineering. In 1950s it was used in aeronautics engineering. The adoption of the method is made in 1968 by Peter Peet Silvester [6]. Silvester was a pioneer in FEM and after his contributions FEM used in electrical engineering by many researchers.

The use of method was restricted in its early times because method is numerical method and solution requires a computer. Hence, development of the method has parallels with development of computer technology. Invention of personal computers lead to researchers access and use the method easier.

FEM enables to analyze complex geometries and it is widely used for analyzing electrical machines. Electrical machines problems contain a large number of differential equations. Although analytical solutions are required for these differential equations, it is usually not possible. Thus, a numerical solution is used that is FEM.

FEM divides the related geometry in smaller divisions and solves each division. In electrical machines FEM usually handles with electric and magnetic field distributions. These vector fields can be time dependent or analyzed materials can be non-homogenous, anisotropic or non-linear but method is still valid [23].

In electrical machines, the problem is defined by the geometry of the machine, used materials and Maxwell equations. There are some known parameters and FEM uses

these known parameters to solve unknown parameters. As a result, magnetic field distribution, current density distribution, induced electromagnetic force or torque and many other desired vector or scalar quantities can be computed by using FEM.

The method is widely used in engineering applications because of its advantages. These advantages ,especially for electromagnetic field analysis, can be summed up as following [23].

- Allows local analysis.

- Presents excessive field gradient, magnetic saturation and strength.

- Enables a reliable estimation for electric machines.

- Reduces manufacturing expenses.

In spite of these advantages FEM has some handicaps and these are listed below [23].

- Results are not exact solutions.

- Generating a mesh and using the method requires experience.

- To satisfy more approximate solutions number of elements should be increased, which results in longer computation time and requires more computer memory.

- Interpreting the results in a wrong way can cause a fatal error.

The finite element method consists of 4 main parts that are discretization of the domain, determine of the interpolation function, system equations and solution of the system. Brief explanations about each step are given.

3.1.1 Discretization of the domain

In this step, problem geometry is divided into subdivisions. Number of these subdivisions are significant because it directly affects the accuracy of the results and required computer memory. Each subdivision represents an element and those elements shape depends on the problem dimensions. If the problem is one-dimensional, then the element is a segment. If the problem is two-dimensional,

each element represents a surface and elements can be a triangle, rectangle or square. Lastly, if the problem is three-dimensional, this time each element represents a volume and elements can be triangular prism, a tetrahedron or a rectangular solid. Regarding the problem dimension these geometric objects are chosen and a mesh is generated for the whole domain. It can be deduced easily that number of the dimension of the problem increases the number of elements as a result the computation time and required memory is increased also.

3.1.2 Determine of the interpolation function

As it is mentioned before FEM uses known parameters to solve unknown parameters. To solve these parameters an interpolation polynomial should be chosen. The higher order of the interpolation polynomial leads to higher accuracy in results. However, using a higher order polynomial enhances the problem complexity and makes adoption of the method even harder.

3.1.3 System equations

In FEM, each element consists of nodes. The chosen interpolation function should be defined for each node to solve the required field problem. These functions defines a set of equation that establishes the system. The variational method or residual method can be used to establish the system [23]. These methods are Galerkin's method and Rayleigh-Ritz method. In this step discrete elements are unified.

3.1.4 Solution of the System

After all the steps mentioned above, the system can be computed by solving related functions for each node.

Today personal computers are usually enough to get quick results in $2D$ FEA. Thus, many softwares were released by commercial companies for FEA. These softwares provide user friendly interfaces and enables to use FEM easier. In this thesis, a computer software was used to compute the solutions, which is Ansoft Maxwell $v.14$. This software enables to assign mesh operation according to skin depth and applies skin effect in any kind of material.

In this thesis, FEM was used to compute magnetic field density and current density distribution in a conductor. Details of the FEM were not covered in this study but there are many precious references and reference [16] and [23] can be seen for further information.

4. MOTOR PARAMETERS AND COMPUTATION OF SPACE HARMONIC ORDERS

Before starting magnetic analysis, space harmonic orders should be computed. A real induction motor, which is $QS100L2 - A$ manufactured by Arcelik Motor Company was used to compute space harmonic orders and this motor's parameters were used to perform magnetic analysis. This chapter covers detailed information about motor parameters and space harmonic order computation process.

4.1 Motor Parameters

In this study Arcelik $QS100L2 - A$ three phase squirrel cage induction motor is used. Required motor parameters are given in Table 4.1- 4.4 to calculate and compute required values.

Table 4.1: Motor Nameplate values.

Nominal supply voltage	400 V
Nominal current	6.1 A
Rated speed	2890 rpm
Rated power	3 kW
Rated torque	9.96 NM
Frequency	50 Hz
Power factor	0.88
Efficiency	83%
Stator winding connection type	Y

Table 4.2: Motor constructional parameters.

Number of phases	3
Number of poles	2
Number of stator slots	36
Number of rotor bars	28
Airgap length	0.34 mm
Number of stator coils in one slot	29
Number of winding layer	1
Number of parallel branches	1
Rotor bar area	43.0609 mm^2

29

Table 4.3: Motor T equivalent circuit parameters.

Stator winding resistance, R_s 25°C	1.917Ω
Stator winding resistance 75°C	2.2955 Ω
Stator leakage reactance, X_{σ_s}	1.6537 Ω
Magnetizing reactance, X_m	104.524 Ω
Iron loss resistance, R_{Fe}	1.062 Ω
Rotor cage resistance per phase, R'_r	1.574 3Ω
Rotor bar resistance, R'_{rb}	1.0372 Ω
Rotor ring resistance per phase, R'_{re}	0.5379 Ω
Rotor leakage reactance,(unsaturated) $X'_{\sigma r}$	1.4891 Ω
Rotor leakage reactance,(saturated) $X'_{\sigma r}$	1.2988 Ω
Rotor leakage inductance,(unsaturated) $L_{\sigma r}$	$3.99583 \cdot 10^{-7}$ H
Rotor leakage inductance,(saturated) $L_{\sigma r}$	$3.48518 \cdot 10^{-7}$ H
Turns ratio, a	108.914

In Table4.2, the symbol ($'$) represents that the related parameter value is referred to the stator side.

Table 4.4: Motor power losses.

Stator copper loss	235.2 W
Rotor copper loss	133.6 W
Iron loss	116.15W
Additional losses	55.04 W
Mechanical losses	66.85 W

In the light of these parameters required magnetic values and harmonic orders can be computed.

4.2 Computation of Harmonic Orders

The motor that used in the study has 36 slots and it has a conventional full-pitch stator winding.Each stator slot has 29 coils. Winding distribution function can be computed easily now. To implement the winding function a MATLAB code was written and winding distribution for three phase is given in Figure4.1.

As a next step, ampere turn function can be computed. To compute ampere-turn function, the current value of each three phase should be calculated. The current value depends on the time. That is why a certain time value should be selected for further calculations. The instant 5*ms* was selected for all analyses. The reason was the fundamental component of current density, magnetic flux density, magnetic field intensity vectors and three phase ampere turn function reach their maximum value
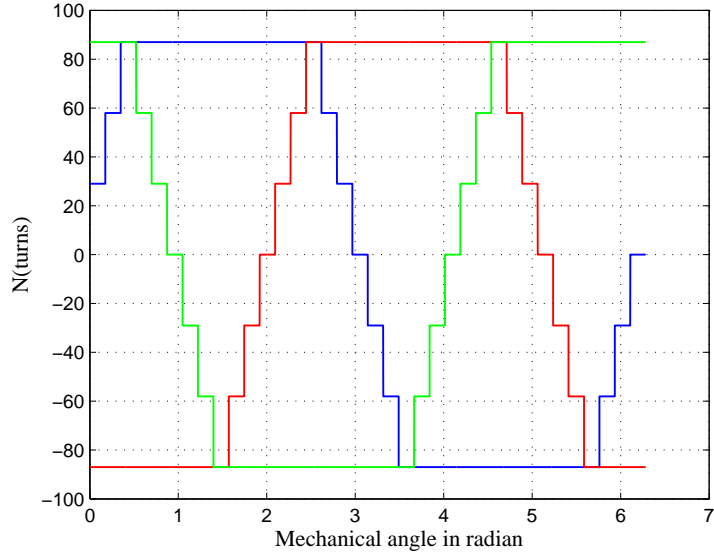
Figure 4.1: Winding distribution for three phase.

at the time 5*ms*. That means 5*ms* instant was the worst case to investigate in the machine.All calculations was done for that instant.

According to Equations **2.37**-**2.39** phase current values can be calculated. Three phase ampere-turn function can be calculated according to equation given below.

$$\mathscr{F}_{TOTAL} = 6.1 \cdot \sqrt{2} \cdot N_a - 0.5 \cdot 6.1 \cdot \sqrt{2} \cdot N_b + 0.5 \cdot 6.1 \cdot \sqrt{2} \cdot N_c \qquad \textbf{(4.1)}$$

Three phase ampere-turn function was computed according to equation above and the final ampere-function distribution in the machine is given in Figure 4.2.
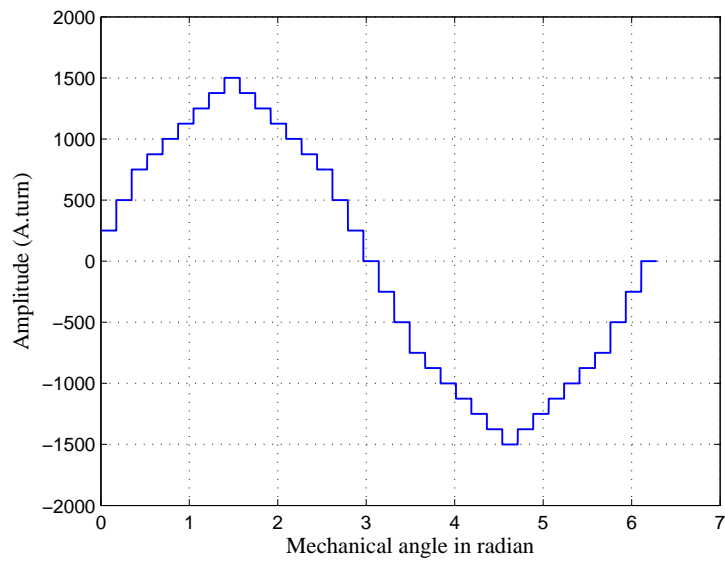
Figure 4.2: Total MMF function in the machine.

31

Hamonic orders in the machine can be computed by using the total MMF function. FFT was applied to total MMF function and also it was applied to Phase A ampere-turn function. Results are given in Figure 4.3 and in Figure 4.4.
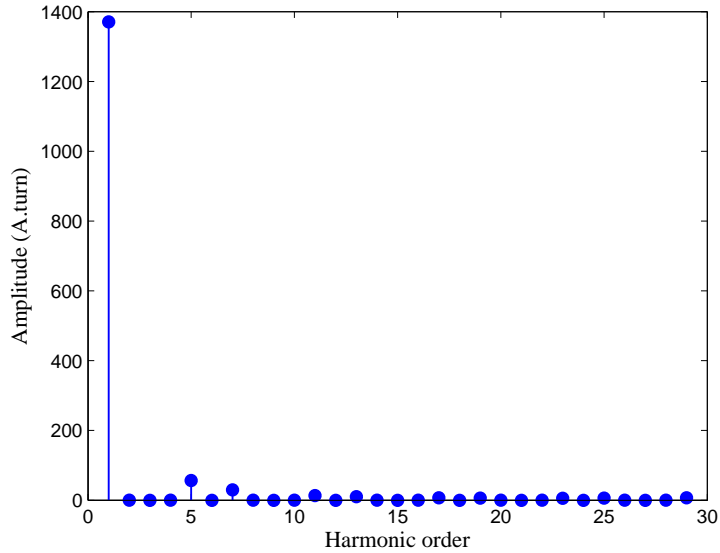
Figure 4.3: FFT result for total MMF function in the machine.
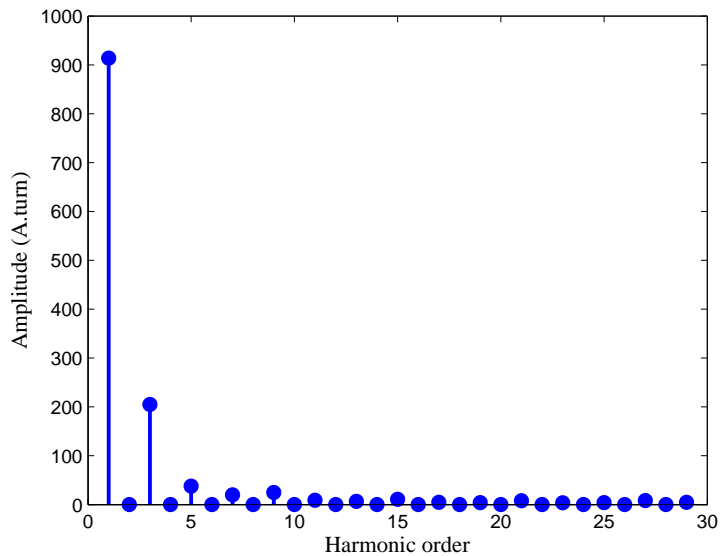
Figure 4.4: FFT result for Phase A ampere-turn function.

FFT results depicted that 3rd order harmonics were eliminated in the total MMF function which was an expected result. Detailed results are given in Table 4.5 and Table 4.6.

According to Equation **2.43**, the amplitude of the first harmonic component of the total MMF function should be 1.5 times greater than the amplitude of the first harmonic

Table 4.5: FFT result for Phase A ampere-turn function.

Harmonic order	Amplitude
1st	913.6766
3rd	205.0991
5th	37.6745
7th	19.8202
9th	24.9869
11th	8.7873
13th	6.7998

Table 4.6: FFT result for total MMF function.

Harmonic order	Amplitude
1st	1370.5149
3rd	0
5th	56.5118
7th	29.7303
9th	0
11th	13.1809
13th	10.1997

component of Phase A ampere-turn function. By using the results above $\frac{1370.5149}{913.6766} = 1.5$ which proves the computation result is correct.

Also winding function can be calculated by using Equation **2.33**, **2.34** and **2.35**. Since the stator winding is full-pitch, K_{ye} is equal to 1. As a result the winding coefficient is equal to 0.959. The winding coefficient can be calculated by using the results above also. Equation **2.43** was used to calculate winding coefficient. Winding coefficient was calculated as 0.956 by using related equations.

Analytical calculations and computation results are almost the same. Hence, computation results can be directly used in magnetic analysis.

Total MMF function waveform defines the induced voltage and current waveforms in the machine. Even if current or voltage amplitudes change in the machine, their harmonic component does not change. That is why rather than harmonic amplitudes of MMF function, ratio of each harmonic component with respect to first harmonic order is more significant. These ratios are given in Table 4.7.

The waveform of the total MMF function was computed above. RMS value of the total MMF function can be calculated. The relation between maximum value of the total MMF function and RMS value of it can be calculated also.

Table 4.7: Ratios of harmonic components in the machine.

Harmonic order	Ratio (%)
1st	100
5th	4.123
7th	2.169
11th	0.9617
13th	0.5147

$$\frac{max(\mathscr{F}_{TOTAL})}{RMS(\mathscr{F}_{TOTAL})} = 1.5449 \tag{4.2}$$

The ratio calculated above important for rotor current and leakage flux calculations, because nameplate values are RMS values. To calculate the maximum value of those magnitudes, the ratio calculated above will be used.

4.3 Required Calculations For Rotor

Since deep bar effect was investigated in this thesis, rotor current values should be determined. Each rotor bar's induced voltage was calculated by using power values of the motor [21].

$$E_{rb} = V_1 \cdot \frac{1}{1+\sigma_1} \cdot \frac{1}{2pqz_sk_w} \tag{4.3}$$

E_{rb} is induced rotor bar voltage for rated values, V_1 is voltage of single phase, σ_1 is Heyland distribution factor and z_s is number turns for each coil.

The induced rotor bar voltage was calculated 0.675V by using the Equation **4.3** where Heyland distribution factor is 0.204 [21]. The induced rotor bar current can be calculated by these known values [21].

$$I_{rb} = \frac{P_o + P_{F\&W}}{N_{rb}E_{rb}(1-s)} \tag{4.4}$$

I_{rb} is induced rotor bar current for rated values, P_o is output power, $P_{F\&W}$ is mechanical losses, N_{rb} is number of rotor bars and s is slip.

The induced rotor bar current is 168.44A. The calculated rotor bar current is rated value. In this study, the start-up instant was investigated. Hence, slip value was equal to 1 at that instant. An induction motor draws 4-7 times greater current values at the

Table 4.8: Harmonic Current Amplitudes and Current Density Values.

Harmonic order	Current Amplitude(A)	Current Density ($A\backslash mm^2$)
1st	1187.92	27.587
5th	48.98	1.137
7th	25.764	0.598
11th	11.424	0.265
13th	8.8405	0.142

start-up stage. It was assumed that this motor draws 5 times greater current than rated current at the star-up stage. This assumption does not affect the accuracy of the results. It just affects the amplitudes in the magnetic analysis. The induced rotor bar current is 842.2A under this condition. Harmonic components current amplitude values and current density values are given in Table 4.8.

4.4 Magnetic Calculations

In this study, four different type of bar was investigated. Cross-sections of investigated rotor bar geometries are given in Figure 4.5.
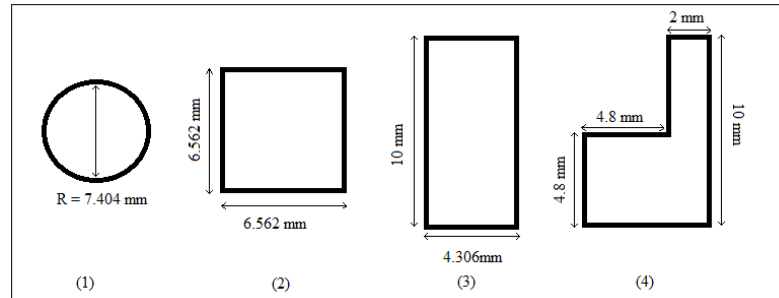
Figure 4.5: Cross-sections of investigated rotor bars.

Each rotor bar defines different leakage inductance and leakage flux values. These values can be calculated by using the equations given below [21].

$$L_{\sigma_{rb}} = 0.8\pi z_o p q l_r \lambda \, 10^{-8} \tag{4.5}$$

$$\lambda = \frac{h_1}{b_0} \tag{4.6}$$

$L_{\sigma_{rb}}$ is leakage inductance, z_o is number of conductors, l_r is length of rotor bar in cm and λ is magnetic conductivity factor. Leakage flux can be calculated by using the equations below.

35

Table 4.9: Harmonic current amplitudes and current density values.

Geometry	$L_{\sigma_{rb}}$(Unsaturated)	$L_{\sigma_{rb}}$ (Saturated)	$\phi_{sigma_{rb}}$
Circle	$3.1018 \cdot 10^{-7}$	$2.79162 \cdot 10^{-7}$	$118.436 \cdot 10^{-7}$
Square	$1.5509 \cdot 10^{-7}$	$1.39581 \cdot 10^{-7}$	$59.218 \cdot 10^{-7}$
Rectangle	$3.61886 \cdot 10^{-7}$	$3.25697 \cdot 10^{-7}$	$138.178 \cdot 10^{-7}$
Two way bar	$9.33996 \cdot 10^{-7}$	$8.40596 \cdot 10^{-7}$	$356.628 \cdot 10^{-7}$

$$N_{rb} \cdot \phi_{\sigma_{rb}} = L_{\sigma_{rb}} \cdot i \qquad (4.7)$$

where $\phi_{\sigma_{rb}}$ is leakage flux of rotor bar.

According to equations above and defined geometries leakage inductance and leakage flux values were calculated. Results are given in Table 4.9.

All of required calculations and computations are completed. These calculations were used as a reference for magnetic analysis results.

5. SIMULATION RESULTS

Magnetic analysis simulations was run after required calculations and computations. Current distribution results for 4 different cross-section and 2 different materials were obtained. All simulation figures are given in Appendix A.1 and Appendix A.2. In this chapter some detailed information is given for simulation results to interpret the results better.

Simulation results are given for copper rotor bar in Table 5.1 and Table 5.2. Simulation results for aluminum rotor bars are given in Table 5.3 and 5.4.

During the study, it was discovered that two-way rotor bar reacts 7th harmonic component much more than any type of rotor bar. To present this effect, a few more extra simulations was run. The important thing while investigating the effect of 7th harmonic component, the fundamental component of the magnetic flux density should be applied to the rotor bar. Otherwise the result would be deceptive. Because the 7th harmonic component of the rotor current creates too weak magnetic flux density that does not induce enough eddy current. However, in real application 1st harmonic component always exists and effects all of the other harmonic components in the rotor bar.

Another simulation model was developed to propound the reaction of two way rotor bar to the 7th harmonic component because of the reasons mentioned above. Results are given in Appendix A.3.

Table 5.1: Detailed simulation results for copper rotor bar.

Harmonic Order		1		1,5		1,7		1,5,7,11,13	
Current Denstiy ($A \backslash mm^2$)		Max.	Min.	Max.	Min.	Max.	Min.	Max.	Min.
Cross-section	Round	30.557	26.688	32.819	26.861	29.181	25.662	31.291	26.400
	Square	30.498	25.923	32.951	26.790	28.982	25.423	31.221	26.285
	Deep bar	35.078	23.053	38.196	23.874	33.182	22.512	36.075	23.231
	Two-way bar	32.663	28.858	35.075	26.855	31.169	25.134	33.392	26.266

Table 5.2: Detailed simulation results for copper rotor bar (continuation of previous table).

Harmonic Order		1,7,11,13		1,5,11,13		1,7,11		1,5,13	
Current Denstiy ($A \backslash mm^2$)		Max.	Min.	Max.	Min.	Max.	Min.	Max.	Min.
Cross-section	Round	29.008	25.617	32.648	26.815	28.534	25.476	33.283	27.004
	Square	28.782	25.352	32.746	26.718	28.257	25.177	33.470	26.966
	Deep bar	32.941	22.422	37.956	23.782	32.289	22.237	38.839	24.066
	Two-way bar	31.008	25.039	34.884	26.805	30.505	24.786	35.587	27.018

Table 5.3: Detailed simulation results for aluminum rotor bar.

Harmonic Order		1		1,5		1,7		1,5,7,11,13	
Current Denstiy ($A \backslash mm^2$)		Max.	Min.	Max.	Min.	Max.	Min.	Max.	Min.
Cross-section	Round	29.419	26.688	31.313	27.577	28.285	26.232	30.052	27.070
	Square	29.396	26.581	31.448	27.516	28.168	26.063	30.025	26.928
	Deep bar	32.203	24.817	34.719	25.675	30.694	24.295	33.035	25.066
	Two-way bar	30.337	24.725	32.344	27.737	29.114	26.049	30.977	27.148

Table 5.4: Detailed simulation results for aluminum rotor bar (continuation of previous table).

Harmonic Order		1,7,11,13		1,5,11,13		1,7,11		1,5,13	
Current Denstiy ($A \backslash mm^2$)		Max.	Min.	Max.	Min.	Max.	Min.	Max.	Min.
Cross-section	Round	28.144	26.186	31.173	27.530	27.754	26.030	31.695	27.735
	Square	28.007	25.998	31.247	27.451	27.585	25.821	31.827	27.696
	Deep bar	30.506	24.218	34.532	25.597	29.987	24.040	35.232	29.857
	Two-way bar	28.857	25.963	32.190	27.688	28.547	25.729	32.759	27.909

6. CONCLUSIONS AND RECOMMENDATIONS

In this thesis, deep bar effect in squirrel-cage induction motor was investigated. Motivation point was to obtain space harmonic effect on deep bar effect. A real motor data was used for reliable results. Four different rotor bar cross-sections that are round, square, deep bar, and a novel two-way rotor bar were investigated. Simulations repeated for two different materials that are copper and aluminum. During the study it was realized that there was a relation between harmonic order and rotor bar geometry. A new model was developed to investigate this relation.

Under some certain assumptions, satisfactory and useful results were achieved. These results are itemized and given below.

- Simulation results demonstrated that deep bar effect depends on space harmonic order. It was seen that 5th and 13th order harmonics were increasing the deep bar effect whereas 7th and 11th order harmonics were decreasing the deep bar effect. The simulation results for copper rotor bar in Appendix A.1 and A.2 and Table 5.1 and 5.2 can be seen to discuss these results. It was assumed that the total current contains 1st, 5th, 7th, 11th, and 13th since other harmonic orders amplitudes were low enough to neglect. First the 5th harmonic was eliminated. The related simulation result depicted that the current density values decreased and current density distribution normalized. Then $7th$ harmonic was eliminated. This time current density values reached higher numbers and bar current accumulated near the top of the bar. This effect was not dependent to bar geometry. All of the bar types reacted in the same manner.

  This effect can be explained by using the harmonic components current directions for a certain instant. In this study $5ms$ instant was analyzed. At this instant 1st, 5th, and 13th harmonic currents are in the same direction. However, 7th and 11th harmonic currents flow in the opposite direction. As a result 7th and 11th harmonics attenuate deep bar effect and makes the current the current distribution smoother. On the contrary, 5th and 13th harmonics step up the deep bar effect. This result

can be generalized as if the harmonic component is in the same direction with fundamental component at the instant 5*ms*, that harmonic increases the deep bar effect but if it is in the opposite direction with fundamental component at the instant 5*ms*, that harmonic decreases the deep bar effect.

As a result, if an induction motor would have been designed to use the deep bar effect as an advantage, 7th and 11th harmonics should be eliminated and if an induction motor would have been designed to decrease copper losses, then 5th and 13th harmonics should be eliminated by using different winding techniques in the stator windings of the motor.

- Magnetic conductance factors and leakage flux values were calculated in Chapter 4. According to those results round rotor bar's leakage flux was two times higher than square rotor bar's leakage flux. One can say that induced eddy currents should be less in the square conductor. However, in the simulation results the current density distribution of the round and square rotor bars were very close. Moreover, in the square rotor bar the rotor current moved to upper corners of the bar that means square rotor bar could be a more lossy form. It is not certain because power loss calculations were not included in this thesis because of the assumptions. Nevertheless, this result propounded that rotor bar geometry was an important design criteria. By using different cross-sections, space harmonic effects can be increased or decreased.

- A novel rotor bar geometry was investigated in this thesis which was called as two-way rotor bar. This rotor bar type had the same depth with the deep bar type. But the width of the bar was not uniform. The bar actually consisted of a square part and a rectangular part. According to calculations in Chapter 4 the leakage flux value was 2.5 times higher than deep bar. The expected result was deep bar effect would be much more higher in this bar type. However, due to shape of the two-way rotor bar deep bar effect decreased. Because, the width of the bar was narrower at top and wider at the bottom. As a result magnetic flux density increased at the top of the bar and induced more eddy currents at that part.

According to magnetic analysis results, there were some differences with analytical expected results. Deep bar effect in two-way bar type was higher than the round

and square cross-sections but it was less than deep rotor bar. The current density distribution in this rotor type was also different from the others. The current density distribution of the square part was very close to DC current form and deep bar effect was not observed at this part. In the rectangular part of the rotor bar the current density distribution was similar to deep rotor bar but with one difference. The difference was that deep bar effect decreased in two-way rotor bar. This result was investigated deeper and another significant result was obtained.

- Since the deep bar effect decreased in two-way rotor bar it was thought that 7th harmonic component was increased in this bar type. Because, as it was mentioned above 7th harmonic had a decreasing effect on deep bar effect. A different simulation model was developed and the 7th harmonic effect was obtained. Results are given in Appendix A.3. According to simulation results, two-way rotor bar induced 3 times higher eddy currents than round and square rotor bars. The maximum current density values at the top of the two way rotor bar and deep rotor bar were similar. However, current density distribution resulted in more different in the two-way rotor bar which showed that current density distribution was not balanced in this rotor bar type. As a result, it was discovered that two-way rotor bar type reacted 7th harmonic much more than any other analyzed bar type in this study.

The reason of this result can be explained by using the basics of skin effect and deep bar effect. Skin effect is increased by the current frequency. 7th space harmonic's frequency is 7 times higher than fundamental frequency. That means more eddy currents will be induced for this component. It is also known that deep bar effect is created by an external magnetic field actually and it is due to leakage flux in the rotor bar in this case. Harmonic effects can not be considered and investigated individually. First component of the rotor bar current always consists in the machine and it creates the deep rotor bar effect actually. In the light of this information it can be easily deduced that 7th harmonic induces much more eddy currents in the rotor bar. Now, the effect of geometry can be explained. The cross-section area was lower at the top of the bar. This will increase magnetic flux density at that part and induced currents accumulates at that part of the conductor. 7th harmonic effect is higher rather than 5th harmonic effect due to frequency. 5th harmonic component's

frequency is lower than 7th harmonic. As a result 5th harmonic component does not gather at the top of the rotor bar as much as 7th harmonic. Hence, 7th harmonic effect is more penetrating in two-way rotor bar.

It should be also pointed out that the results mentioned above and 7th harmonic effect were consistent. All results indicated that 7th harmonic component had a decreasing impact on deep bar effect. Moreover, this result was another proof of that design of rotor bar geometry could be used to increase or decrease space harmonic effects in the machine.

- In this study, two different material was investigated. The first one was copper and the second one was aluminum. These two material were chosen because these materials are used in many motor applications. It was seen that using aluminum instead of copper decreased deep bar effect. Related simulation results are given in Appendix A.2 and Table 5.3-5.4. The current density values in aluminum rotor bars were less than copper rotor bars, which was an expected result. The current density distribution was also more balanced. The current density distribution was not uniform but had a better distribution in the conductor compared to copper rotor bars. This result was also an expected result, because the skin depth of aluminum at 50 Hz is approximately 11.546 mm whereas 9.345 mm for copper. Thus, the skin effect is lower in aluminum conductor and also deep bar effect will be less in the aluminum rotor bars. Simulation results supported the effect explained above. According to simulation results deep bar effect decreased but to determine which material is beneficial further analysis required. Because conductivity of the aluminum is less than copper. Hence, less rotor bar currents are induced in rotor bar and induced torque value and power losses change in the motor. To make the material distinction, a complete design of an induction motor is required and this is a future work about this thesis.

- There are some significant points while investigating the deep bar effect in the motor. As it was mentioned above the effects of harmonics should not be analyzed separately. The most significant point for deep bar effect is applied magnetic field to the conductor. If one tries to obtain 5th,7th or any other harmonic component individually, receives misleading and wrong results. Because, the harmonic components except the fundamental component create too weak magnetic fields

and these created magnetic fields are not enough to induce eddy currents in the conductor. Thus, the results would be similar to an analysis of skin effect in a bare conductor which is a wrong result. To overcome this problem, the fundamental component of the magnetic field that created by leakage rotor flux should be applied to the rotor bar. This process was used to investigate 7th harmonic effect during the study.

- The skin effect does not depends on amplitude of the current. Skin effect and deep rotor bar effect are quite similar and skin effect creates the basics of the deep rotor bar effect. However, there is a distinction point between them which magnetic field density. If the magnetic field density that applied to the rotor bar is higher then deep bar effect is higher and vice-versa. The mentioned magnetic field density is created by the leakage flux in the rotor in the induction motor. The calculated rotor bar currents were for $3 \, kW$ motor in this thesis. If a more powerful motor is going to be investigated, then rotor bar currents at the start-up can get excessive values that creates very high leakage magnetic field density values. In this case deep bar effect is multiplied by the rotor bar current. Thus, design of the rotor bar and harmonic effects can be fatal for high power motors. It should be always kept in mind that skin effect effect and deep bar effect are similar effects but deep bar effect is influenced significantly by related current values even if it is an indirect effect.

As a conclusion, space harmonics have a significant impact on deep bar effect. All simulation results support this hypothesis. This thesis propounds that 7th, 11th and every other current harmonic components that in the opposite direction with fundamental component decreases the deep bar effect and 5th, 13th and every other current harmonic components that in the same direction with fundamental component increases the deep bar effect. The rotor bar geometry effects the induced harmonic current components in the rotor bar. There is a relation between two-way rotor bar geometry and 7th harmonic. All of these results are assertive for future works. In this thesis, rotor bar currents were assumed as constant for simulations to make comparisons. As a future work, a complete design can be done for each type of rotor bar and material. According to those results a decision can be made about which material and which rotor bar type is beneficial for motor manufacturing. Another future work can be done for harmonic elimination in the motor. Different winding

techniques can be used to eliminate desired harmonic components in the stator winding function and as a result harmonic components induced in the rotor. This effect can be supported by designing different rotor bar geometries and total machine harmonics can be optimized and also the efficiency of the motor can be increased. The study achieved its objective and this study will lead to future works mentioned above.

REFERENCES

[1] **Dwight, H.B.**, 1922. Skin effect and proximity effect in tubular conductors, *Transactions of the American Institute of Electrical Engineers*, **XLI**, 189 – 198.

[2] **Dwight, H.B.**, 1929. Bessel functions for A-C. problems, *Transactions of the American Institute of Electrical Engineers*, **48(3)**, 812 – 820.

[3] **Wheeler, H.A.**, 1942. Formulas for the skin effect, *RFIC Virtual Journal*, **30(9)**, 412 – 424.

[4] **Douglas, J.F.H.**, 1951. A Contribution to the Theory of the Deep-Bar Induction Motor, *Transactions of the American Institute of Electrical Engineers*, **70(1)**, 862–866.

[5] **Liwschitz-Garik, M.**, 1954. Skin-effect bars of squirrel-cage rotors, *Electrical Engineering*, **73(6)**, 504.

[6] **Cermak, I.A. and Silvester, P.P.**, 1968. Solution of 2-dimensional field problems by boundary relaxation, *Proceedings of the Institution of Electrical Engineers*, **115(9)**, 1341 – 1348.

[7] **Silvester, P.P. and Chari, M.V.K.**, 1970. Finite element solution of saturable magnetic field problems, *IEEE Transactions on Power Apparatus and Systems*, **PAS-89(7)**, 1642 – 1651.

[8] **Silvester, P.P. and Ferrari, R.L.**, 1996. Finite Elements for Electrical Engineers, Cambridge University Press, Cambridge, 3rd edition.

[9] **Reatti, A. and Kazimierczuk, M.K.**, 2002. Comparison of various methods for calculating the AC resistance of inductors, *IEEE Transactions on Magnetics*, **38(3)**, 1512 – 1518.

[10] **Gerling, D.**, 2009. International Conference on Electrical Machines and Systems ICEMS 2009, Approximate analytical calculation of the skin effect in rectangular wires, Tokyo,Japan.

[11] **Seman, S.**, **Saitz, J. and Arkkio, A.**, 2003. International Conference on Electrical Machines and Systems ICEMS 2003, Dynamic model of cage induction motor considering saturation and skin effect, Beijing,China.

[12] **Khang, H.V. and Arkkio, A.**, 2012. Parameter estimation for a deep-bar induction motor, *Electric Power Applications, IET*, **6(2)**, 133 – 142.

[13] **Kazimierczuk, M.K.**, 2009. High Frequency Magnetic Components, John Wiley and Sons Ltd., West Sussex, United Kingdom.

[14] **Boduroğlu, T.**, 1994. Elektrik Makinaları Dersleri Cilt II Kısım 2, Beta Basım Yayım Dağıtım A.Ş., İstanbul, 2. edition.

[15] **Mergen, A.F.**, 1977. Minimisation of inverter-fed induction motor losses by optimisation of PWM voltage waveform, Ph.D. thesis, Loughborough University of Technology, Loughborough, United Kingdom.

[16] **Boldea, I. and Tutelea, L.**, 2010. Electric Machines Steady state, transients and design with MATLAB, CRC Press, Boca Raton, FL, USA.

[17] **IEEE-112-2004**, 2004. IEEE Standard test procedure for polyphase induction motors and generators, *Institute of Electrical and Electronics Engineers*.

[18] **Fitzgerald, A.E., Charles Kingsley, J. and Umans, S.D.**, 2003. Electric Machines, Mac Graw Hill, New York, NY, USA, 6th edition.

[19] **Kocabas, D.A.**, 2009. Novel winding and core design for maximum reduction of harmonic magnetomotive force in AC motors, *IEEE Transactions on Magnetics*, **45(2)**, 735–746.

[20] **Kocabas, D.A. and Mergen, A.F.**, 2008. A novel method to reduce the effects of space harmonics alternating current machines, Industrial Electronics, 2008. ISIE 2008. IEEE International Symposium on, pp.692 – 697.

[21] **Boduroğlu, T.**, 1994. Elektrik Makinaları Dersleri Cilt II Kısım 3, Beta Basım Yayım Dağıtım A.Ş., İstanbul, 2. edition.

[22] **Url-1**, `http://www.rle.mit.edu/media/pr152/15_PR152.pdf`, retrieved on: 30.03.2014.

[23] **Nicola, B.**, 2005. Electrical Machine Analysis Using Finite Elements, CRC Press, Boca Raton, FL, USA.

APPENDICES

APPENDIX A.1 : Simulation Results for Copper Rotor Bar Profiles
APPENDIX A.2 : Simulation Results for Aluminum Rotor Bar Profiles
APPENDIX A.3 : Simulation Results for 7th Harmonic Effect

APPENDIX A.1
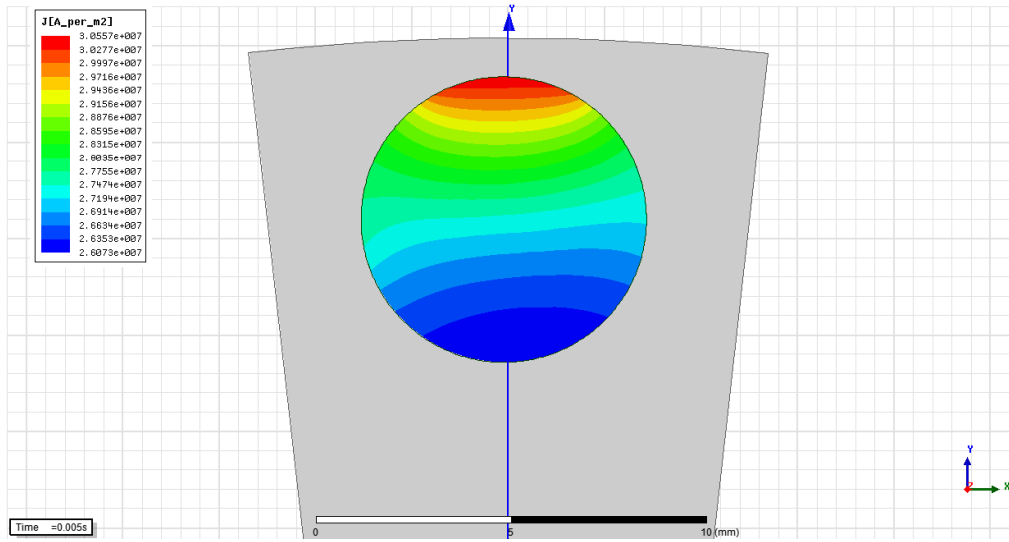
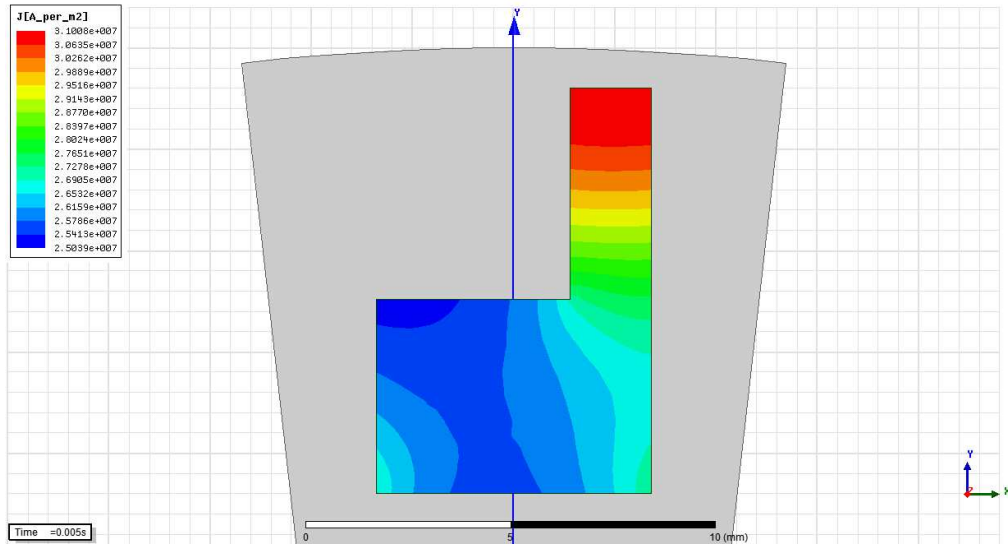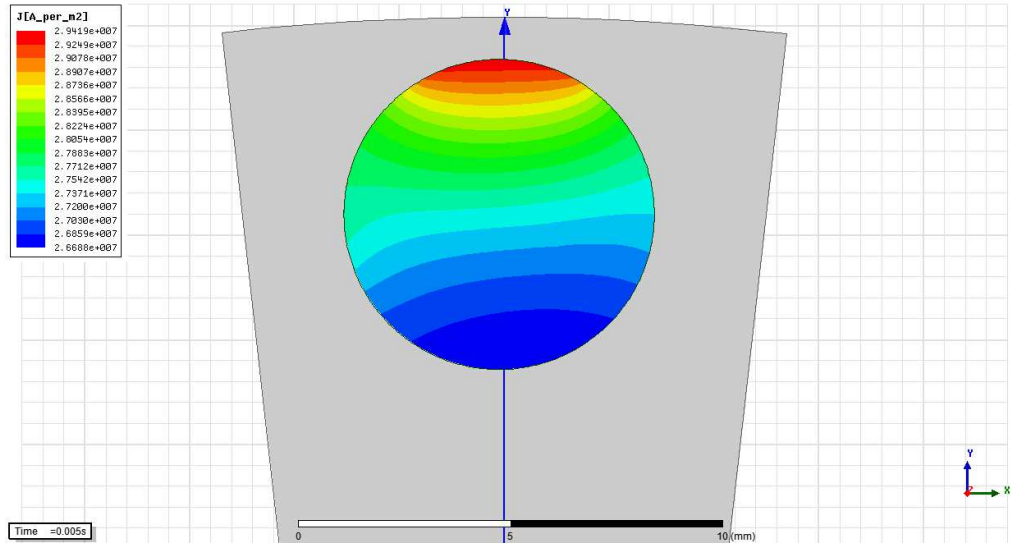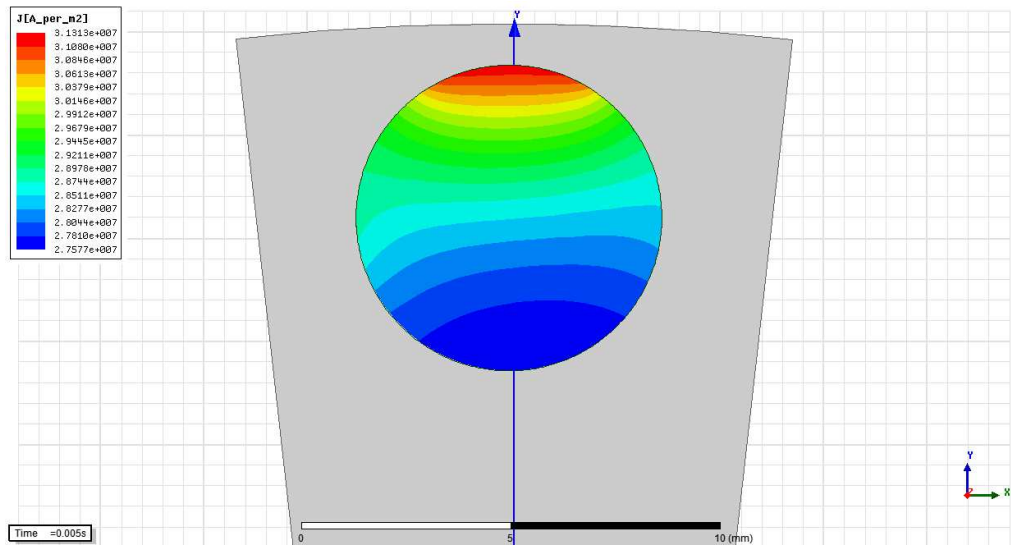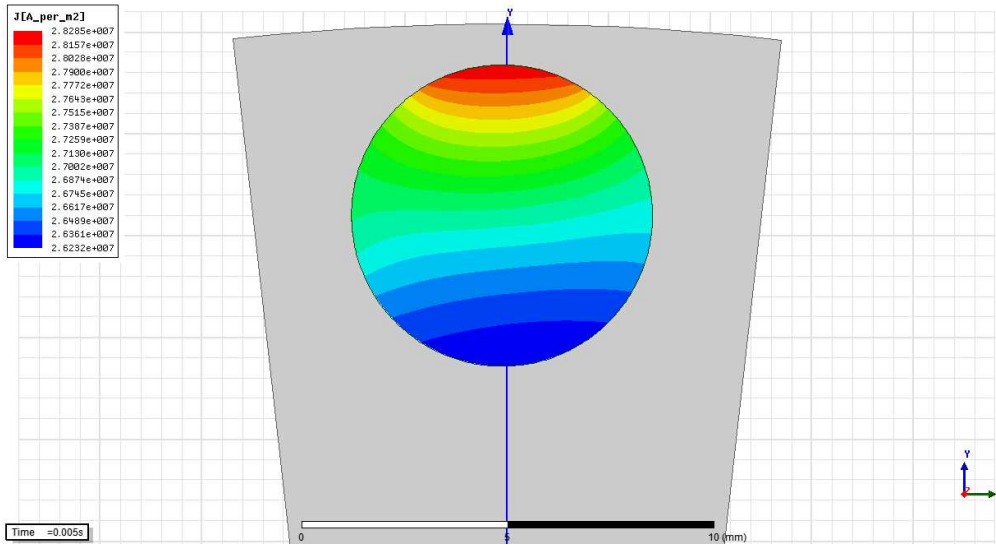**Figure A.1**: Current density distribution of round rotor bar for 1st harmonic
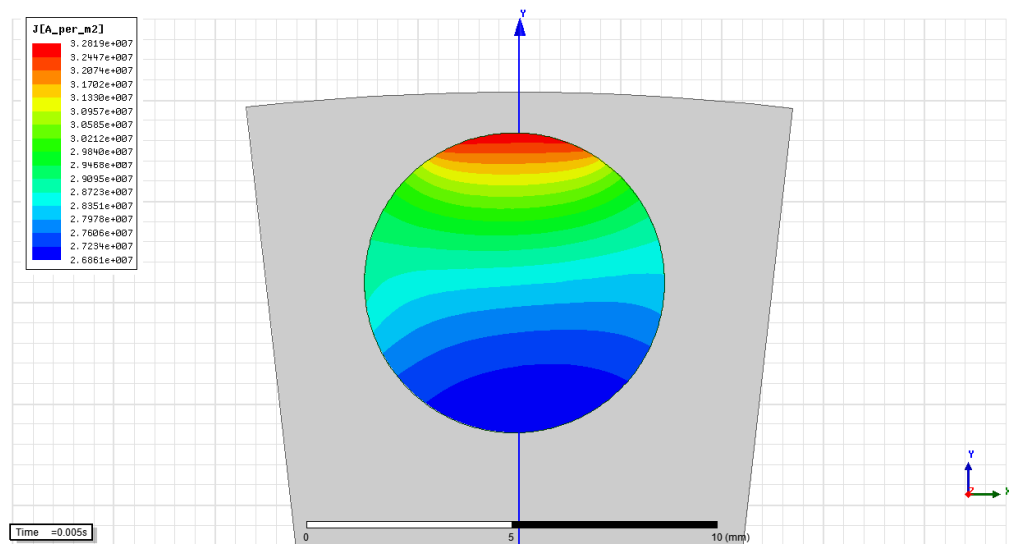
Figure A.2: Current density distribution of round rotor bar for 1st and 5th harmonics
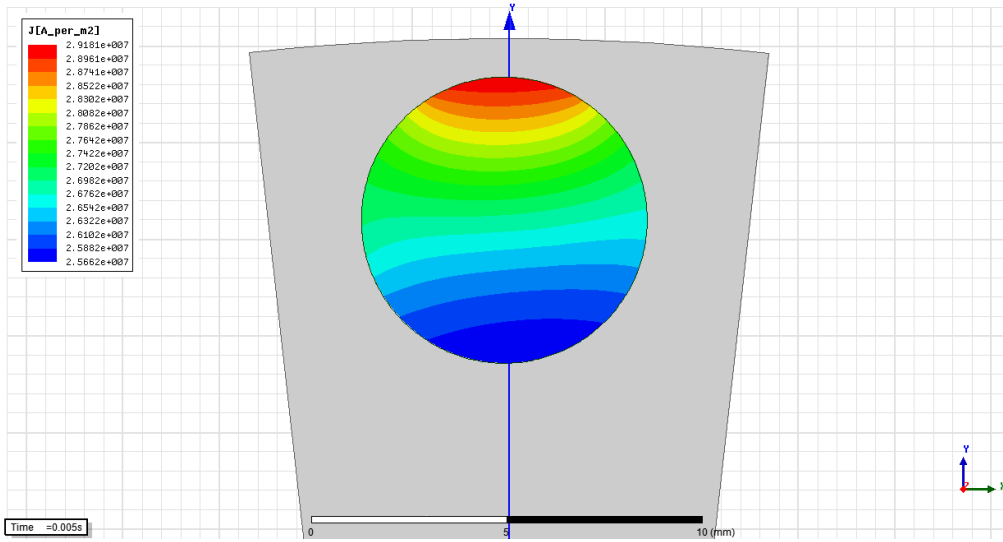
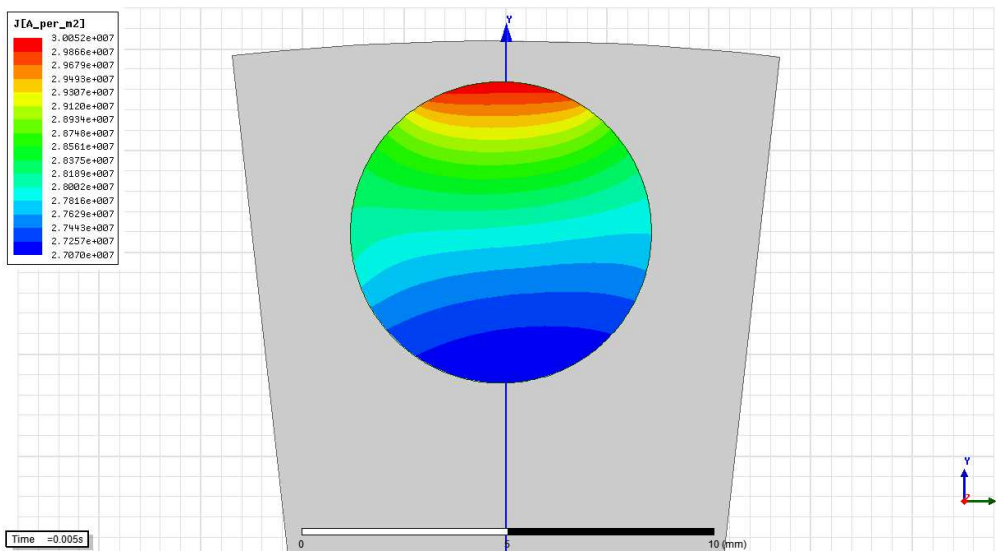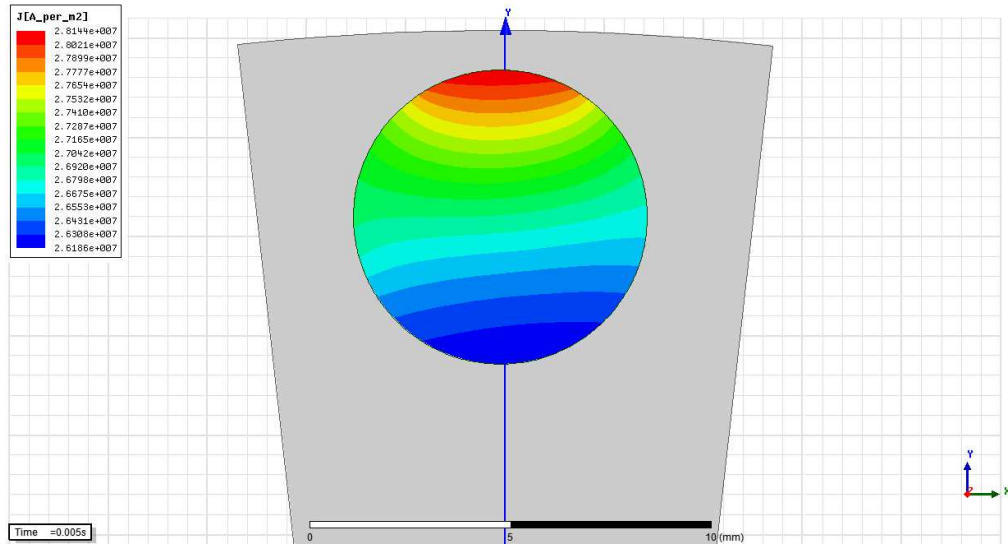**Figure A.3**: Current density distribution of round rotor bar for 1st and 7th harmonics
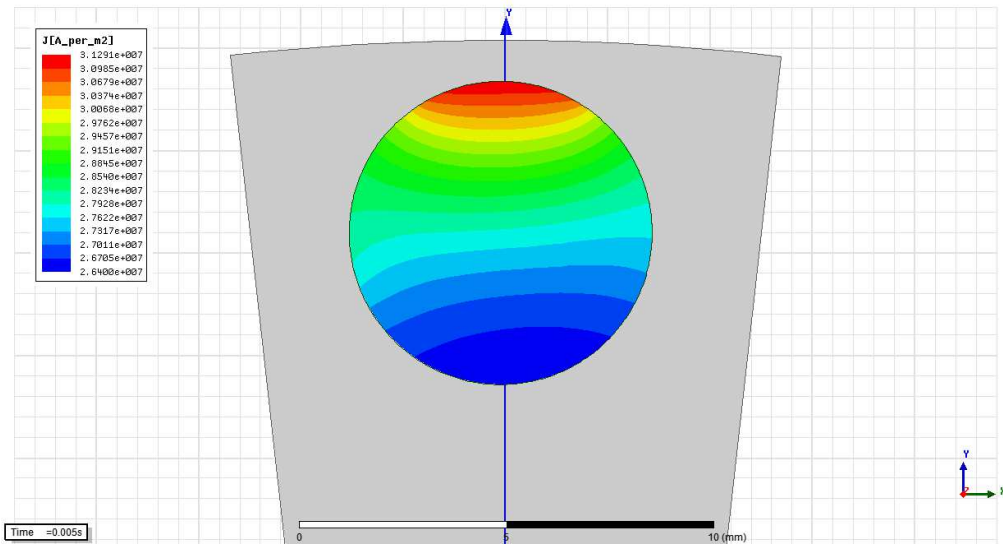
Figure A.4: Current density distribution of round rotor bar for 1st, 5th, 7th, 11th and 13th harmonics
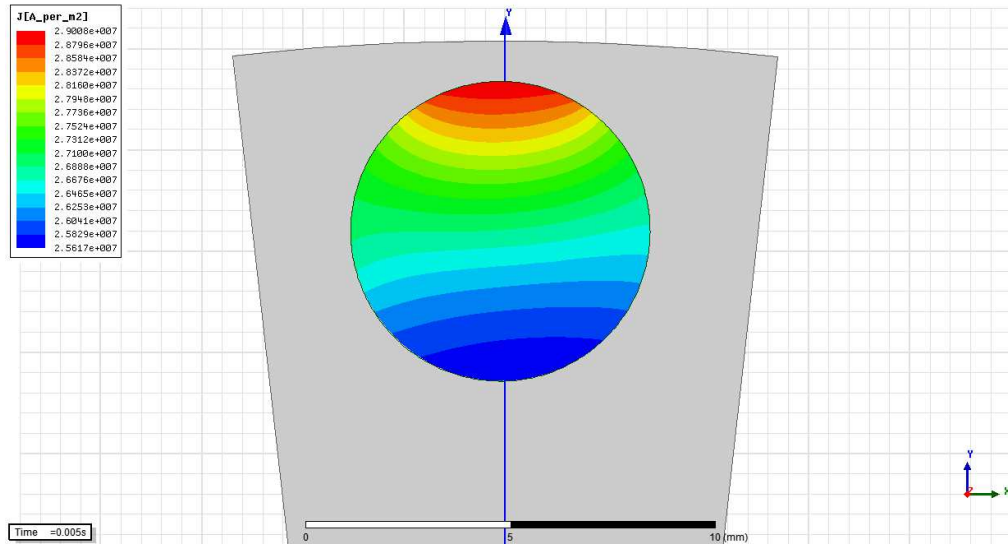
Figure A.5: Current density distribution of round rotor bar for $1^{st}, 7^{th}, 11^{th}$ and 13th harmonics
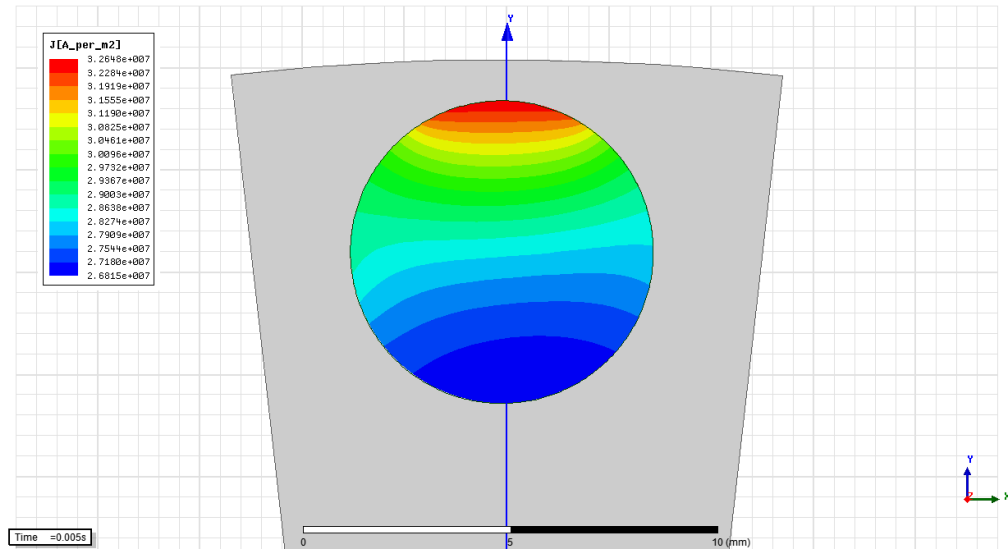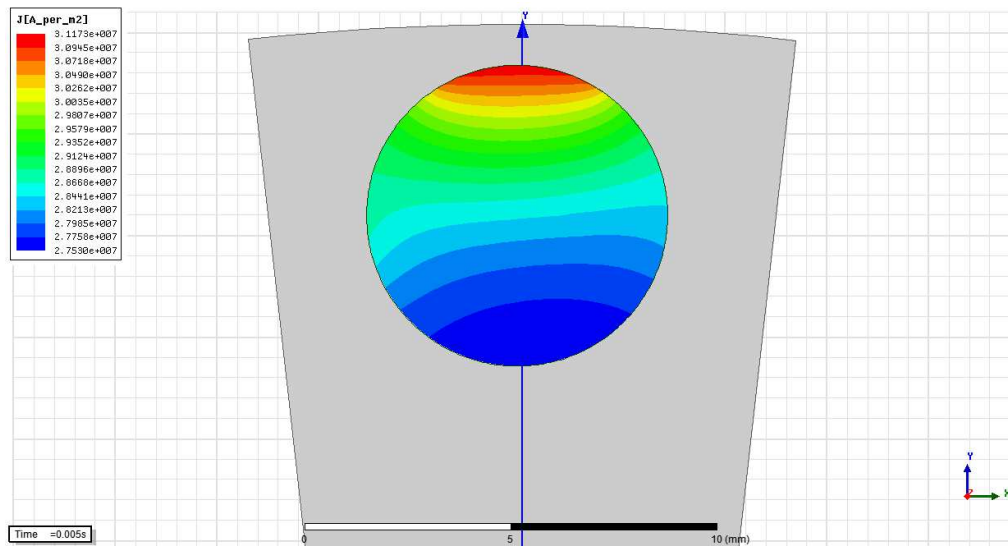

Figure A.6: Current density distribution of round rotor bar for $1^{st}, 5^{th}, 11^{th}$ and 13th harmonics
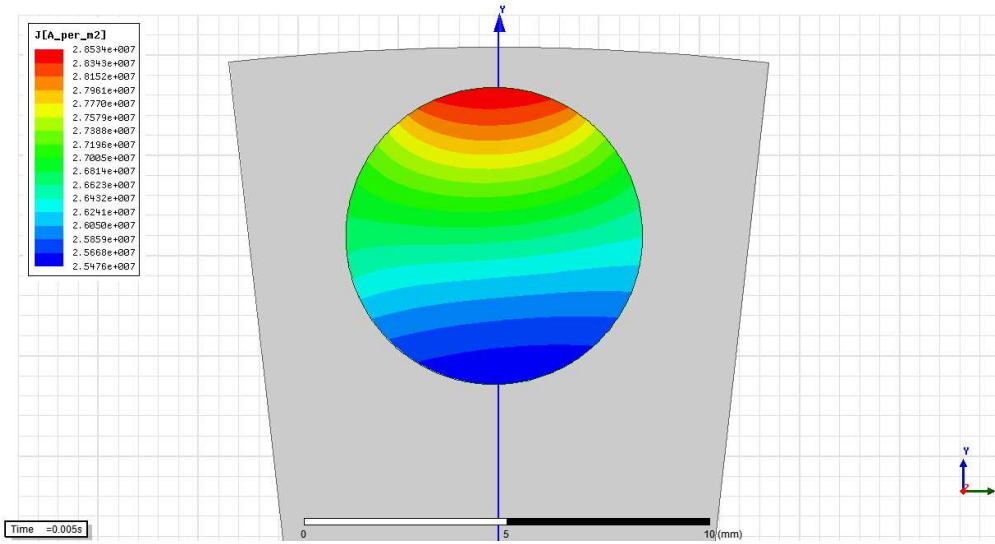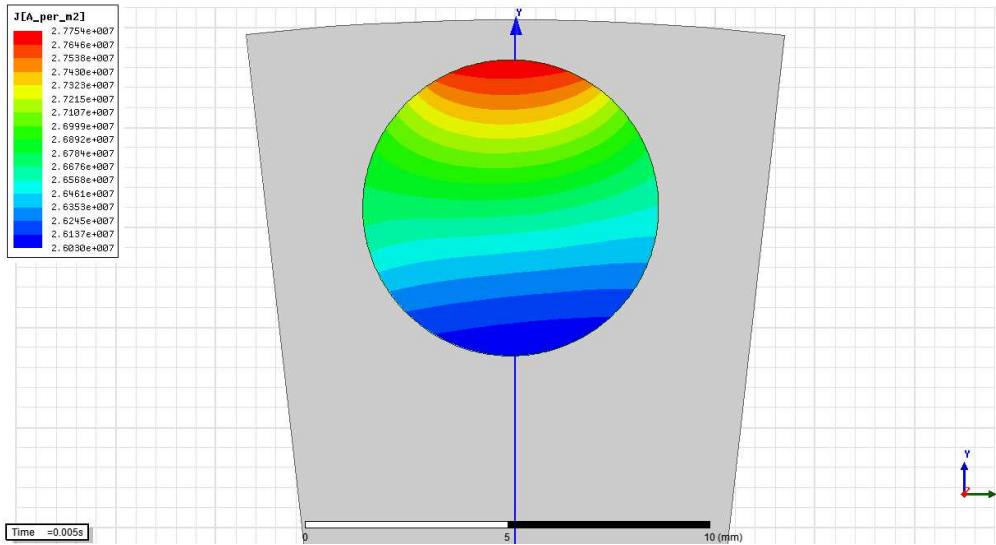
Figure A.7: Current density distribution of round rotor bar for $1^{st}, 7^{th}$ and 11th harmonics
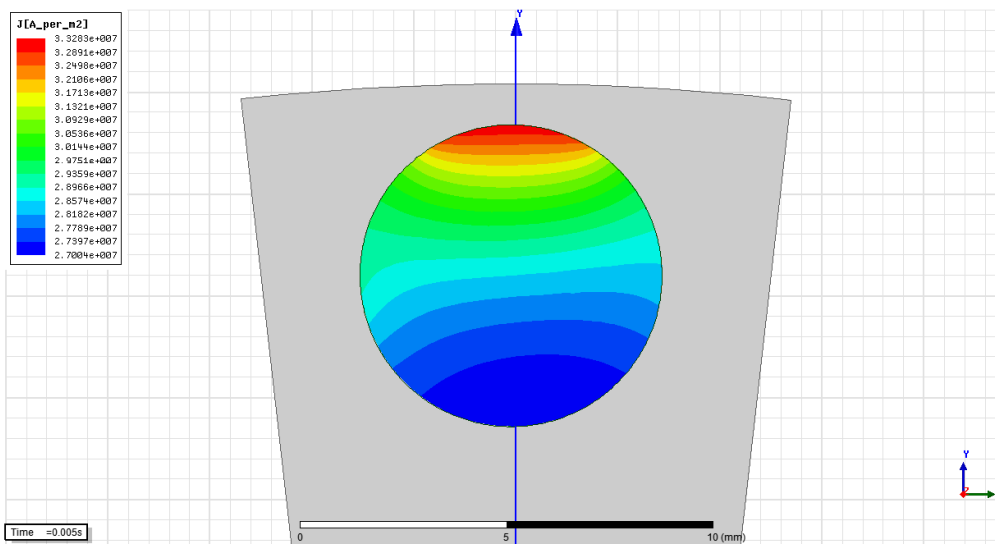
Figure A.8: Current density distribution of round rotor bar for $1^{st}, 5^{th}$ and 13th harmonics
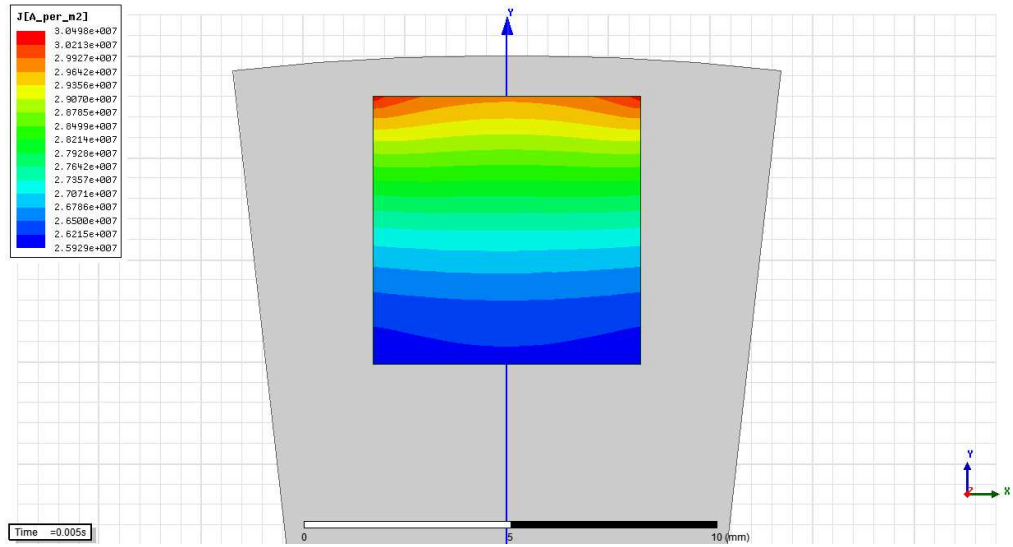
Figure A.9: Current density distribution of square rotor bar for 1st harmonic
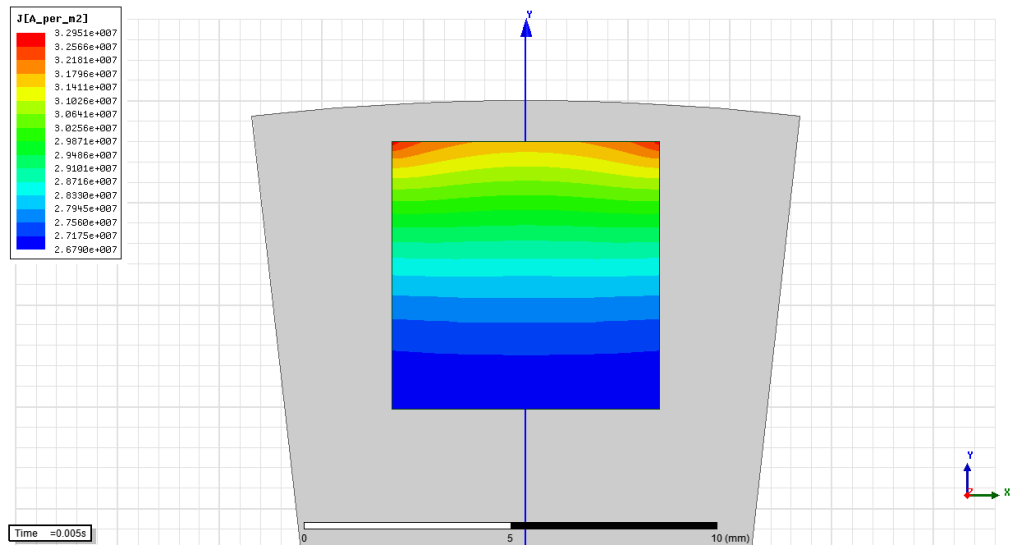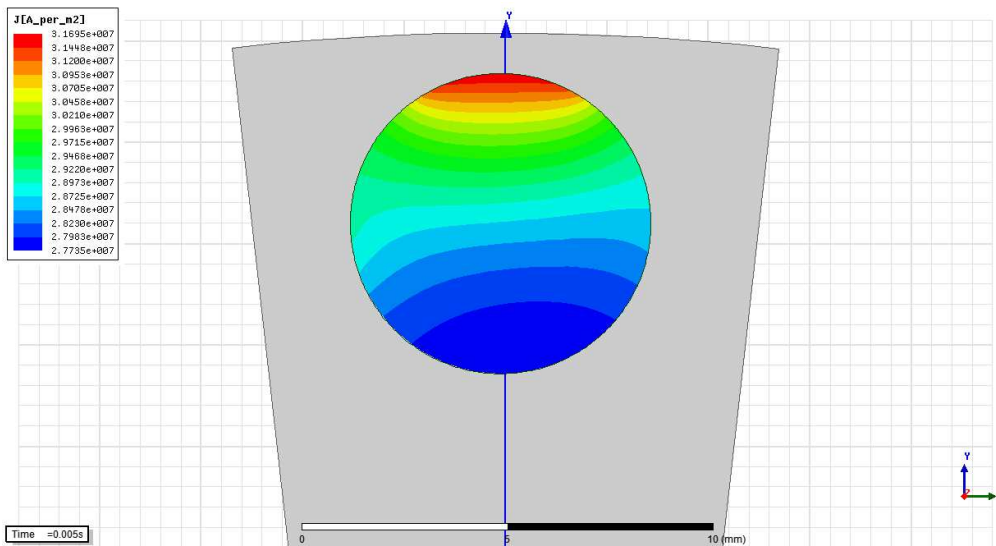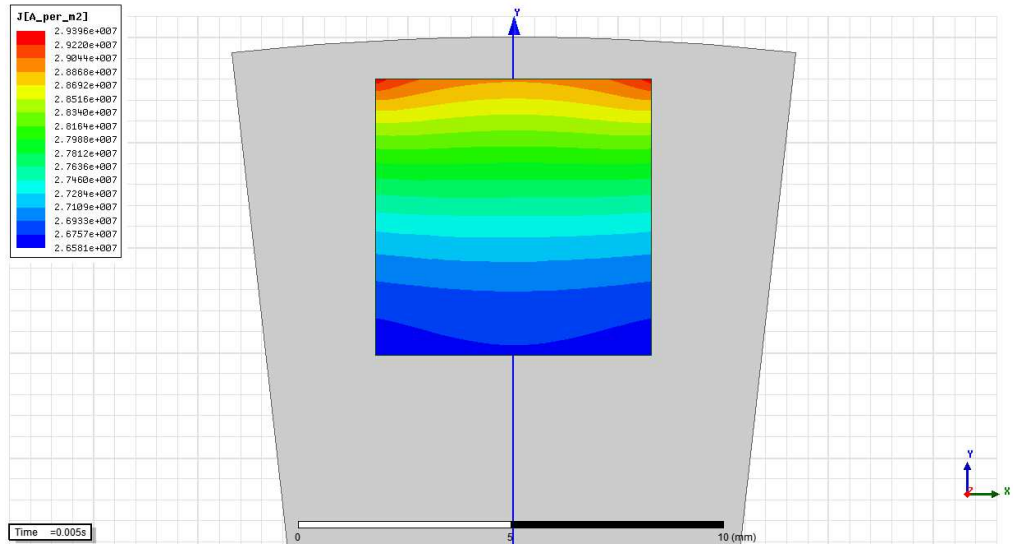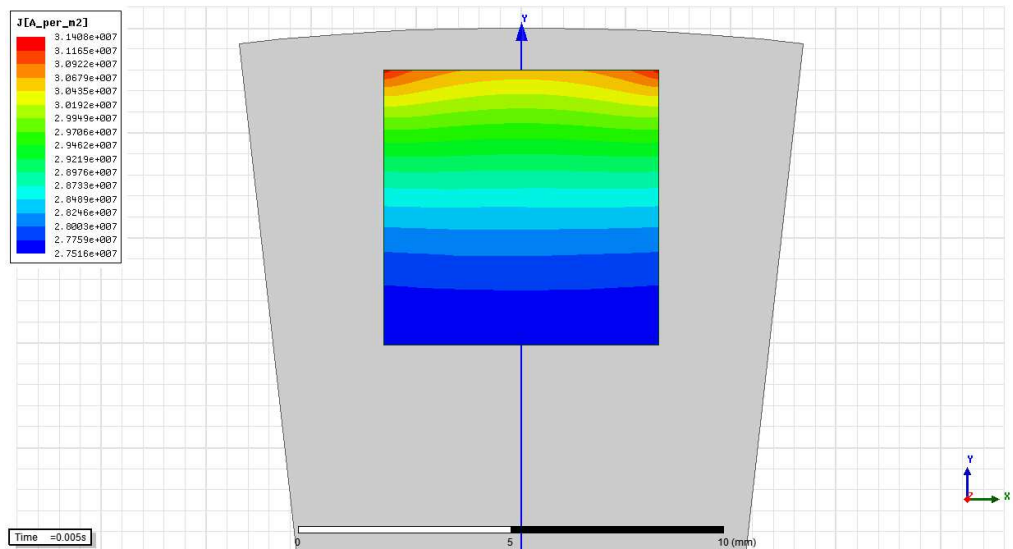

Figure A.10: Current density distribution of square rotor bar for 1st and 5th harmonics
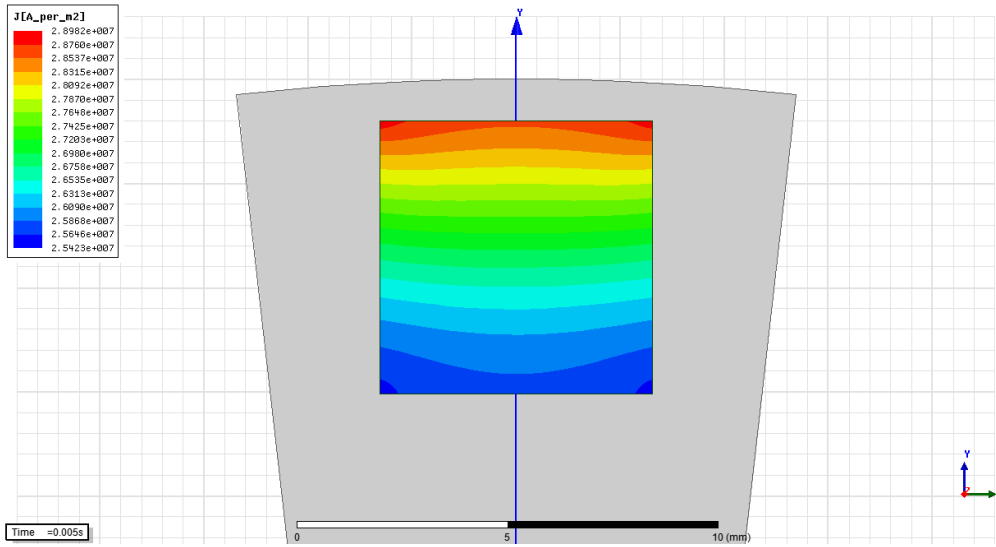
Figure A.11: Current density distribution of square rotor bar for 1st and 7th harmonics
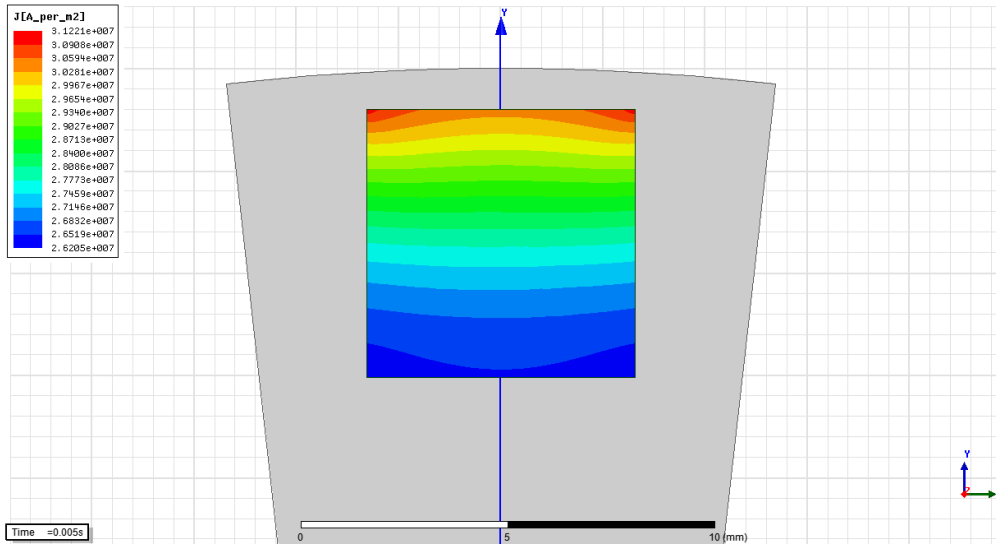
Figure A.12: Current density distribution of square rotor bar for 1st,5th,7th,11th and 13th harmonics
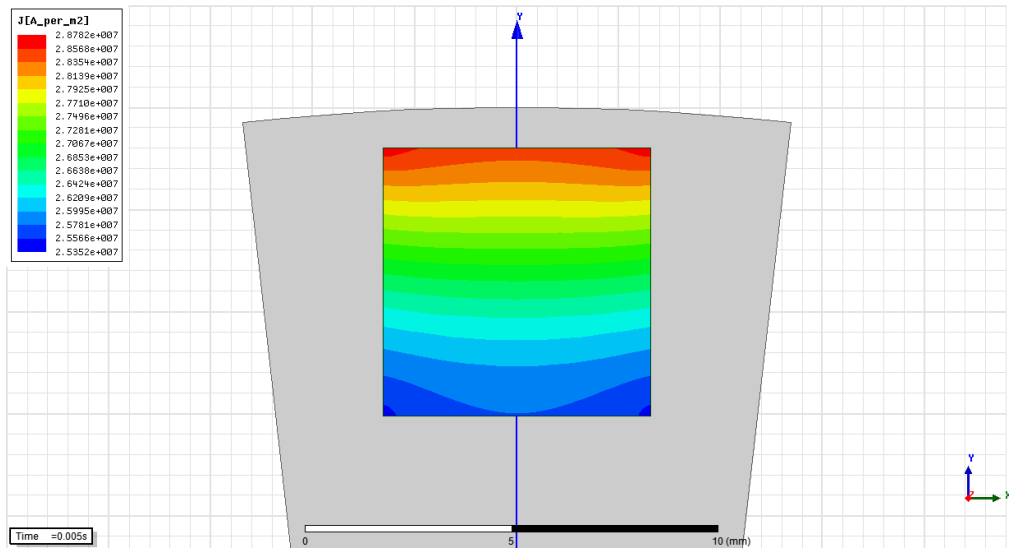
Figure A.13: Current density distribution of square rotor bar for 1st,7th,11th and 13th harmonics
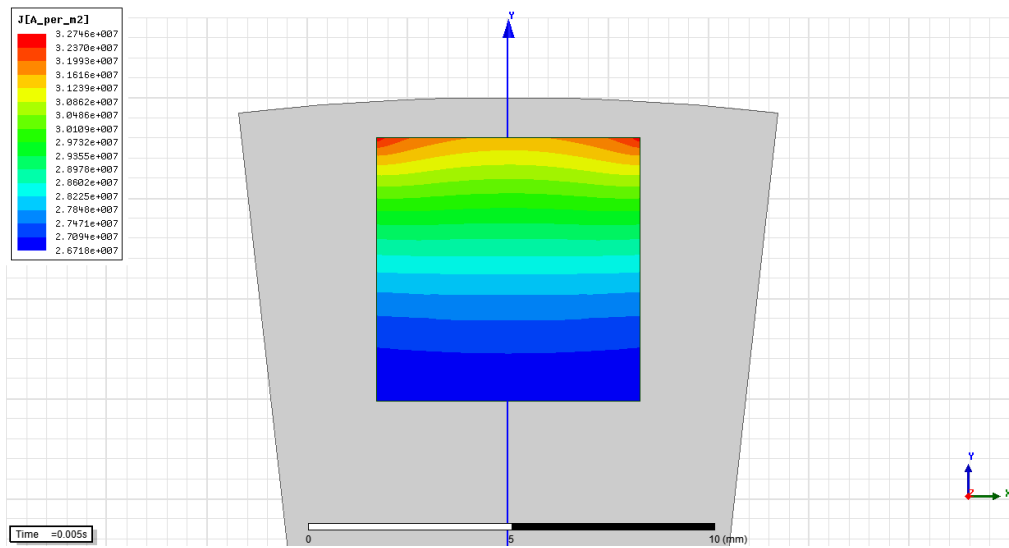
Figure A.14: Current density distribution of square rotor bar for 1st,5th,11th and 13th harmonics
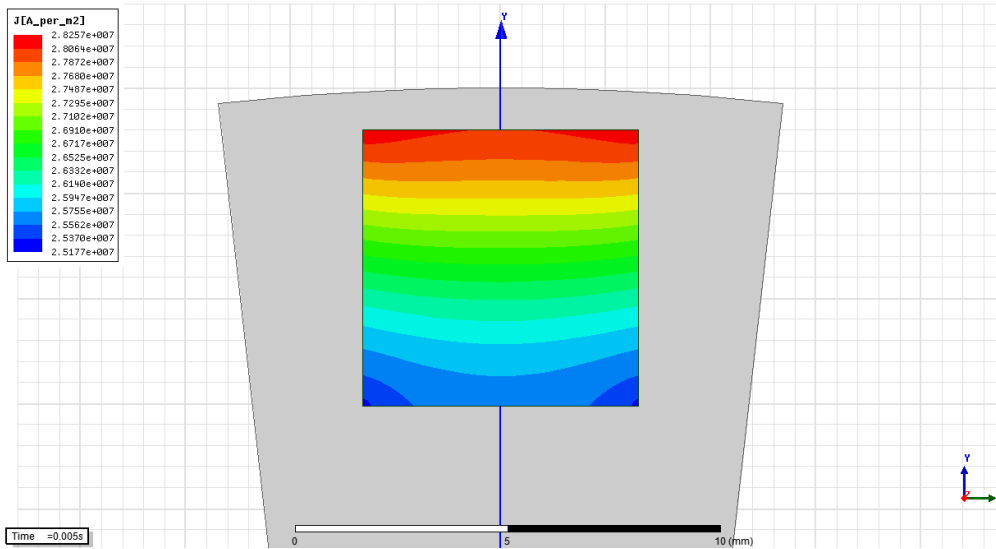
Figure A.15: Current density distribution of square rotor bar for $1^{st}, 7^{th}$ and 11th harmonics
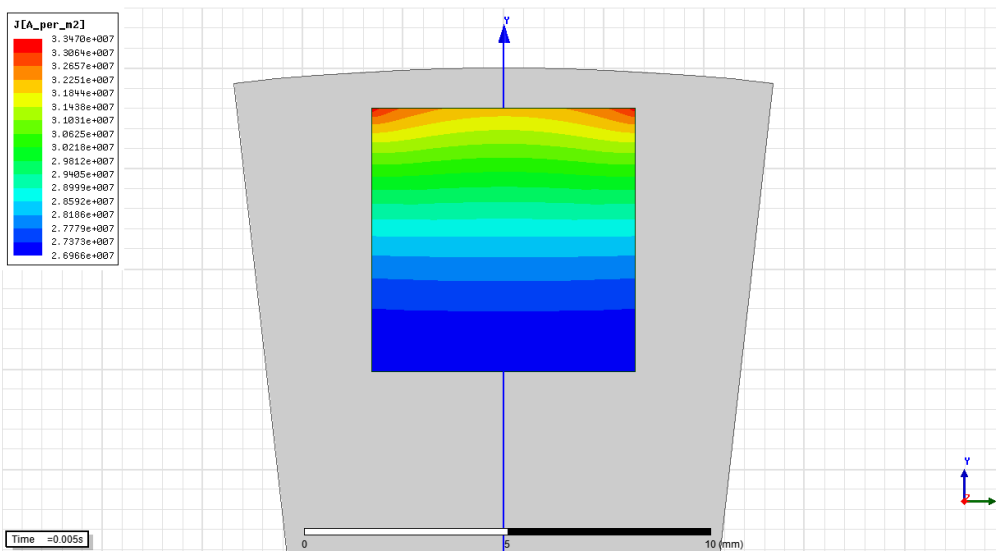
Figure A.16: Current density distribution of square rotor bar for $1^{st}, 5^{th}$ and 13th harmonics
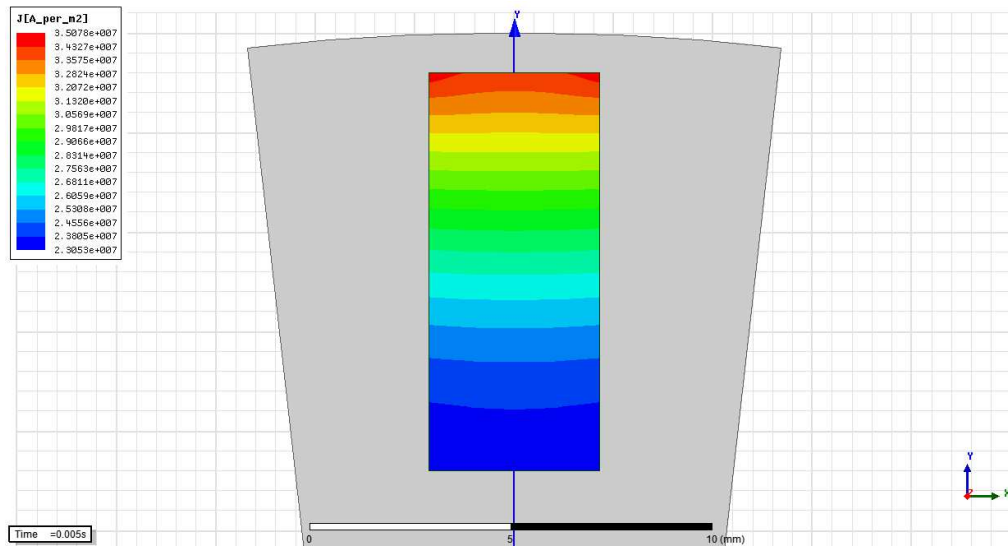
Figure A.17: Current density distribution of deep rotor bar for 1st harmonic
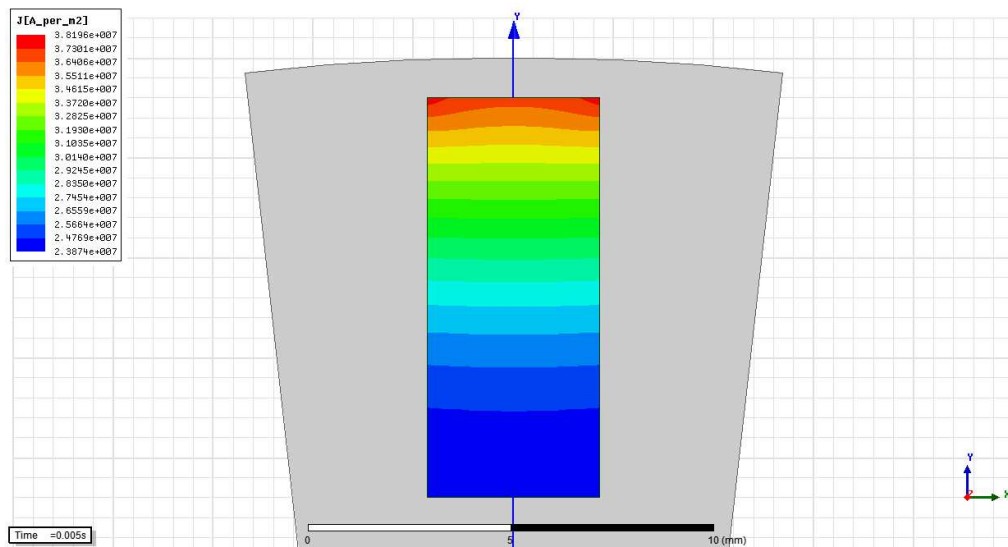
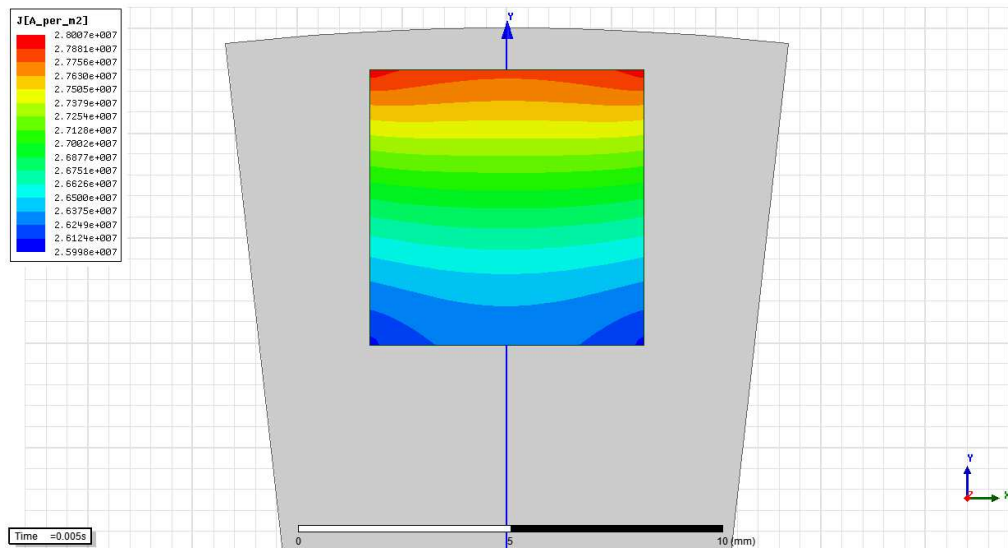**Figure A.18**: Current density distribution of deep rotor bar for 1st and 5th harmonics
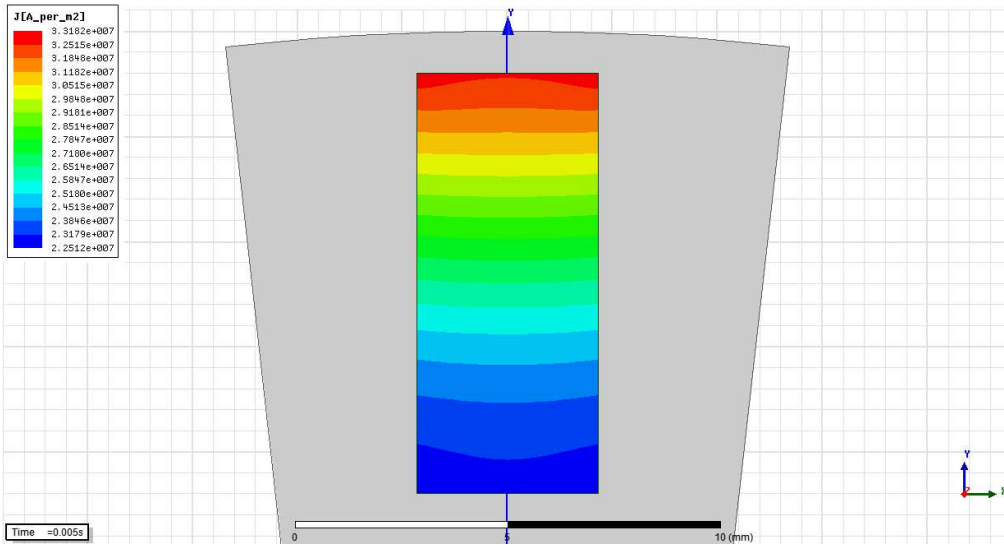
Figure A.19: Current density distribution of deep rotor bar for 1st and 7th harmonics
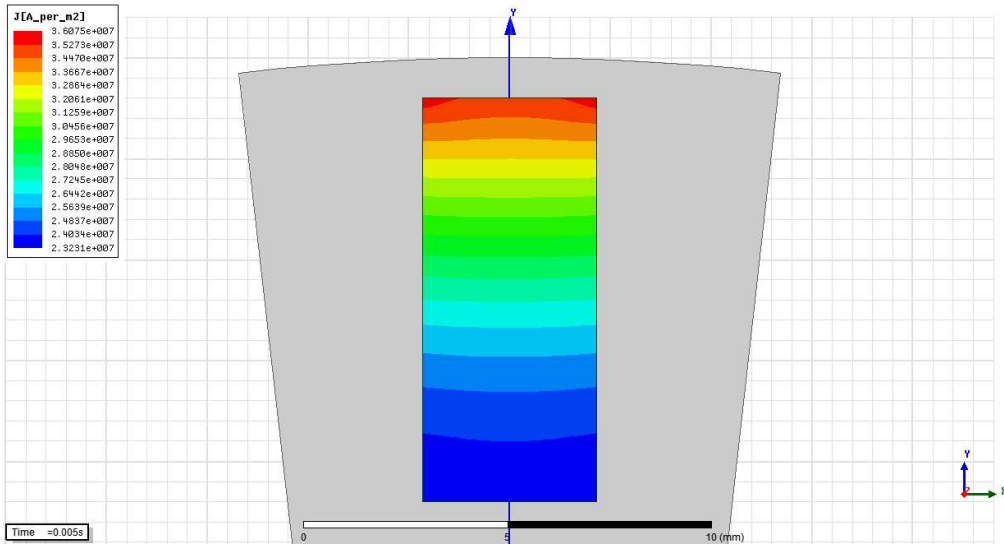
Figure A.20: Current density distribution of deep rotor bar for 1st,5th,7th,11th and 13th harmonics
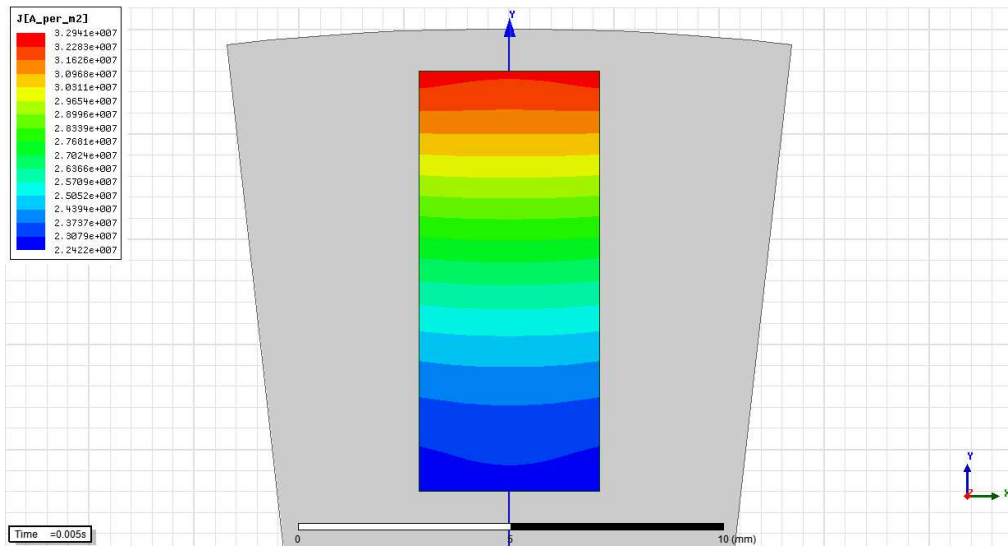
Figure A.21: Current density distribution of deep rotor bar for 1st,7th,11th and 13th harmonics
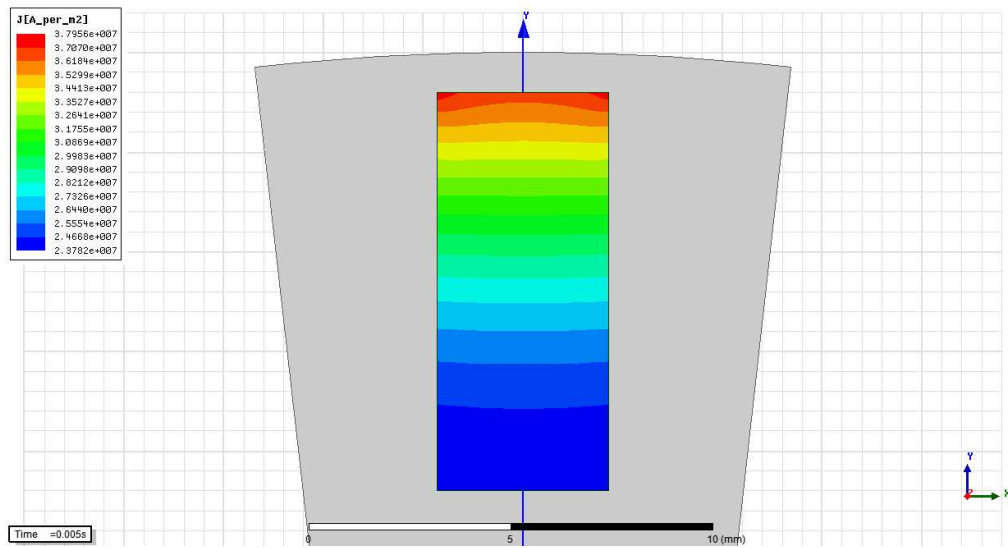
Figure A.22: Current density distribution of deep rotor bar for 1st,5th,11th and 13th harmonics
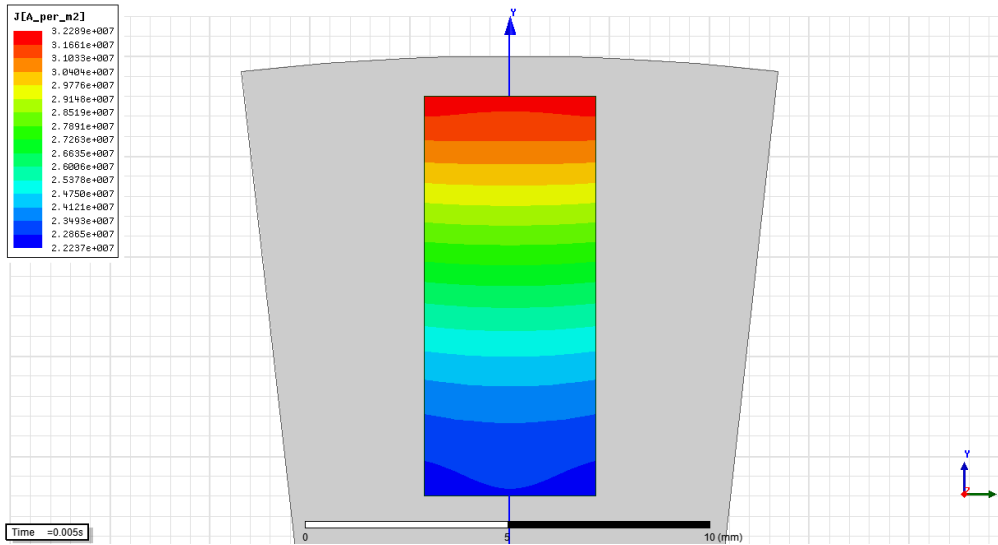
Figure A.23: Current density distribution of deep rotor bar for 1st, 7th and 11th harmonics
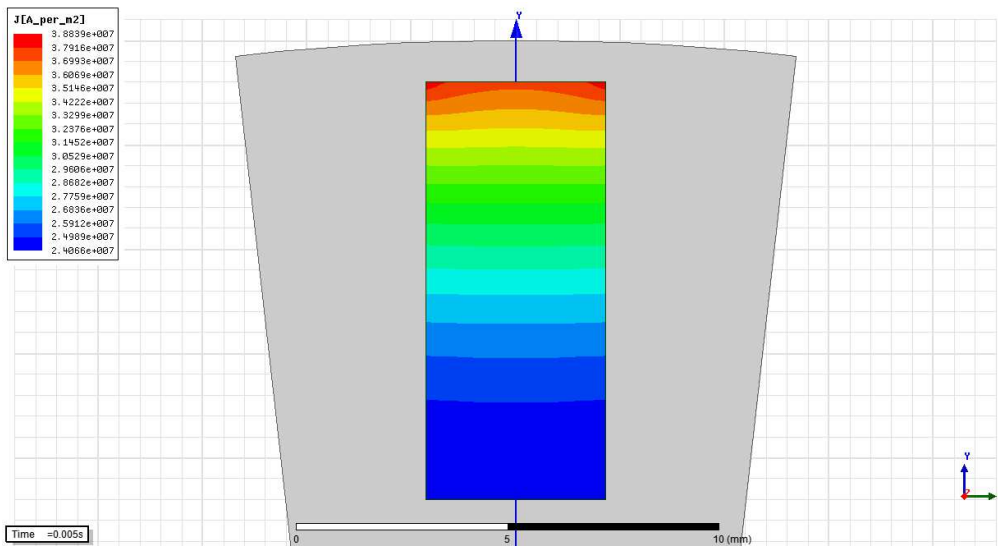
Figure A.24: Current density distribution of round rotor bar for 1st, 5th and 13th harmonics

62
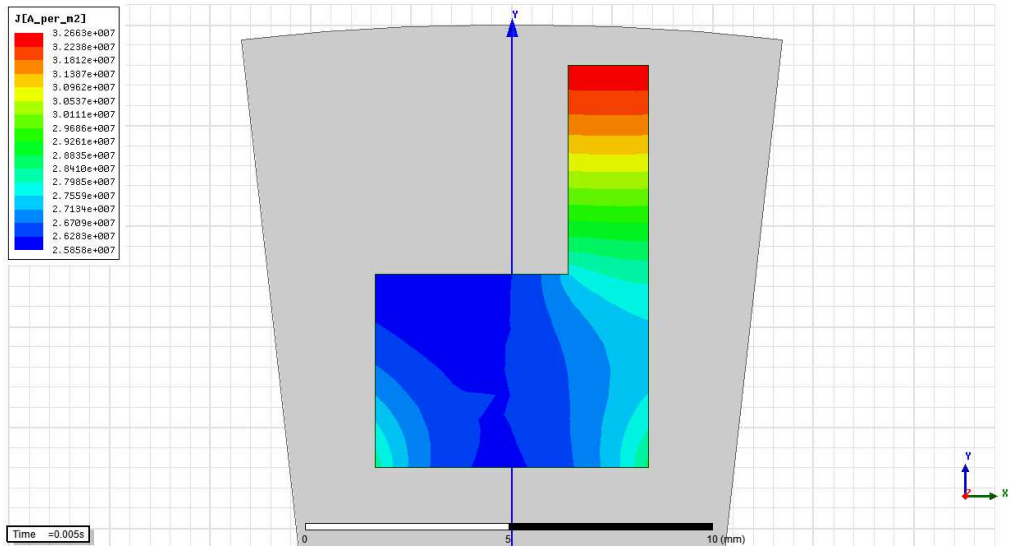
Figure A.25: Current density distribution of two-way rotor bar for 1st harmonic
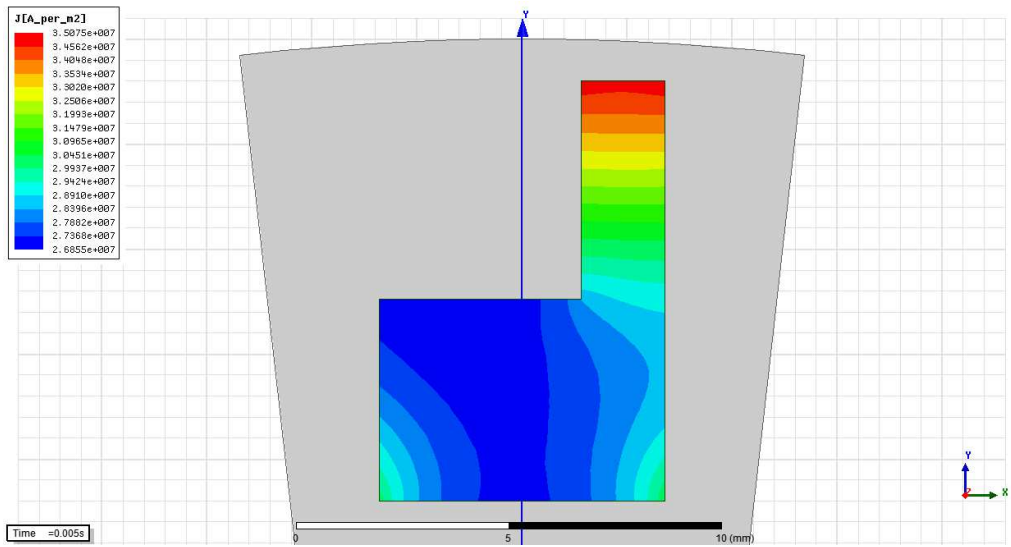
Figure A.26: Current density distribution of two-way rotor bar for 1st and 5th harmonics

63
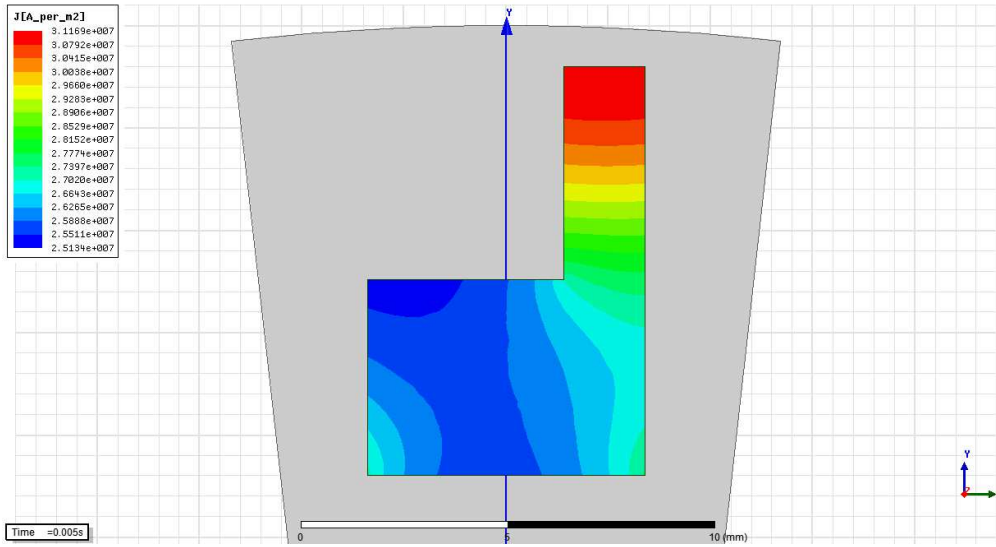
Figure A.27: Current density distribution of two-way rotor bar for 1st and 7th harmonics
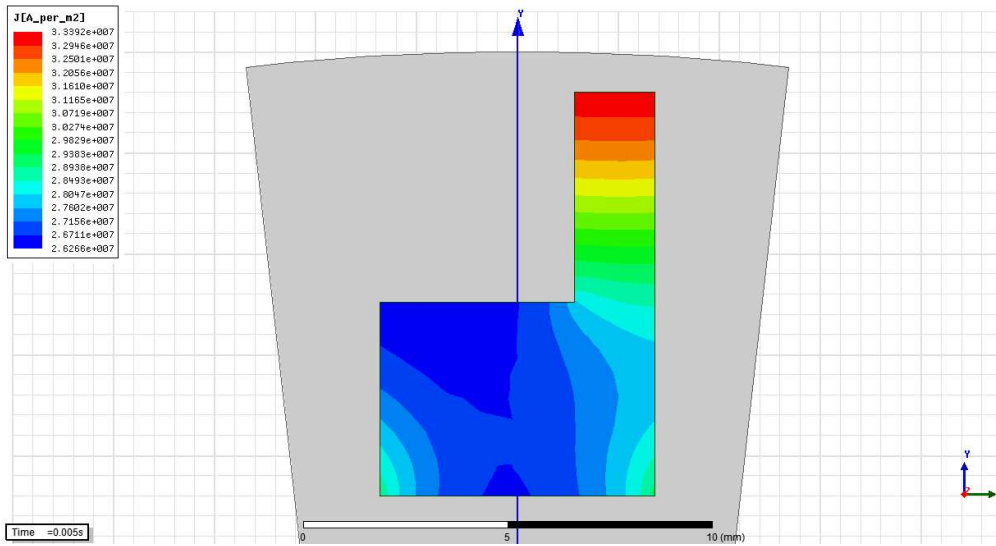
Figure A.28: Current density distribution of two-way rotor bar for 1st,5th,7th,11th and 13th harmonics

Figure A.29: Current density distribution of round two-way bar for 1st,7th,11th and 13th harmonics
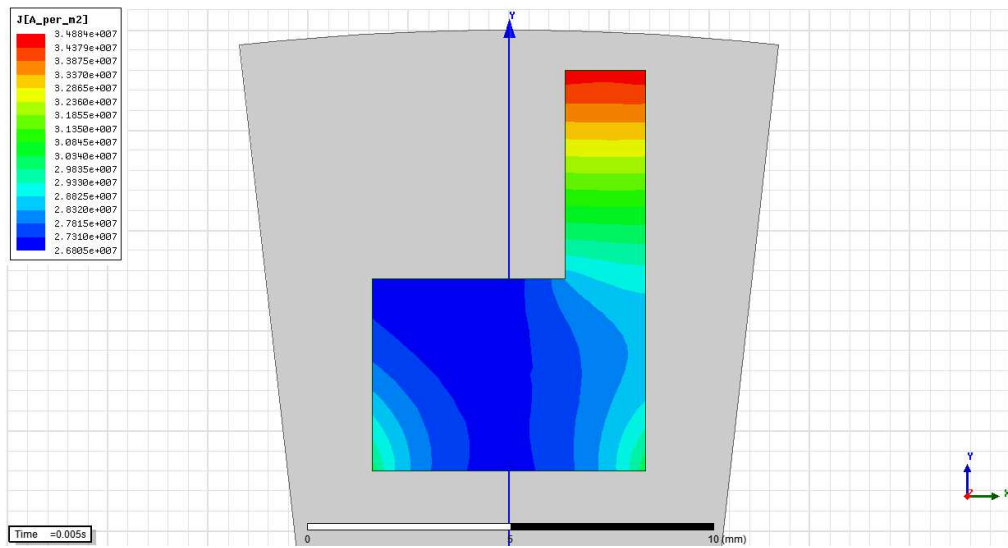
Figure A.30: Current density distribution of two-way rotor bar for 1st,5th,11th and 13th harmonics
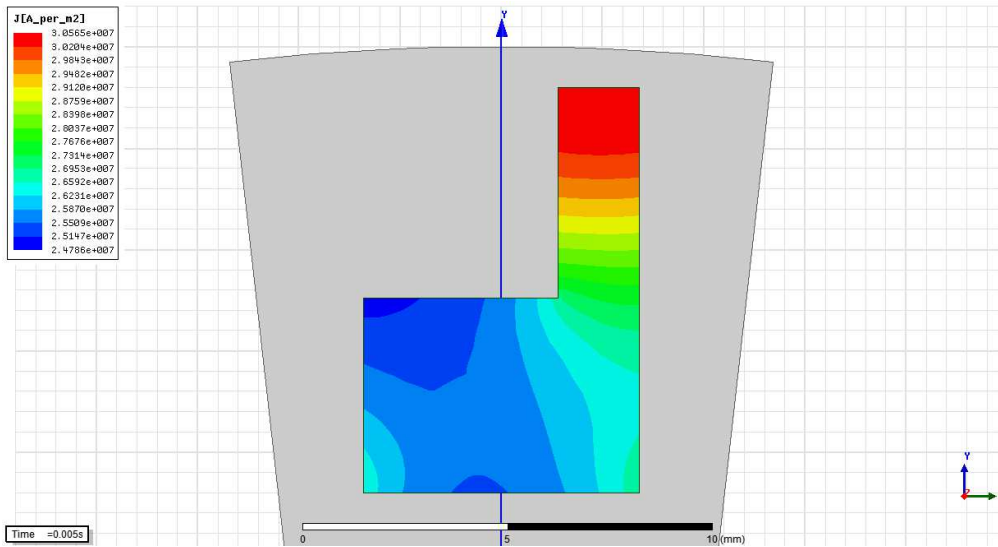
Figure A.31: Current density distribution of two-way rotor bar for 1st,7th and 11th harmonics
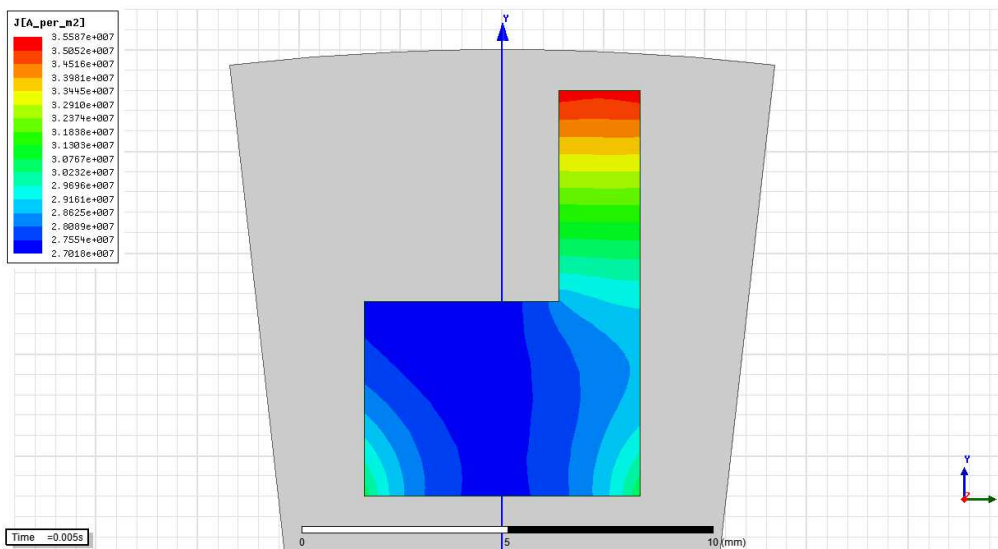
Figure A.32: Current density distribution of two-way rotor bar for 1st,5th and 13th harmonics

Figure A.33: Current density distribution of round rotor bar for 1st harmonic

Figure A.34: Current density distribution of round rotor bar for 1st and 5th harmonics

Figure A.35: Current density distribution of round rotor bar for 1st and 7th harmonics

Figure A.36: Current density distribution of round rotor bar for 1st,5th,7th,11th and 13th harmonics

Figure A.37: Current density distribution of round rotor bar for 1st,7th,11th and 13th harmonics

Figure A.38: Current density distribution of round rotor bar for 1st,5th,11th and 13th harmonics

Figure A.39: Current density distribution of round rotor bar for 1st,7th and 11th harmonics

Figure A.40: Current density distribution of round rotor bar for 1st,5th and 13th harmonics

Figure A.41: Current density distribution of square rotor bar for 1st harmonic

Figure A.42: Current density distribution of square rotor bar for 1st and 5th harmonics
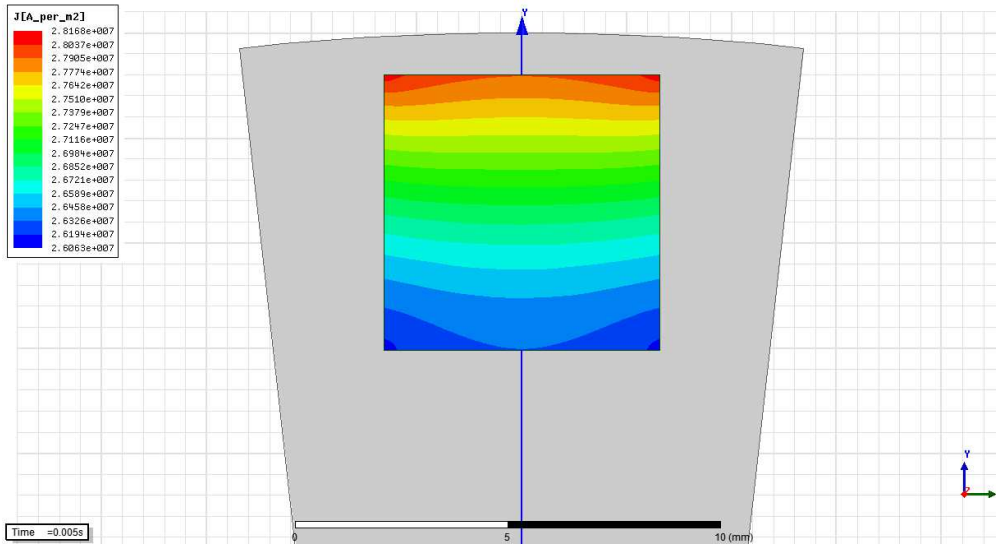
Figure A.43: Current density distribution of square rotor bar for 1st and 7th harmonics
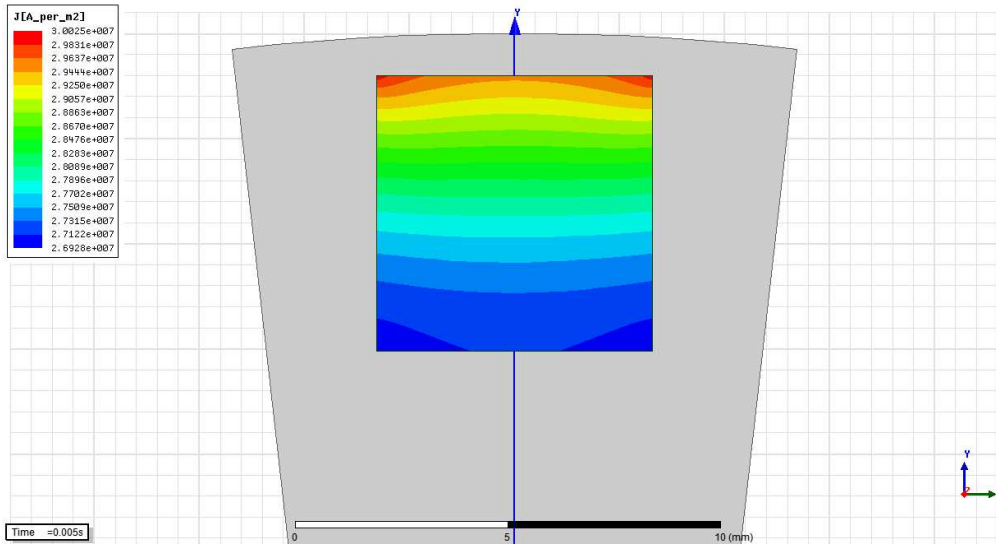
Figure A.44: Current density distribution of square rotor bar for 1st,5th,7th,11th and 13th harmonics

Figure A.45: Current density distribution of square rotor bar for 1st,7th,11th and 13th harmonics
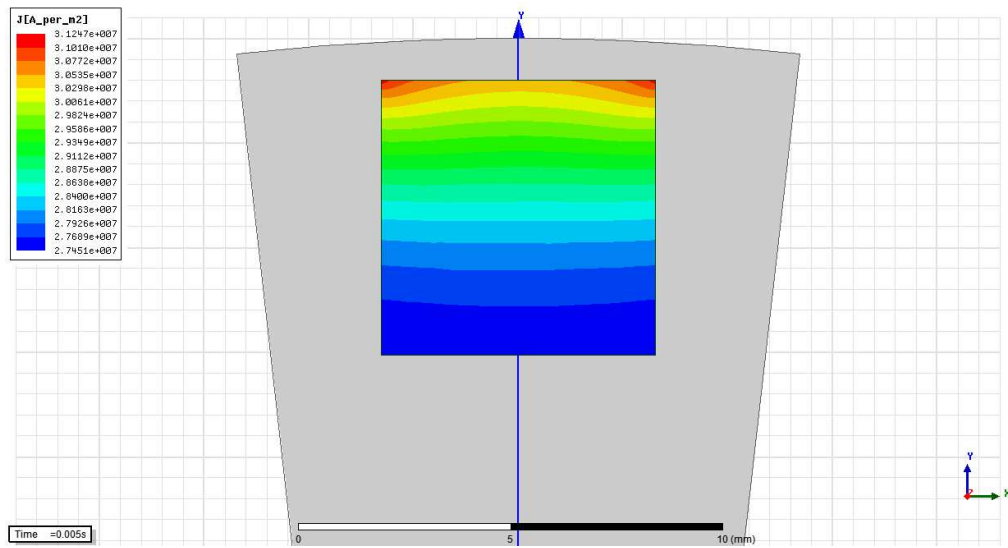
Figure A.46: Current density distribution of square rotor bar for 1st,5th,11th and 13th harmonics
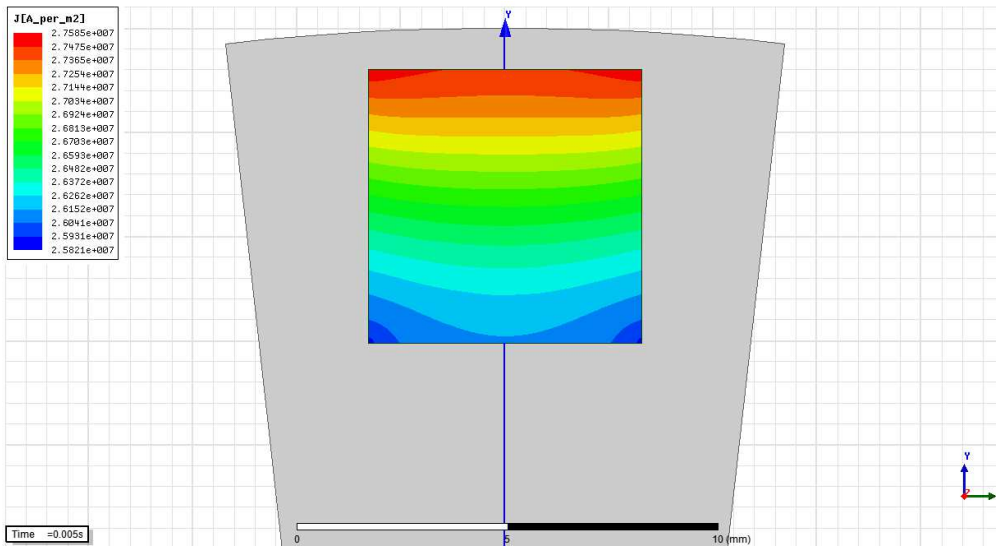
Figure A.47: Current density distribution of square rotor bar for $1^{st}, 7^{th}$ and 11th harmonics
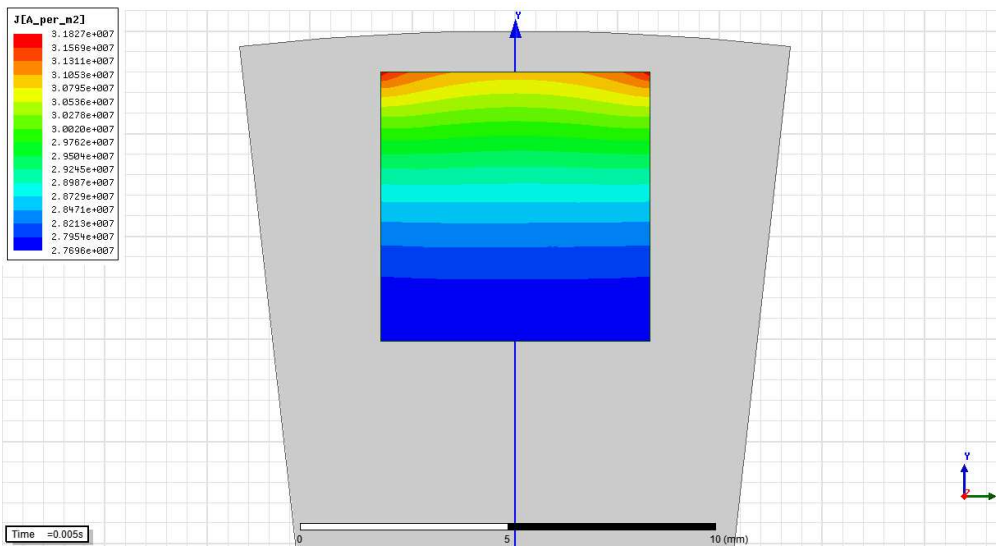
Figure A.48: Current density distribution of square rotor bar for $1^{st}, 5^{th}$ and 13th harmonics
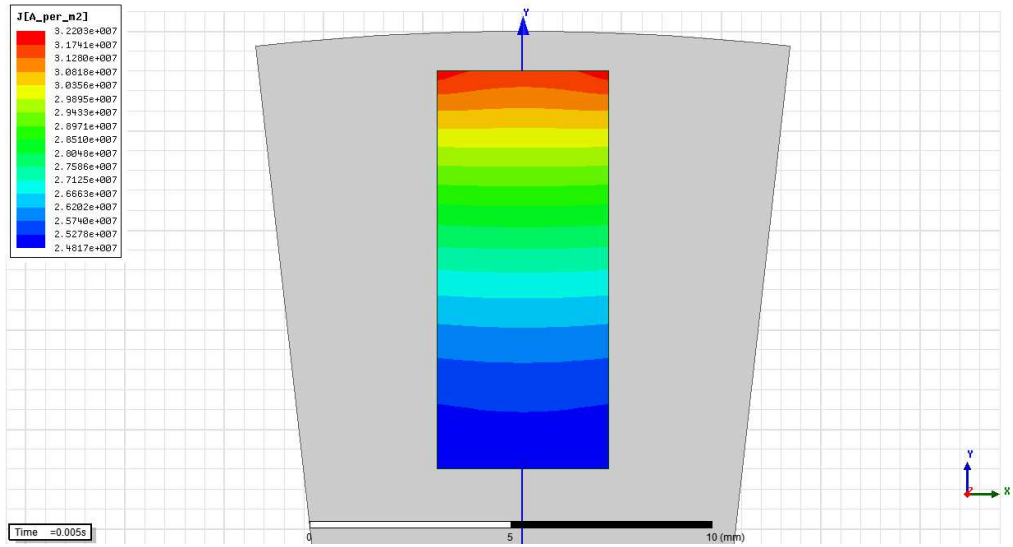
Figure A.49: Current density distribution of deep rotor bar for 1st harmonic
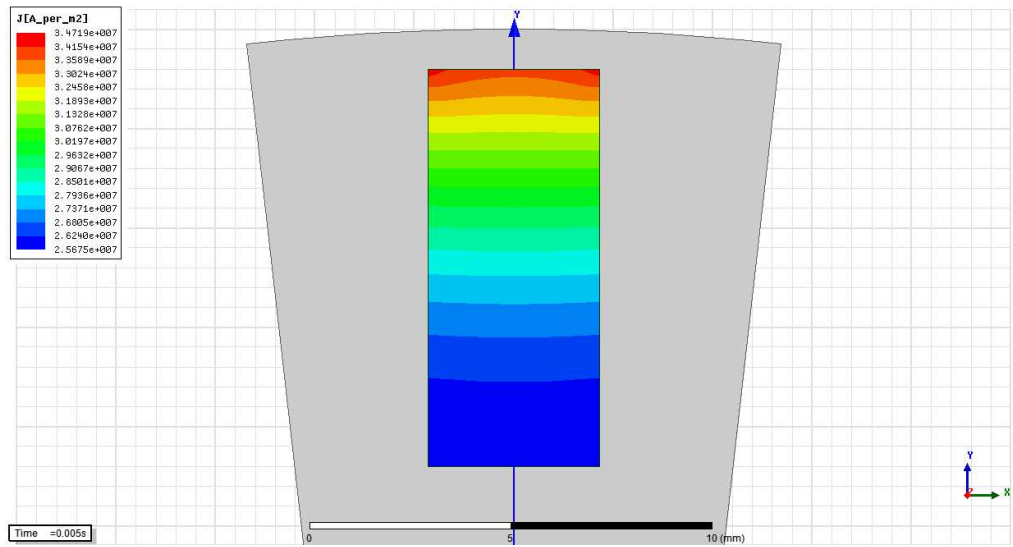
Figure A.50: Current density distribution of deep rotor bar for 1st and 5th harmonics
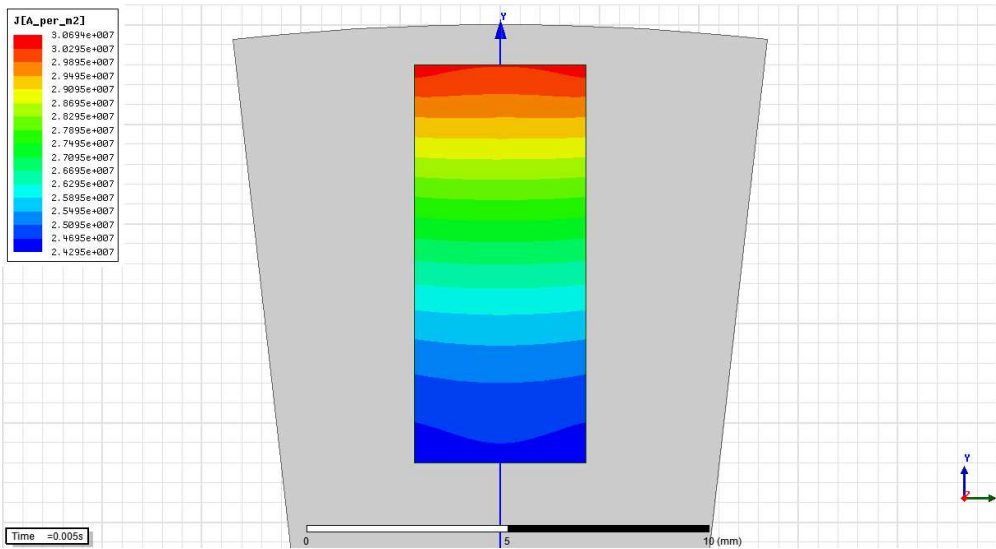
Figure A.51: Current density distribution of deep rotor bar for 1st and 7th harmonics
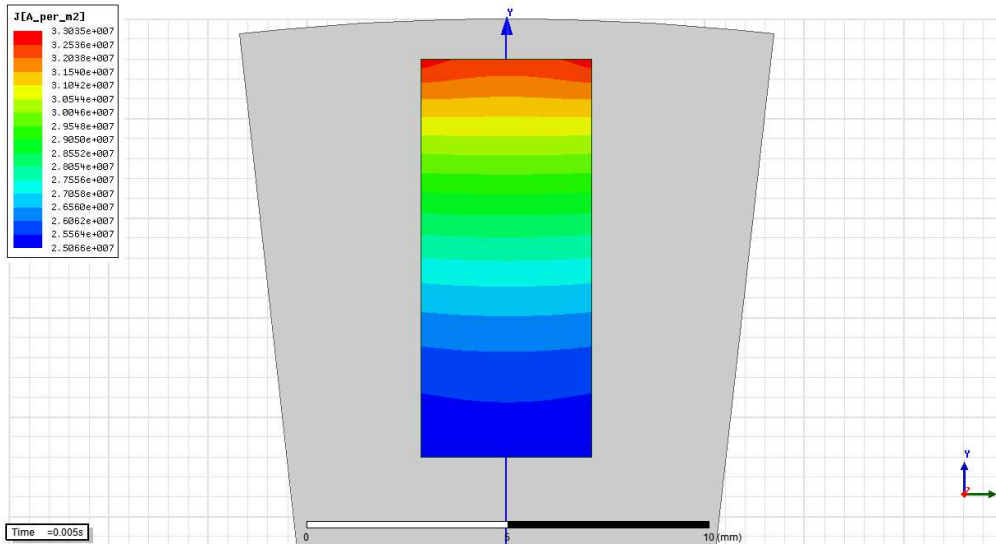
Figure A.52: Current density distribution of deep rotor bar for 1st,5th,7th,11th and 13th harmonics
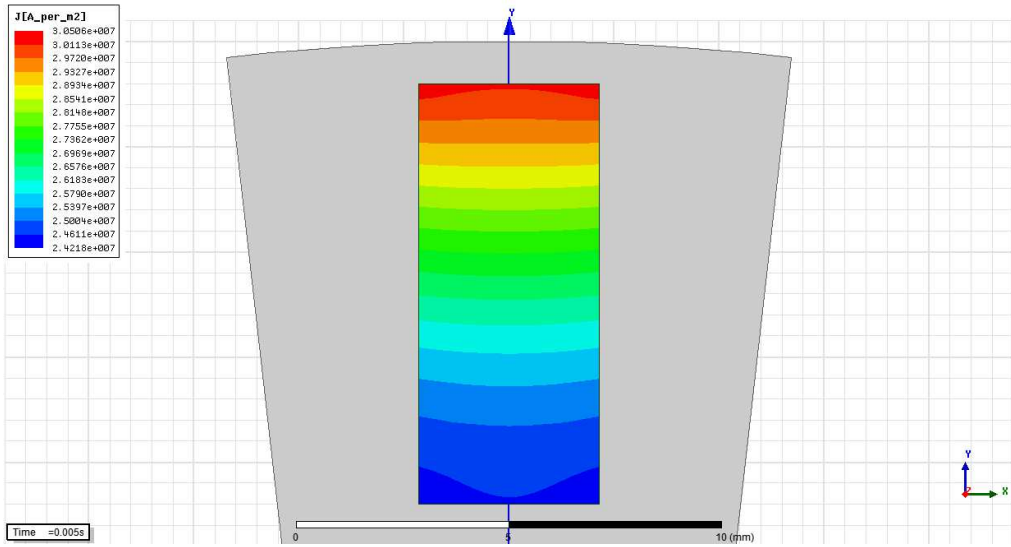
Figure A.53: Current density distribution of deep rotor bar for 1st,7th,11th and 13th harmonics
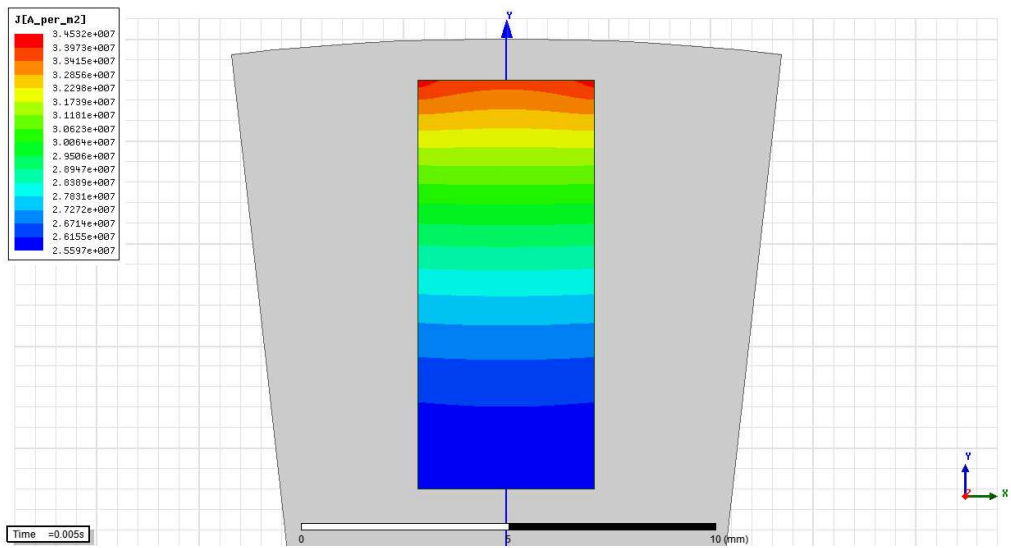
Figure A.54: Current density distribution of deep rotor bar for 1st,5th,11th and 13th harmonics
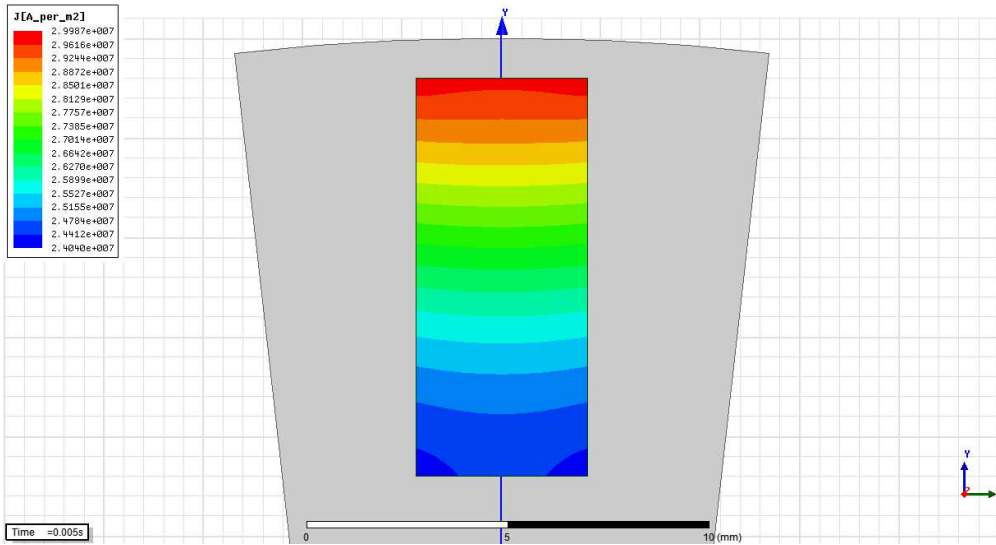
Figure A.55: Current density distribution of deep rotor bar for $1^{st}, 7^{th}$ and 11th harmonics
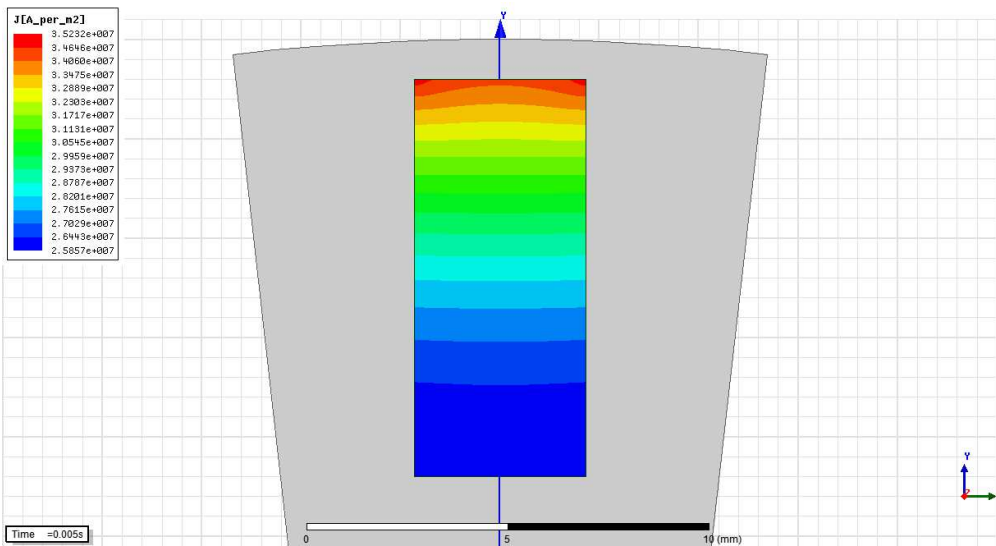
Figure A.56: Current density distribution of deep rotor bar for $1^{st}, 5^{th}$ and 13th harmonics
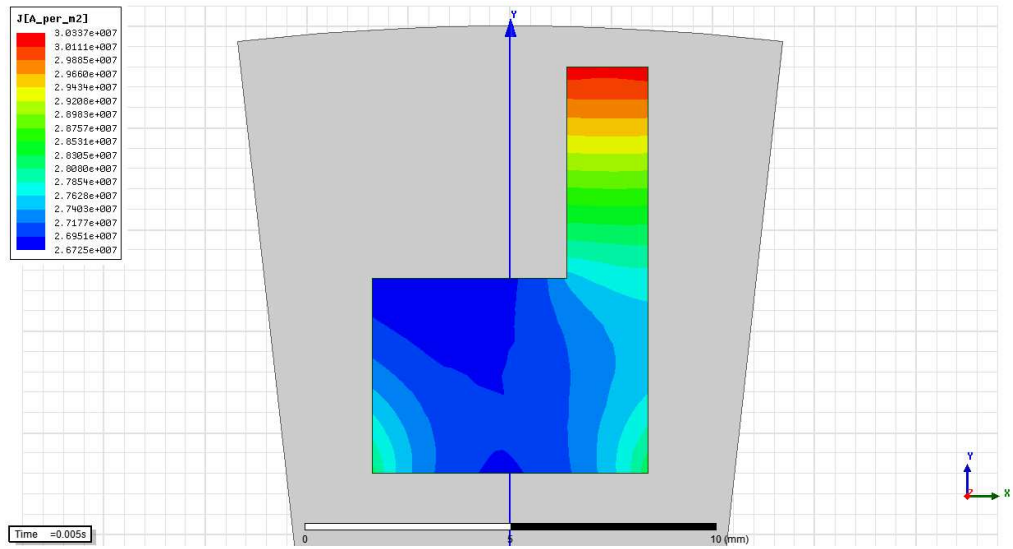
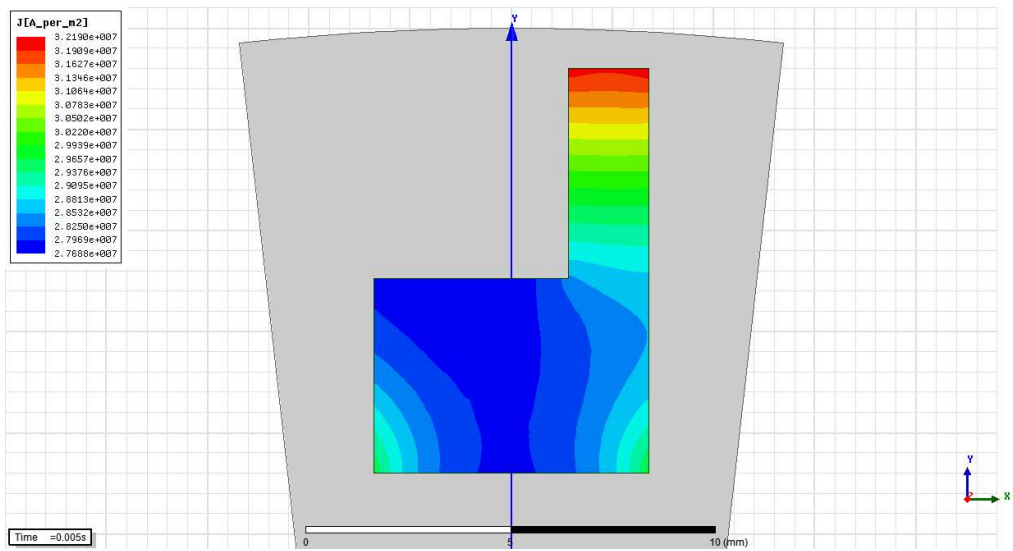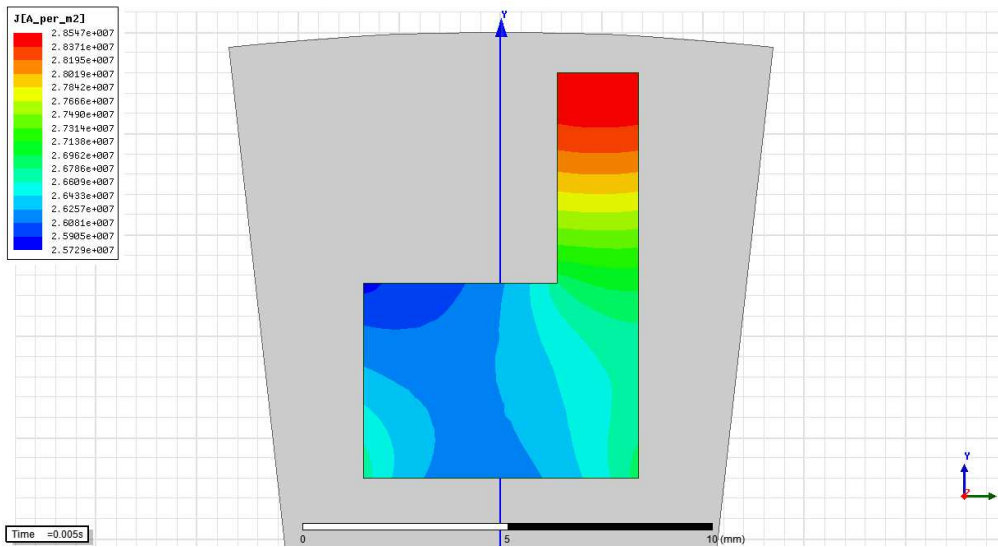**Figure A.57**: Current density distribution of two-way rotor bar for 1st harmonic
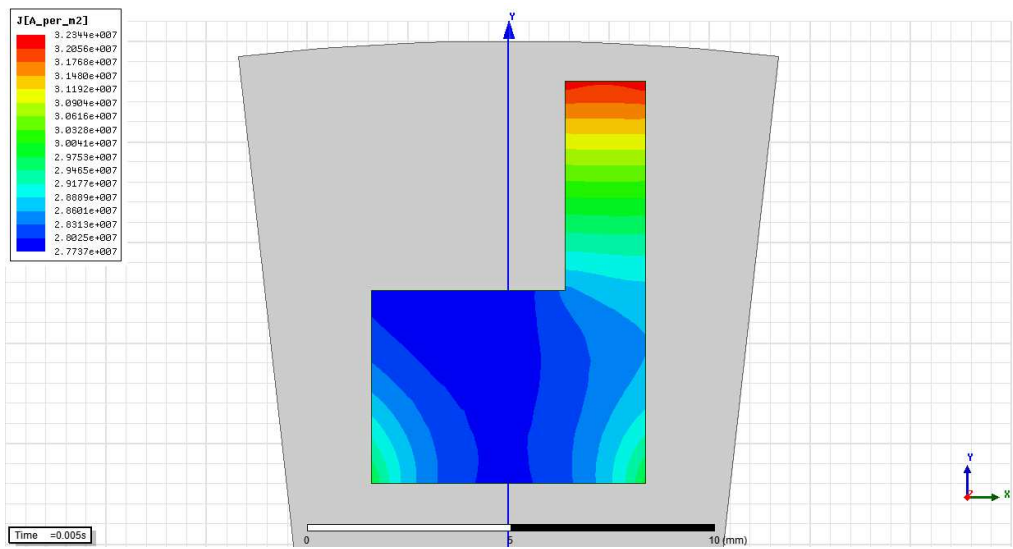
Figure A.58: Current density distribution of two-way rotor bar for 1st and 5th harmonics

79
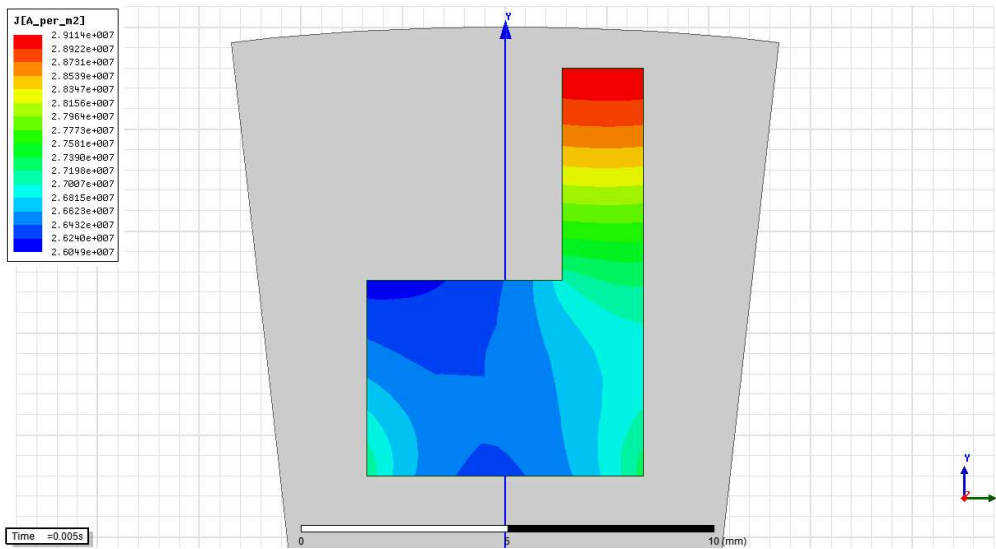
Figure A.59: Current density distribution of two-way rotor bar for 1st and 7th harmonics
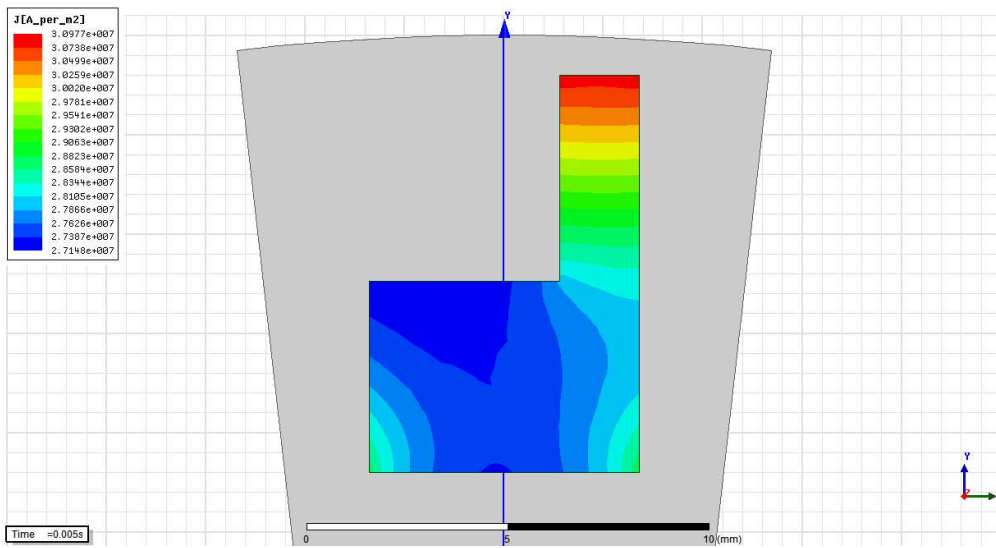
Figure A.60: Current density distribution of two-way rotor bar for 1st,5th,7th,11th and 13th harmonics
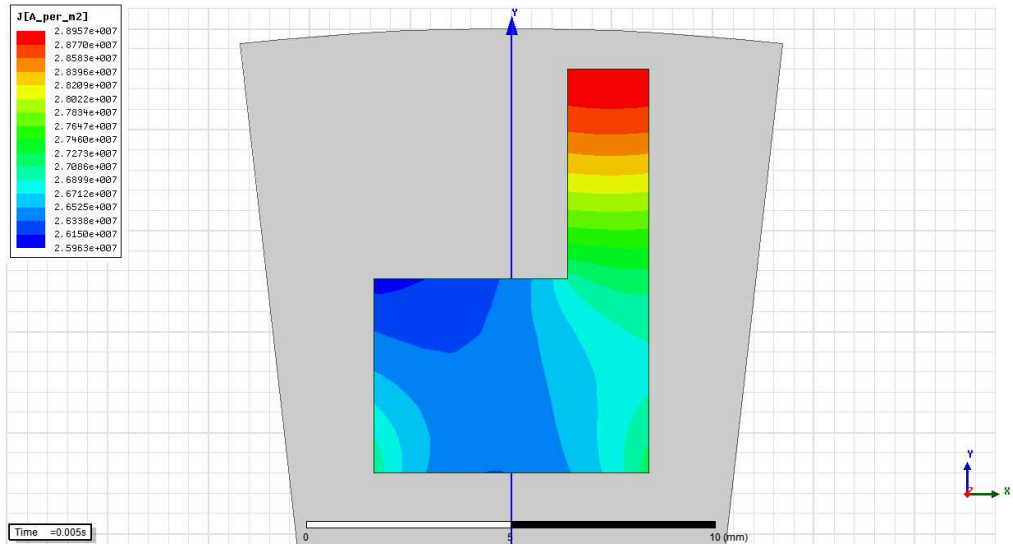
Figure A.61: Current density distribution of two-way rotor bar for 1st, 7th, 11th and 13th harmonics

Figure A.62: Current density distribution of two-way rotor bar for 1st, 5th, 11th and 13th harmonics

Figure A.63: Current density distribution of two-way rotor bar for 1st, 7th and 11th harmonics
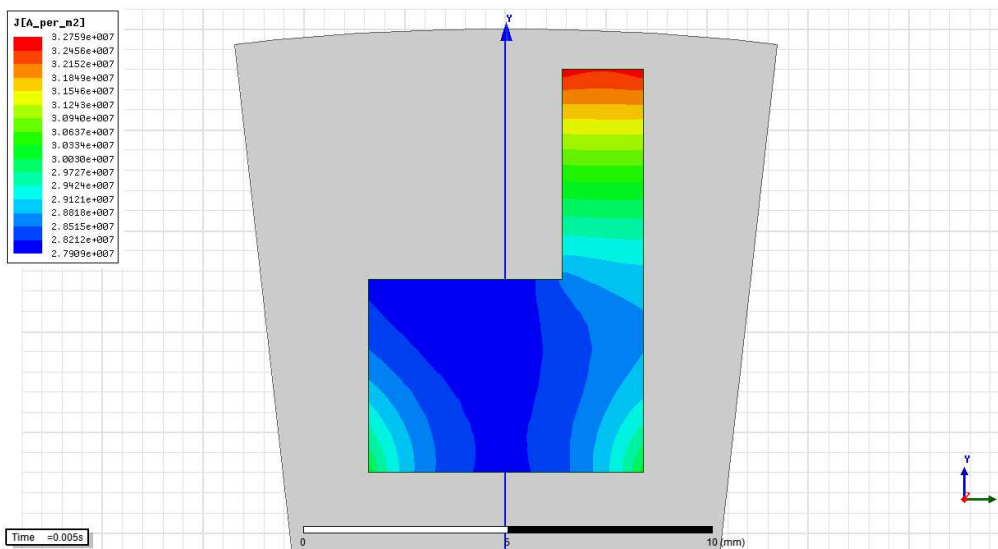
Figure A.64: Current density distribution of two-way rotor bar for 1st, 5th and 13th harmonics
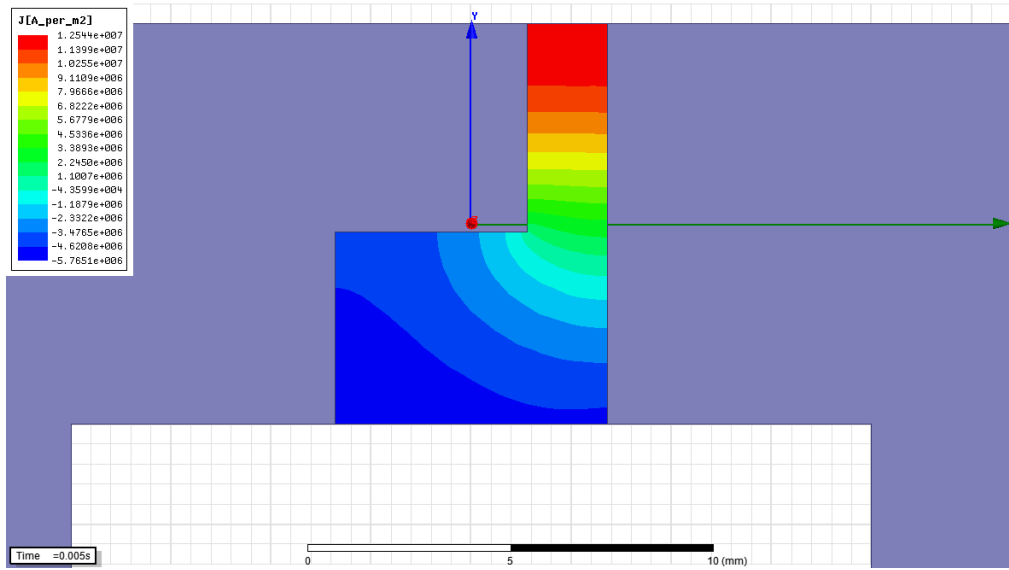
82

APPENDIX A.3

Figure A.65: Effect of 7th harmonic on two way copper rotor bar.
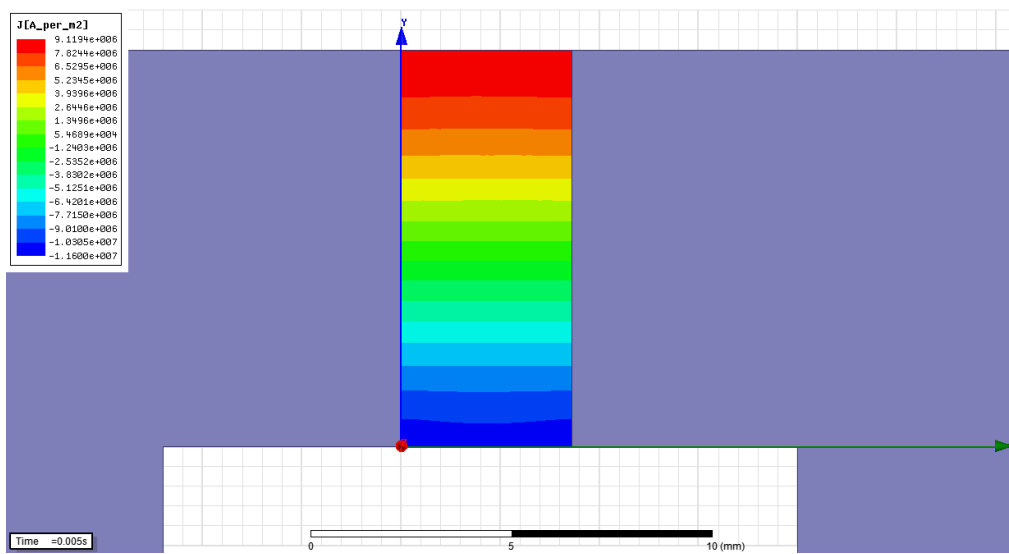

Figure A.66: Effect of 7th harmonic on deep copper rotor bar.
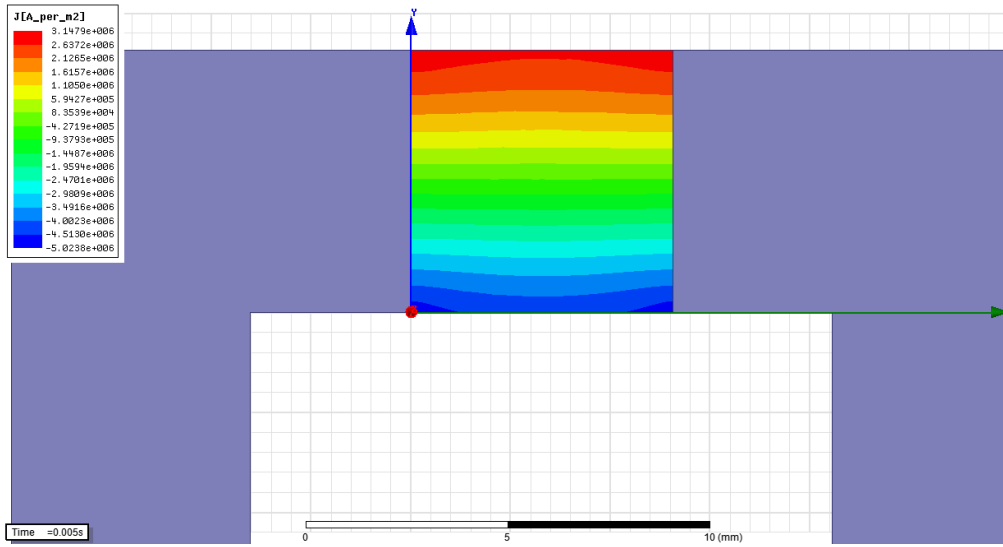
Figure A.67: Effect of 7th harmonic on square cross-section copper rotor bar.
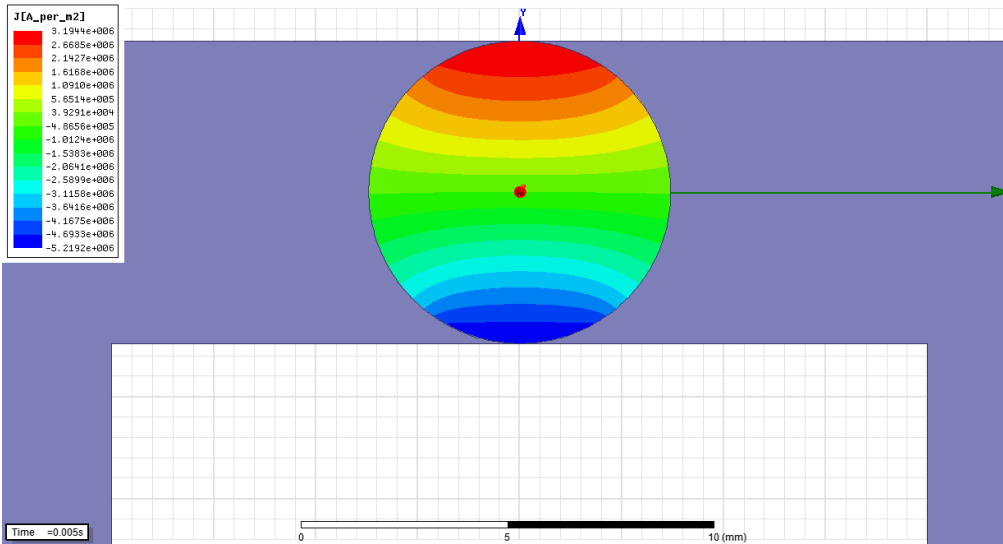

Figure A.68: Effect of 7th harmonic on round cross-section copper rotor bar.

CURRICULUM VITAE

Name Surname: Ahmet Yasin Yeksan

Place and Date of Birth: Konya, 1989

E-Mail: yeksan@itu.edu.tr

B.Sc.: Istanbul Technical University

Professional Experience and Rewards:
2011-To present Research Assistant Istanbul Technical University

List of Publications and Patents:
C. Gokce, O. Ustun, A.Y. Yeksan, "Dynamics and limits of electrical braking," in *8th International Conference on Electrical and Electronics Engineering*, Bursa, Turkey, 2013.